Annual Report
Jahresbericht

2011

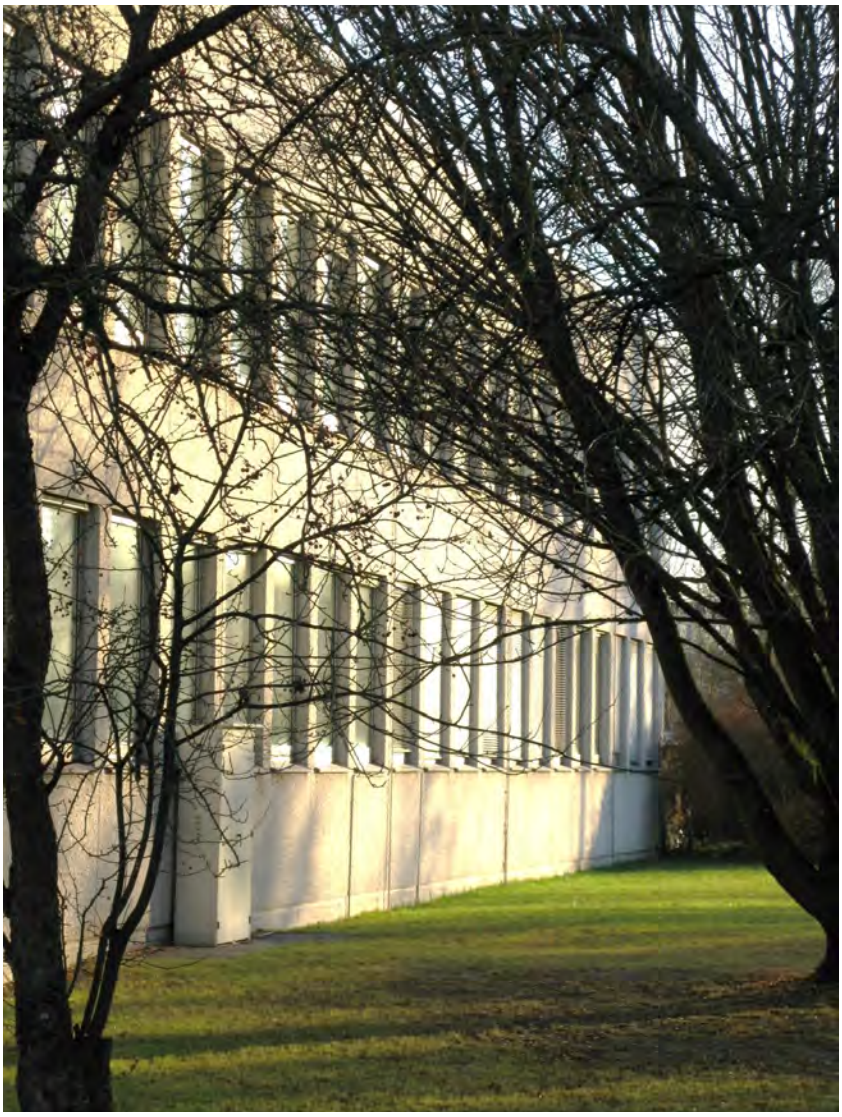

Walther–Meissner–Institut
für Tieftemperaturforschung
Bayerische Akademie der Wissenschaften

Contact:

Prof. Dr. Rudolf Gross
Walther–Meißner–Institut für Tieftemperaturforschung
Bayerische Akademie der Wissenschaften
and
Lehrstuhl für Technische Physik – E23
Technische Universität München

Address:

Walther–Meißner–Str. 8	Phone:	+49 – (0)89 289 14201
D - 85748 Garching	Fax:	+49 – (0)89 289 14206
GERMANY	e–mail:	Rudolf.Gross@wmi.badw.de
	WWW–address:	http://www.wmi.badw.de

Secretary's Office and Administration:

Emel Dönertas	Phone:	+49 – (0)89 289 14202
	Fax:	+49 – (0)89 289 14206
	e–mail:	Emel.Doenertas@wmi.badw.de
		Sekretariat@wmi.badw.de
Ludwig Ossiander	Phone:	+49 – (0)89 289 14205
	Fax:	+49 – (0)89 289 14206
	e–mail:	Ludwig.Ossiander@wmi.badw.de

Preface

Dear colleagues, friends, partners, and alumni of the Walther-Meißner-Institute for Low Temperature Research (WMI) of the Bavarian Academy for Sciences and Humanities (BAdW)!

On behalf of the members of WMI, I am pleased to present to you our ***Annual Report 2011***. With this report, we provide you an overview on our last year's activities ranging from fundamental studies in solid state physics, application oriented research, materials science to technological developments in low temperature, thin film and nanotechnology. Our research interests cover superconductivity and superfluidity, magnetism, strongly correlated electron systems, spintronics, as well as quantum and coherence in solid state systems. In 2011, we succeeded to further extended our efforts in research and teaching and to keep our internationally leading position in several areas of low temperature research. The report is aiming to provide not only concise summaries of our ongoing research projects and their major results, but also information on our teaching activities as well as interesting data about publications, completed and ongoing Ph.D., diploma, master and bachelor theses, collaborations, funding, and recent developments in infrastructure and experimental facilities.

In 2011, WMI was successful in extending several long-term, coordinated research programs jointly put into effect in collaboration with partners from both Munich universities and other national and international research institutions. The *Collaborative Research Center 631* (Solid State Quantum Information Processing) was reviewed in February 2011 and a third four-year funding period (07/2011 – 06/2015) has been granted by the senate of the German Research Foundation (DFG). The same is true for the *DFG Priority Program 1285* (Semiconductor Spin Electronics), which has been extended until 2013. Moreover, WMI is participating in the new *DFG Priority Program 1538* (Spin Caloric Transport), which has been started in May 2011. The proposal for the second funding period of the *Cluster of Excellence Nanosystems Initiative Munich* has been submitted and will be reviewed in January 2012. Further coordinated research programs, such as the *Transregional Collaborative Research Center TRR 80* (From Electronic Correlations to Functionality) and the *DFG Priority Program 1485* (High Temperature Superconductivity in the Iron-Pnictides) are ongoing. In several of these programs, WMI is playing a leading role and providing the coordinator of the program. Various other national and international research projects of WMI have been successfully continued in 2011 and promising new projects could be started. In particular, I would like to mention the new EU network *Circuit and Cavity Quantum Electro-Dynamics (CCQED)*. This network has been granted 3.5 Million Euros by the European Union through a Marie Curie Action within the Seventh Framework Program Initial Training Network ITN-People-2010.

Throughout 2011, more than 70 people were working in the crowded laboratories and offices of WMI, including more than 20 Ph.D. students and a large number of bachelor, master and diploma students. In 2011, 5 Ph.D. theses, 9 diploma and master theses, and 18 bachelor theses were completed. Regarding laboratory space, the tense situation could be relaxed by the completion of the new *WMI Quantum Science Laboratory* in the basement of the WMI building, providing about 150 m^2 additional laboratory space particularly designed for low temperature facilities and ultra-sensitive studies on solid state quantum systems. This new lab was financed by extra money from the state government within the so-called "Konjunkturpaket II". WMI also succeeded in keeping the high level of third-party funding in 2011. In particular, WMI could acquire a new dilution fridge with vector magnet financed by the "State Major Instrumentation Programme".

Our successful research in 2011 is reflected in many excellent publications, new extramural funding, collaborations with industry, and many invited presentations at national and in-

ternational conferences. WMI also has organized national and international workshops and conferences, in this way promoting the scientific visibility of WMI. This would not have been possible without the dedicated and hard work of all scientific and technical staff as well as doctorate, diploma, master and bachelor students. An important prerequisite of our successful research work is the continuous support of various funding agencies. In this context I gratefully acknowledge financial support from the BAdW, the DFG, the Bavarian Ministry for Science and Arts, the BMBF and the EU. A further key to our success in research is the recruitment of outstanding, scientifically independent group leaders with complementary research interests and technical expertise, a process which is supported and monitored by the scientific advisory board of WMI, and the excellent quality of our Ph.D., diploma and master students. We are much committed to support and promote young scientists in their career.

I hope that our Annual Report 2011 inspires your interest in WMI. I take this opportunity to thank all the colleagues, guests, students, post–docs and cooperating partners, who contributed to our research and teaching activities within the last year, and last but not least all our friends and sponsors for their interest, trust and continuous support.

Garching, December 2011

Rudolf Gross

the majority of the WMI team members

Contents

The Walther–Meißner–Institute

General Information

The Walther–Meißner–Institute for Low Temperature Research (WMI) is operated by the Commission for Low Temperature Research of the Bavarian Academy of Sciences and Humanities (BAdW). The commission was founded in 1946 on Walther Meißner's initiative, who was president of BAdW from 1946 to 1950. The Commissions (Research Groups) of the Academy are set up in order to carry out long–term projects, which are too ambitious for the lifetime or capacity of any single researcher, or which require the collaboration of specialists in various disciplines. At present, the Bavarian Academy of Sciences and Humanities consists of 36 Commissions with more than 300 employees.

The Commission for Low Temperature Research of the BAdW started its research activities in 1946 in the Herrsching barracks. After the retirement of Walther Meißner in 1952, Heinz Maier-Leibnitz, who followed Walther Meißner on the Chair for Technical Physics of the Technische Universität München, became the new head of the Commission for Low Temperature Research. In 1967, the commission moved to the Garching research campus after the construction of the new "Zentralinstitut für Tieftemperaturforschung" (ZTTF) was completed (director: Prof. Heinz Maier-Leibnitz, technical director: Prof. Franz Xaver Eder). Until 1972, the theory group of the Institute Laue Langevin was hosted at the ZTTF. In 1980, Prof. Dr. Klaus Andres became the new director of the ZTTF again associated with the Chair for Technical Physics (E23) at the Technische Universität München, followed by Prof. Dr. Rudolf Gross in 2000. In 1982, the ZTTF was renamed into Walther-Meißner-Institute for Low Temperature Research (WMI) on the occasion of Walther Meißner's 100. birthday.

As already mentioned, it is a long tradition that WMI hosts the Chair for Technical Physics (E 23) of the Technische Universität München (TUM) with the director of the WMI being full professor at the Faculty of Physics of TUM. However, there are also close ties with the Ludwig-Maximilians-Universität (LMU). Between 2004 and 2010, WMI hosted a scanning probe division with the head of this division being professor at the Ludwig-Maximilians-Universität (LMU). In this way a tight collaboration has been established between WMI and research groups of both Munich universities, joining technological and human resources in the fields of experimental and theoretical solid-state and condensed matter physics, low temperature techniques, materials science as well as thin film and nanotechnology. Noteworthy, the WMI supplies liquid helium to more than 25 research groups at both Munich universities and provides the technological basis for low temperature research.

Research Activities

The research activities of the Walther–Meißner–Institute are focused on low temperature solid-state and condensed matter physics (see reports below). The research program is devoted to both **fundamental** and **applied research** and also addresses **materials science, thin film and nanotechnology** aspects. With respect to **basic research** the main focus of the WMI is on

- superconductivity and superfluidity,
- magnetism and spin transport,
- quantum phenomena and quantum coherence in mesoscopic systems and nanostructures,

- self-organization of molecules on surfaces,
- and the general properties of metallic systems at low and very low temperatures.

The WMI also conducts **applied research** in the fields of

- solid-state quantum information processing systems,
- superconducting and spintronic devices,
- oxide electronics,
- multi-functional and multiferroic materials,
- and the development of low and ultra low temperature systems and techniques.

With respect to **materials science, thin film and nanotechnology** the research program is focused on

- the synthesis of superconducting and magnetic materials,
- the single crystal growth of oxide materials,
- the thin film technology of complex oxide heterostructures including multi-functional and multiferroic material systems,
- and the fabrication of superconducting, magnetic, and hybrid nanostructures.

The WMI also develops and operates systems and techniques for low and ultra–low temperature experiments. A successful development have been dry mK-systems that can be operated without liquid helium by using a pulse-tube refrigerator for precooling. Meanwhile, these systems have been successfully commercialized by the company VeriCold Technologies GmbH at Ismaning, Germany, which was taken over by Oxford Instruments in 2007. As further typical examples we mention a nuclear demagnetization cryostat for temperature down to below 100 μK, or very flexible dilution refrigerator inserts for temperatures down to about 20 mK fitting into a 2 inch bore. These systems have been engineered and fabricated at the WMI. Within the last years, several dilution refrigerators have been provided to other research groups for various low temperature experiments. The WMI also operates a helium liquifier with an annual capacity of well above 150.000 liters and supplies both Munich universities with liquid helium. To optimize the transfer of liquid helium into transport containers the WMI has developed a pumping system for liquid helium that is commercialized in collaboration with a company.

To a large extent the research activities of WMI are integrated into national and international research projects such as Clusters of Excellence, Collaborative Research Centers, Research Units, or EU projects. The individual research groups of WMI offer a wide range of attractive research opportunities for diploma (graduate) students, PhD students and postdoctoral fellows.

Experimental Facilities and Resources

The WMI is equipped with state of the art facilities for the preparation and characterization of superconducting and magnetic materials as well as for various low and ultra–low temperature experiments. The main experimental and technological resources of WMI are listed in the following.

Materials Preparation and Fabrication of Nanostructures

- Laser Molecular Beam Epitaxy (L-MBE) system for oxide heterostructures (equipped with in–situ RHEED, Omicron AFM/STM system, atomic oxygen/nitrogen source, infrared-laser heating system, metallization)
- molecular beam epitaxy (MBE) system for metallic systems
- UHV magnetron sputtering systems for metals (e.g. Nb, Al, NiPd, ...)
- magnetron sputtering system for oxide heteroepitaxy (equipped with four sputtering guns and an oxygen ion gun)
- reactive ion etching (RIE) system, Plasmalab 80 Plus with ICP plasma source, Oxford Instruments Plasma Technology
- ion beam etching (IBE) system equipped with a LN_2 cooled sample holder
- polishing machine for substrate preparation
- ultrasonic bonding machine
- 50 m^2 class 1000 clean room facility
- optical lithography (Süss maskaligner MJB 3 and projection lithography)
- electron beam lithography (based on Philips XL 30 SFEG scanning electron microscope and Raith Elphy Plus lithography system including a laser stage)
- four-mirror image furnace for crystal growth

Characterization

- 2–circle x–ray diffractometer (Bruker D8 Advance, sample temperature up to 1 600°C)
- high resolution 4–circle x–ray diffractometer with Göbel mirror and Ge monochromator (Bruker D8 Discover)
- scanning electron microscope with EDX analysis
- UHV room temperature AFM/STM system
- 2048 u high resolution mass spectrometer (Fa. Pfeiffer, cross beam ion source, SEM)
- Low Energy Electron Diffraction (SPECTA-LEED, Fa. Omicron)
- two Raman spectroscopy systems (1.5 to 300 K, in-situ sample preparation)
- SQUID magnetometer (Quantum Design, 1.5 to 700 K, up to 7 Tesla)
- several high field magnet systems (up to 17 Tesla) with variable temperature inserts
- 7 Tesla split coil magnet systems with optical access and variable temperature insert
- experimental set–ups for the measurement of noise including low noise SQUID amplifiers and signal analyzers
- high-frequency network analyzers (up to 40 GHz) and various microwave components (sources, mixers, circulators, attenuators) for the determination of high frequency parameters
- high-frequency cryogenic probing station (up to 20 GHz, $T > 4$ K)
- magnetooptical Kerr effect (MOKE) system
- ferromagnetic resonance (FMR) system

Low temperature systems and techniques

- 5 K-Scanning Tunneling Microscope (low temperature STM, Fa. Omicron)
- several ^{3}He/^{4}He dilution refrigerator inserts for temperatures down to 10 mK
- "dry" mK-cooler based on a dilution refrigerator with pulse-tube precooling
- ultra–low temperature facility for temperatures down to below 100 μK based on a nuclear demagnetization cryostat
- experimental set–ups for the measurement of specific heat, magnetization, thermal expansion as well as electrical and thermal transport properties as a function of temperature, magnetic field and pressure

Joint Research Projects

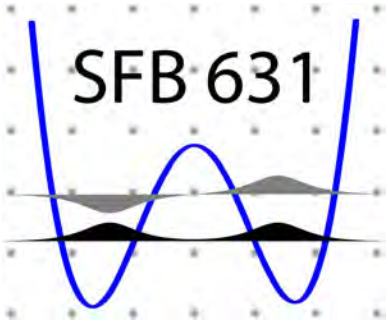

SPP 1285

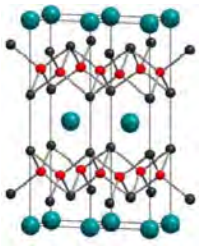

SPP 1458

SPP 1538

The Collaborative Research Center 631

F. Deppe, R. Gross, H. Hübl, A. Marx[1]

The Collaborative Research Center 631 (SFB 631) on Solid State Quantum Information Processing was granted a third four-year funding period. SFB 631 was established in 2003 and extended for a second four-year funding in 2007. After a review process in February 2011, the "Senatsausschuss für die Angelegenheiten der Sonderforschungsbereiche" of the German Research Foundation (DFG) has granted the third funding period (07/2011–06/2015) of SFB 631 in May 2011.

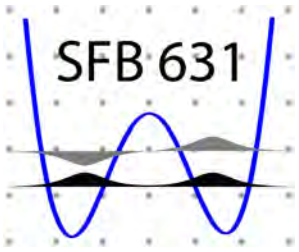

Quantum information science is a fascinating and one of the most rapidly growing fields of science and technology, residing at the interface between physics, mathematics, computer and materials science, and engineering. It is concerned with both fundamental questions and technological developments, aiming at the realization of a useful quantum information hardware. Over the last decade, the physics of solid state quantum systems has developed into a key research field of Walther-Meißner-Institute (WMI). It requires extremely sensitive measurements at low and ultra-low temperatures and therefore perfectly fits to the research profile of WMI.

Solid state systems are considered a particularly promising platform for the successful implementation of quantum information systems. The Collaborative Research Center 631 studies the ***physical concepts, materials aspects, and technological foundations of solid state quantum information processing (SQIP)***. It deals with the coherent dynamics of solid state quantum systems and has the vision to engineer them so as to allow to process and communicate information on the basis of quantum mechanical principles. To realize this vision, SFB 631 aims at the clarification of the key physical questions as well as the materials aspects and technological problems that have to be solved for the successful implementation of SQIP. Particular goals are to design and implement solid state quantum bits (qubits) with long coherence times, to learn how to efficiently control, manipulate and read-out qubits, to couple them to complex systems as well as to develop theoretical tools for modeling the dynamics of driven, damped qubits in different experimental systems. The long-term goal is the development of small-scale solid state quantum systems that are capable of performing elementary processing and communication of quantum information. This involves the design, fabrication and investigation of solid state qubits, oscillators, cavities and transmission lines that can be combined to create hybrid quantum circuits.

To cover the broad spectrum of fundamental and application oriented questions related to solid state quantum information systems in a comprehensive way, SFB 631 joins research activities from quantum information theory, experimental and theoretical solid state physics, quantum optics, materials science, and nanotechnology. Today, within SFB 631 research groups from the Bavarian Academy of Sciences and Humanities (BAdW), the TU Munich (TUM), the Ludwig-Maximilians-University (LMU), the Max-Planck-Institute for Quantum Optics (MPQ), as well as Augsburg and Regensburg University are collaborating in 17 research projects. The main objective is to obtain a profound understanding of the physics, technology, and materials aspects of SQIP by making use of advanced experimental and theoretical methods in a coordinated interdisciplinary research effort. At present, SFB 631 joins more than 30 principal investigators and more than 60 Ph.D. and diploma students, as well

[1]This work is supported by the German Research Foundation through SFB 631.

as a large number of postdocs and guest scientists. WMI is one of the main actors, not only being involved in the three projects A3 (Gross, Hübl, Marx), A8 (Gross, Marx, Deppe) and C3 (Hübl), but also providing the coordination of the center from the beginning (spokesman: Rudolf Gross).

Within the project A3 on *Superconducting Quantum Circuits as Basic Elements for Quantum Information Processing* and project A8 on *Cavity Quantum Electrodynamics with Superconducting Devices*, the research program of WMI within SFB 631 is focussing on the fabrication and study of superconducting quantum information circuits. This includes the fabrication of superconducting flux qubits in which quantum mechanical superposition states of clockwise and counter-clockwise circulating persistent currents are used for the realization of solid state qubits. These qubits are coupled to superconducting microwave resonators. In this way fascinating quantum electrodynamic experiments with deliberately designed artificial solid state atoms become possible. Since such experiments are completely analogous to quantum optical experiments on natural atoms in optical resonators, this prospering new field is called circuit quantum electrodynamics (circuit QED). Here, particular goals are the strong and ultrastrong coupling of superconducting qubits to high-quality superconducting microwave resonators, the generation and detection of non-classical microwave states (e.g. Fock or squeezed states), the development of dispersive readout and quantum non-demolition measurements, and the entanglement of superconducting qubits via multiple resonators. Regarding these research goals the WMI team closely collaborates with the theory groups at LMU (von Delft), the University of Augsburg (Hänggi), the Universidad del País Vasco - Euskal Herriko Unibertsitatea at Bilbao (Solano), and the Instituto de Física Fundamental at Madrid (Garcia-Ripoll), as well as the experimental groups at the NTT Basic Research Laboratories (Semba) and the Nano Electronics Research Laboratories at NEC Corporation, Japan (Nakamura, Tsai, Yamamoto). The research work within SFB 631 is also closely linked to the activities within Research Area I of the Cluster of Excellence *Nanosystems Initiative Munich (NIM)* (see pp. 15–17).

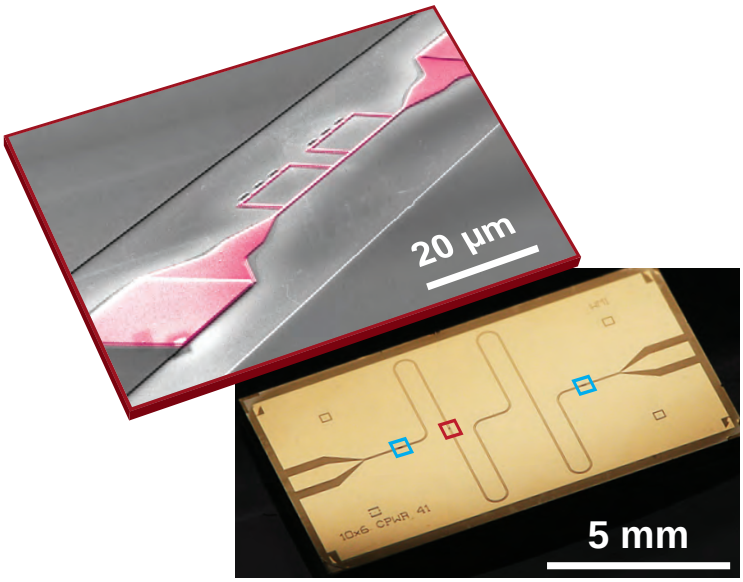

Figure 1: Optical and false-color scanning electron images of the galvanically coupled quantum circuit. The position of the flux qubits (magenta) is indicated by the red box and the light blue boxes mark the position of the coupling capacitors.

Selection rules in a strongly coupled qubit-resonator system. In 2011, we have demonstrated the controllability of fundamental symmetry properties of circuit QED systems in the strong coupling limit as shown in the report by Niemczyk *et al.* (see pp. 36–38). One of the key features of circuit QED setups is their design flexibility and the ability to tune their properties in situ by an external control parameter. This triggered experimental studies of multi-photon driven artificial atoms. Our one- and two-photon spectroscopy of a flux qubit-resonator system provide clear evidence for the controlled transition from an operating point governed by dipolar selection rules to a regime

where one- and two-photon excitations of our artificial atoms coexist. By tuning an external control parameter (applied magnetic flux) the symmetry of the system can be broken in a controlled way and two-photon driving of the coupled qubit-cavity system becomes possible.

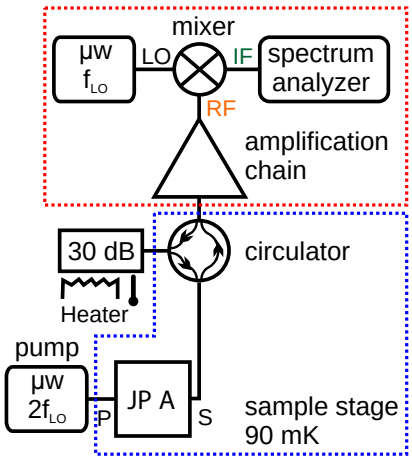

Figure 2: Simplified sketch of the experimental setup for generating and detection squeezed vacuum. The red rectangle marks the homodyne detector.

Squeezing the vacuum with a flux-driven Josephson parametric amplifier. A squeezed state, in general, is a state where the uncertainty is decreased in one quadrature of the electromagnetic field and increased in the other such that their product still satisfies Heisenberg's uncertainty relation. Using a flux-driven Josephson parametric amplifier (JPA) we have successfully generated a quantum microwave state, whose squeezed quadrature has an uncertainty below the vacuum noise level (standard quantum limit) as shown in the report by Menzel *et al.* (see pp. 39–41). The amplified output signal of the JPA is measured by a homodyne detector. The achieved squeezed state is well suited to be reconstructed by our dual-path state reconstruction scheme for propagating quantum microwaves. While it is already interesting on its own to study the quantum effect of squeezing, squeezed microwaves are also compatible with circuit quantum electrodynamics and can be used in various applications.

Gradiometric flux quantum bits with tunable tunnel coupling. At the WMI, we focus on flux qubits, where quantum information is encoded in the magnetic flux generated by a circulating current in a superconducting loop containing three or more Josephson junctions. We have extended our studies to a gradiometric design with a tunable tunnel coupling as outlined in the report by Schwarz *et al.* (see pp. 51–53). This qubit layout allows for an adjustable energy gap without detuning the qubit from the point of optimal coherence. We have fabricated tunable flux qubits in a gradiometric design demonstrating a large tunability of the qubit gap from zero to at least 5 GHz. An implementation of this qubit type into circuit QED experiments with a qubit coupled to a microwave resonator is currently pursued.

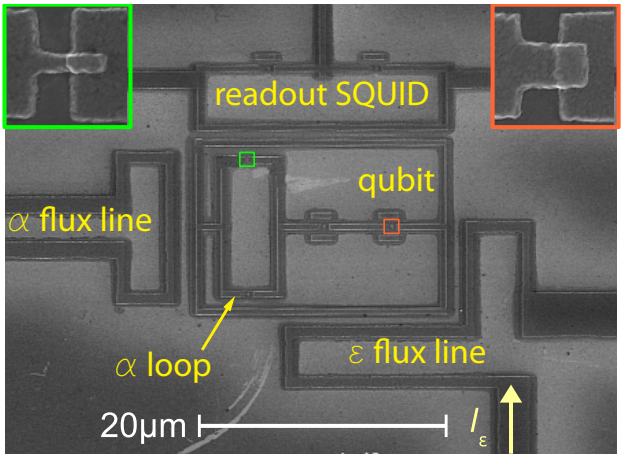

Figure 3: Scanning electron micrograph of gradiometric flux quantum bit with tunable tunnel coupling with readout SQUID. The insets show enlarged views of the Josephson junctions.

Microwave beam splitters and (multi) resonator systems. Important ingredients of circuit QED experiments are microwave beam splitters when dealing with concepts based on quantum microwaves propagating in open transmission lines. Among the various types of superconducting transmission lines, coplanar structures are particularly popular because they

exhibit high field densities and low dielectric losses. However, standard microwave beam splitters such as the 180° hybrid ring have a rather large diameter clearly hindering scalability. Therefore, we have fabricated and characterized a superconducting hybrid ring with coplanar feed lines and minimized dimensions. These hybrid rings show a form factor of 23% of that of standard 180° hybrid rings and are promising candidates as elements for photon based quantum computing with superconducting circuits or state reconstruction of propagating quantum microwaves as shown in the report by Kalb *et al.* (see pp. 54–55).

Superconducting waveguide resonators acting as "photon boxes" are fundamental elements of most circuit quantum electrodynamics (QED) setups. In contrast to the widely used coplanar waveguide (CPW) geometries, microstrip resonators are promising with respect to scalability since the microrstrip geometry allows for the straightforward implementation of additional circuit elements and control lines. We have characterized a large number of microstrip resonators systematically varying the geometry at low temperatures down to 20 mK and low probe power. We have demonstrated internal quality factors which are suitable for circuit QED applications (c.f. report by Baust *et al.*, pp. 59–61).

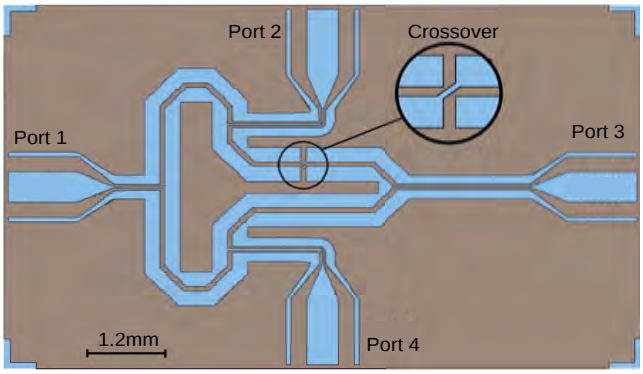

Figure 4: Sketch of a compact 180° coplanar hybrid ring. Blue areas: niobium. Grey area: substrate.

The resulting requirements on coherence times of the qubits or artificial atoms can, to some extent, be relaxed by engineering larger coupling strengths. In this situation, we need to consider not only the qubit-resonator coupling, but also the resonator-resonator interaction strength. Therefore, we have studied distributed coupling between two superconducting microstrip transmission line resonators. We achieve coupling rates that are already comparable to the ultrastrong qubit-resonator coupling rates as shown in the report by Haeberlein *et al.* (see pp. 56–58). Therefore, a possible quantum processor using ultrafast quantum gates and coupled resonators would not be not limited by the latter. Furthermore, our resonators are candidates for measuring the breakdown of thermal entanglement with cross-correlation techniques.

The Nanosystems Initiative Munich – NIM

S.T.B. Gönnenwein, R. Gross, H. Hübl, A. Marx[1]

The Cluster of Excellence ***Nanosystems Initiative Munich (NIM)*** was launched in 2006 and merges the expertise from research groups in the Munich area on man-made and biological nanoscale systems. The cluster joins research groups from LMU Munich, TU Munich, WMI, the University of Augsburg, the Munich University of Applied Science, the Max-Planck-Institutes for Biochemistry and Quantum Optics, and the Deutsches Museum. It merges their combined expertise on nanoscale systems into a coherent and focused nanoscience cluster. While many individual nanoscale building blocks and components have been devised in recent years using top-down and bottom-up strategies, little is known about their integration into entire functional systems. The overarching vision guiding the research in NIM is therefore to design, fabricate and achieve control of a broad range of artificial and multi-functional nanoscale systems, and to unlock their potential for possible applications in fields as diverse as future information technologies, the life sciences, or combinations of both. To this end, it is essential to gain a fundamental understanding of their properties and behavior, which range from being purely quantum mechanical to being governed mainly by stochastic effects.

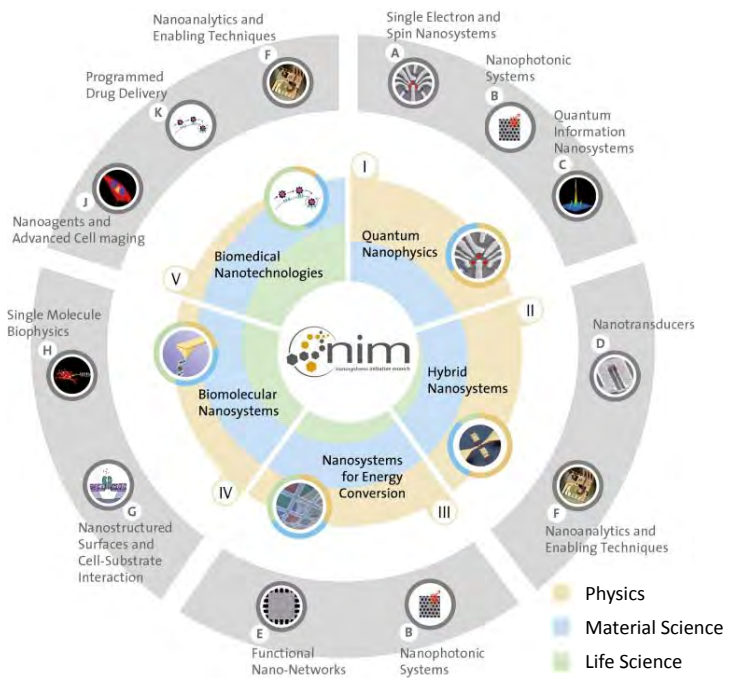

The first funding period of NIM ends in October 2012. The funding proposal for the second five-year funding proposal has been completed and submitted to the German Research Foundation (DFG) in August 2011. It will be reviewed in January 2012. Since November 2010, NIM's research activities have been reorganized in five research areas (RAs) as illustrated in the figure: RA I – ***Quantum Nanophysics***, RA II – ***Hybrid Nanosystems***, RA III – ***Nanosystems for Energy Conversion***, RA IV – ***Biomolecular Nanosystems***, and RA V – ***Biomedical Nanotechnologies***. At WMI, several scientists (Deppe, Gönnenwein, Gross, Hübl, Marx) actively contributed to set up an attractive research program for the second funding period of NIM. The physics of quantum nanosystems is one of the main future research directions of NIM, in perfect agreement with the focus of several research activities at WMI. The major contributions of WMI are to RA I: ***Quantum Nanophysics*** and RA II: ***Hybrid Nanosystems***. Research area I is coordinated by R. Gross of WMI.

[1]This work is supported by the German Excellence Initiative via the Nanosystems Initiative Munich (NIM).

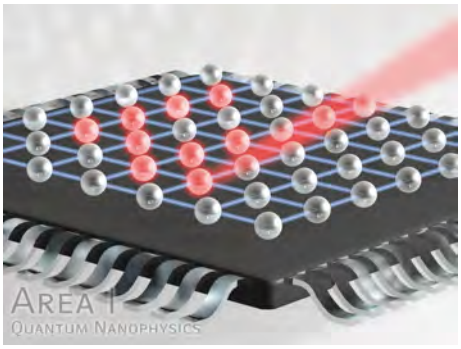

The scientific program of ***Research Area I*** is focused on quantum nanosystems. It aims at the modeling and understanding of such nanosystems on a quantum level. The modelling and understanding of nanosystems on a quantum level is a key prerequisite for their application in hybrid devices, energy conversion systems as well as in biomolecular and biomedical systems. The scientific program of research area I addresses this fundamental problem by systematically studying quantum systems based on solid state nanostructures and tailor-made meso-scale many body systems realized in optical lattices. In future, these research efforts particularly focus on (i) the design and fundamental mechanisms of nanoscale quantum matter, (ii) the development of hybrid quantum nanosystems, (iii) the study of nonequilibrium dynamics, and (iv) the foundations of quantum X-tronics (X = spin, charge, flux, plasmon, magnon, etc.). They aim to establish a thorough understanding of quantum nanosystems and to develop the techniques required for their realization, manipulation and control. To this end, a key objective of research area I is to provide the physical foundations and technological platform for novel quantum-based technologies and functionalities relevant for the other NIM research areas.

Examples of the planned WMI activities within NIM are the fabrication of linear arrays of interacting flux qubits as toy models for many-body quantum systems or the systematic study of the interaction between nanoscale solid state quantum systems and the modes of electromagnetic fields on a single quantum level (in collaboration with Finley, Hänsch, Högele, Holleitner, Wixforth, Cirac, Hänggi, Zwerger). In this field the research activities within NIM are closely linked to those of SFB 631 described already above (see pp. 11–14). The WMI research activities also aim at the study of pure spin currents in the quantum regime. It is planned to perform spin pumping experiments in ferromagnet/normal metal or antiferromagnet/normal metal structures in the limit of mK temperatures and single microwave photons. Furthermore, the study of "Quantum Ferromagnetic Resonance", which can be viewed as a coherent exchange of excitations between a harmonic oscillator and a ferromagnet, is an interesting field. Ferromagnetic resonance has not yet been studied in the quantum limit. Using ferromagnetic nanostructures embedded into superconducting waveguide resonators, single photon/single magnon experiments are expected to become possible. To this end, considerable progress has been achieved within the last year (see reports by Gönnenwein *et al.*, pp. 42–43, and Weiler *et al.*, pp. 44–45).

The ***Research Area II*** on Hybrid Nanosystems can be viewed as NIM's main nano-foundry, where a great variety of solid state and nano-bio-systems are to be fabricated by advanced top-down and smart bottom-up approaches. A key goal is to exploit the potential and to realize functional nanosystems with optimized performance. To this end, nanosystems with various degrees of freedom such as optical, electrical or mechanical will cross-fertilize. It includes different quasi particles and excitations ranging from photons over plasmons, magnons, and phonons to charge carriers, going along with a transfer of methods, materials and technologies. It utilizes the power of biological self-assembly to realize active devices or photons to control the mechanical and

magnetic properties of nanoscale matter. RA II aims towards the realization of such hybrid nano-systems consisting of more than one constituent to meet the expectations given above. The representative examples all share the common ground of adding value by hybridization, combination and cross-linking between the projects as well as the four other areas of NIM. The aim is to integrate individual nanoscale building blocks and biomolecular assemblies into entire functional systems acting in complex environments, resulting in physical sensors and actuators to investigate and promote transport within various nanosystems.

Within RA II, WMI proposes to investigate the interaction of light with magnonic excitations using near-field and nano-optical effects (in collaboration with Grundler, TUM). Metallic nanostructures integrated into magnetic devices are used to locally enhance the light-induced electrical field due to plasmonic effects and to extend the wavevector spectrum by exploiting evanescent waves. Also, the coupling of magnonic and phononic modes shall be investigated in ferromagnetic/ferroelectric hybrid devices (in a cooperation with Krenner/Wixforth, University of Augsburg, and Weig, LMU). In such devices, a surface acoustic wave (SAW) propagating in the ferroelectric induces local, radio-frequency, elastic strains in the adjacent ferromagnet. This allows to elastically drive magnetization dynamics, and makes hypersound ferromagnetic resonance experiments with submicron spatial resolution possible. Ferromagnetic/ferroelectric hybrids thus are an ideal testbed to study the coupling of magnon and phonon dispersions (see report by Weiler *et al.*, pp. 44–45).

A new research field started at WMI some years ago is nano-mechanics. In a collaboration with E. Weig, LMU, and T. Kippenberg, EPFL Lausanne, we have successfully fabricated electro-mechanical nanosystems consisting of a superconducting nanobeam coupled to a high quality factor superconducting microwave resonator. These systems have been studied at mK temperatures and interesting features such as electro-mechanically induced transparency have been observed very recently.

The DFG Priority Program SPP 1285 "Semiconductor Spintronics"

M. Althammer, S. T. B. Goennenwein, R. Gross, M. Opel, D. Venkateshvaran [1]
B. Beschoten, G. Güntherodt, V. Klinke, C. Schwark [2]

The use of electron and hole spins for future semiconductor devices is in the focus of current research. Key prerequisites for the development of novel device concepts for spin electronics and spin optoelectronics are the realization of an effective injection of spin-polarized charge carriers, as well as the thorough understanding of the transport, manipulation, and detection of the spin degree of freedom. To promote research in this field, the German Research Foundation (DFG) started the priority program SPP 1285 on "Semiconductor Spintronics" in 2007. The generell scientific objectives of this priority program are (i) the efficient injection of spin polarized electrons using para- and ferromagnetic semiconductors and ferromagnetic metal clusters, (ii) the transport of electron spins across interfaces and large distances, (iii) the direct manipulation of the orientation of electron spins, (iv) the study of spin-spin-interaction, (v) the development of concepts for spin electronics and spin-optoelectronics, and (vi) the study of basic principles of spin-quantum information processing in semiconductors.

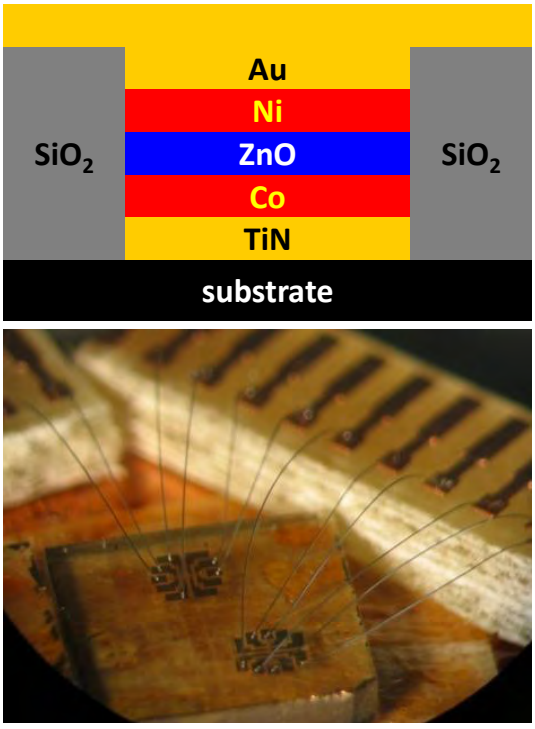

Figure 1: Cross-sectional view (top) and optical micrograph of a ZnO based spin-valve structure used for the study of spin transport through ZnO (Eva-Maria Karrer-Müller, diploma thesis, TU Munich 2011).

The priority program SPP 1285 is presently funding 33 single projects all over Germany in basic and applied research. The Walther-Meißner-Institut (WMI) participates in this program from the beginning with the project ***Spin Injection, Spin Transport and Controllable Ferromagnetism in Transition Metal Doped ZnO*** (cf. report by Althammer *et al.*, pp. 64–66). The key objectives of this project include (i) the fabrication of epitaxial ZnO thin films and heterostructures as well as $[\mathrm{ZnO/ferromagnet}]_n$ digital alloys tailored to the needs of spin (opto)electronic devices, (ii) the study of the spin lifetime and spin coherence length in ZnO by optical pump & probe experiments, (iii) the optical study of electrical spin injection and spin transport in ferromagnet/ZnO heterostructures, and (iv) the investigation of all-electrical spin injection and spin transport in high quality epitaxial ZnO thin films. The work is done in close collaboration with various partners within SPP 1285. The WMI funding proposal for the third two-year funding period (2011–2013) has been reviewed early in 2011 and been granted by the German Research Foundation.

[1] This work was supported by the German Research Foundation via Priority Program SPP 1285 (project number GR 1132/14).
[2] 2. Physikalisches Institut A, RWTH Aachen, Germany.

The DFG Priority Program SPP 1458 "Superconductivity in Iron-Based Compounds"

R. Hackl, B. Muschler, F. Kretzschmar, A. Baum, T. Böhm, R. Gross[1]
B. Büchner[2], *C. Honercamp*[3], *D. Johrendt*[4]

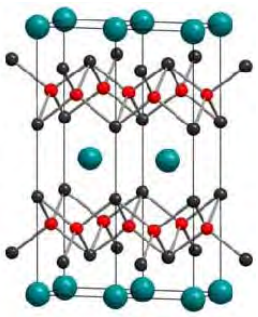

The iron-based or pnictide superconductors [1, 2] are unanticipated members in the family of compounds with high transition temperature T_c. For the relatively isotropic electronic properties, they are promising for applications and expected to outperform even the cuprates in some aspects. Since the electron-phonon coupling is weak, the superconducting pairing has unconventional components. Motivated be these aspects, the Priority Program "High-Temperature Superconductivity in the Iron Pnictides" was initiated by four of the authors. In 2010 the DFG decided to fund the proposed research via SPP 1458, and 35 groups including 5 associated members are presently supported. The research activities proved that the properties of the pnictides are intriguing far beyond the expectations. Similarly as in the cuprates, magnetism and superconductivity are in close proximity as shown for $Ba(Fe_{1-x}Co_x)_2As_2$ in Fig. 1 (a). Moreover, the compounds turn out to be a laboratory for stud-

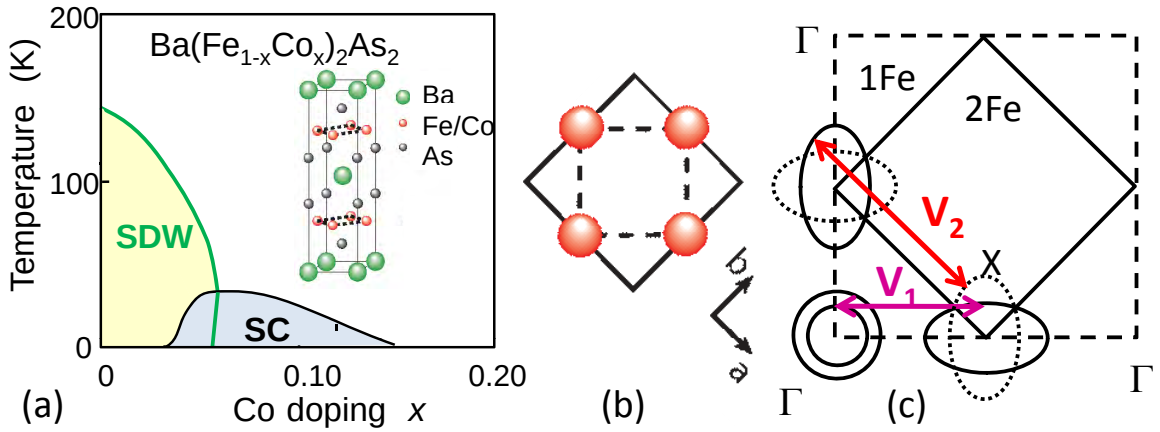

Figure 1: (a) Phase diagram of $Ba(Fe_{1-x}Co_x)_2As_2$. The crystal structure is shown in the inset. The Fe planes are indicated by dashes. (b) Individual Fe plane with crystallographic cell (full line) and orientation of the axes. One crystal cell contains two Fe atoms. For the electronic properties the smaller 1 Fe cell (dashes) is more appropriate. (c) Reciprocal space of the Fe plane. The dashes represent the first Brillouin zone (BZ) of the 1Fe cell shifted by (π, π) with the hole and the electron bands (lull lines) around the Γ and the X point, respectively. Upon increasing the unit cell volume the BZ has to be back-folded, and a second electron band results (dashed ellipses). The coupling between the hole and the electron bands is V_1 and indicated in purple. For the similarity of the Fermi surfaces the coupling among the electron bands V_2 (red) can be similarly strong as V_1.

ies of unconventional superconductivity. For instance, the Fermi surfaces [Fig. 1 (c)] can be tuned in a systematic way by doping. This affords a window into the nature of the pairing state which, according to various theoretical and experimental studies, is directly influenced or even determined by the shape of the Fermi surfaces [3–7]. In particular, the coupling potentials between electron and hole bands V_1 and among the electron bands V_2 are similar in

[1]This work is supported by the German Research Foundation (DFG) via the Priority Program SPP 1458.
[2]Leibniz Institute for Soild State and Materials Research (IFW), 01069 Dresden, Germany
[3]Institute for Theoretical Solid State Physics, RWTH Aachen, 52074 Aachen, Germany
[4]Department of Chemistry, LMU München, 81377 München, Germany

magnitude [Fig. 1 (c)]. As a consequence, the two possible pairing states are nearly degenerate and may be realized for different doping levels. Very importantly, new materials with T_c values beyond 30 K continue to be synthesized [8, 9]. Hence, research into the iron-based compounds is a vibrant field having an impact on the development of superconductivity in general.

The Walther-Meißner-Institute hosts one of the coordinators (R.H.) and participates with the project "Light scattering studies of iron pnictides". The Raman scattering group studied predominantly the electronic properties of $Ba(Fe_{1-x}Co_x)_2As_2$ as a function of doping [10–12]. The strong variations of the electron dynamics observed above and below T_c in the doping range $0 \leq x \leq 0.085$ confirm theoretical predictions and demonstrate that direct electron-electron interactions between different sheets of the Fermi surface dominate the properties. However, the evolution of the superconducting energy gap being a main signature of the interaction potential (e.g. V_1 and V_2) turns out to be complicated in spite of intense joint efforts in the Priority Program. It remains as a major obstacle on the way towards a deeper understanding of unconventional superconductivity. This important open question can be one of the starting points for the second funding period to be prepared in 2012.

References

[1] Y. Kamihara, T. Watanabe, M. Hirano, and H. Hosono, J. Am. Chem. Soc. **130**, 3296 (2008).
[2] M. Rotter, M. Tegel, and D. Johrendt, Phys. Rev. Lett. **101**, 107006 (2008).
[3] A. D. Christianson, E. A. Goremychkin, R. Osborn, S. Rosenkranz, M. D. Lumsden, C. D. Malliakas, I. S. Todorov, H. Claus, D. Y. Chung, M. G. Kanatzidis, R. I. Bewley, and T. Guidi, Nature **456**, 930 (2008).
[4] W.-C. Lee, S.-C. Zhang, and C. Wu, Phys. Rev. Lett. **102**, 217002 (2009).
[5] T. A. Maier, and D. J. Scalapino, Phys. Rev. B **84**, 180513 (2011).
[6] C. Platt, R. Thomale, C. Honerkamp, S.-C. Zhang, and W. Hanke, arXiv:1106.5964 (2011).
[7] G. Friemel, J. T. Park, T. A. Maier, V. Tsurkan, Y. Li, J. Deisenhofer, H.-A. Krug von Nidda, A. Loidl, A. Ivanov, B. Keimer, and D. S. Inosov, arXiv:1112.1636 (2011).
[8] J. Guo, S. Jin, G. Wang, S. Wang, K. Zhu, T. Zhou, M. He, and X. Chen, Phys. Rev. B **82**, 180520 (2010).
[9] C. Löhnert, T. Stürzer, M. Tegel, R. Frankovsky, G. Friederichs, and D. Johrendt, Angew. Chem. Int. Ed. **50**, 9195–9199 (2011).
[10] B. Muschler, W. Prestel, R. Hackl, T. P. Devereaux, J. G. Analytis, J.-H. Chu, and I. R. Fisher, Phys. Rev. B **80**, 180510 (2009).
[11] I. I. Mazin, T. P. Devereaux, J. G. Analytis, J.-H. Chu, I. R. Fisher, B. Muschler, and R. Hackl, Phys. Rev. B **82**, 180502 (2010).
[12] B. Muschler, F. Kretzschmar, R. Hackl, J.-H. Chu, J. G. Analytis, and I. R. Fisher, Annual Report WMI 2010, 49–50 (2010).

The DFG Priority Program SPP 1538 "Spin Caloric Transport"

S. T. B. Goennenwein, R. Gross, J. Lotze, S. Meyer [1]

Spin polarized currents in magnetic nanostructures give rise to novel spin caloric effects. These effects modify thermal transport, magneto-resistance and possibly even magnetic states. To understand the observed effects an extension of thermodynamic laws including the spin is inevitable. It is long known that heat and charge currents are closely linked to each other by, e.g., the Wiedemann-Franz law which connects thermal and electrical conductivities in metals. The coupling leads to thermoelectric effects with prominent examples being the Seebeck effect and its inverse, the Peltier effect, which may be described through the Onsager relations. These effects are used in devices such as thermocouples and thermo-electric cooling devices, respectively. It became clear only recently that these long-known thermoelectric phenomena need to be re-considered by including the spin. This avenue is expected to generate completely new spin-related properties in the solid state. The hypothesis that in magnetic systems spin entropy can be created, manipulated and transported by non-equilibrium charge and heat currents is compelling. Non-equilibrium magneto-caloric transport effects such as the Nernst-Ettingshausen effects will face novel spin and anomalous counterparts. Spin transport phenomena in the presence of a thermal gradient or the lateral transport of heat via magnetic excitations need to be studied.

To stimulate research activities on spin caloric phenomena, the Senate of the German Research Foundation (DFG) has started the new Priority Program SPP 1538 entitled ***Spin Caloric Transport (SpinCaT)*** in 2011. The aim of SPP 1538 is to develop the new research field of caloric effects in spin transport. The research program is focused on four priority areas: (i) spin caloric effects and spin mediated heat transport in planar geometry, (ii) thermal spin-based conductivities across interfaces in nanopatterned magnetic devices, (iii) spin currents induced by large temperature gradients, and (iv) materials for spin caloric applications. The Walther-Meißner-Institute (WMI) participates in this program with the project ***Spin-dependent Thermo-galvanic Effects***. The first three-year funding period started in mid 2011.

[1] This work was supported by the German Research Foundation via Priority Program SPP 1538 (project number GO 944/4-1).

Basic Research

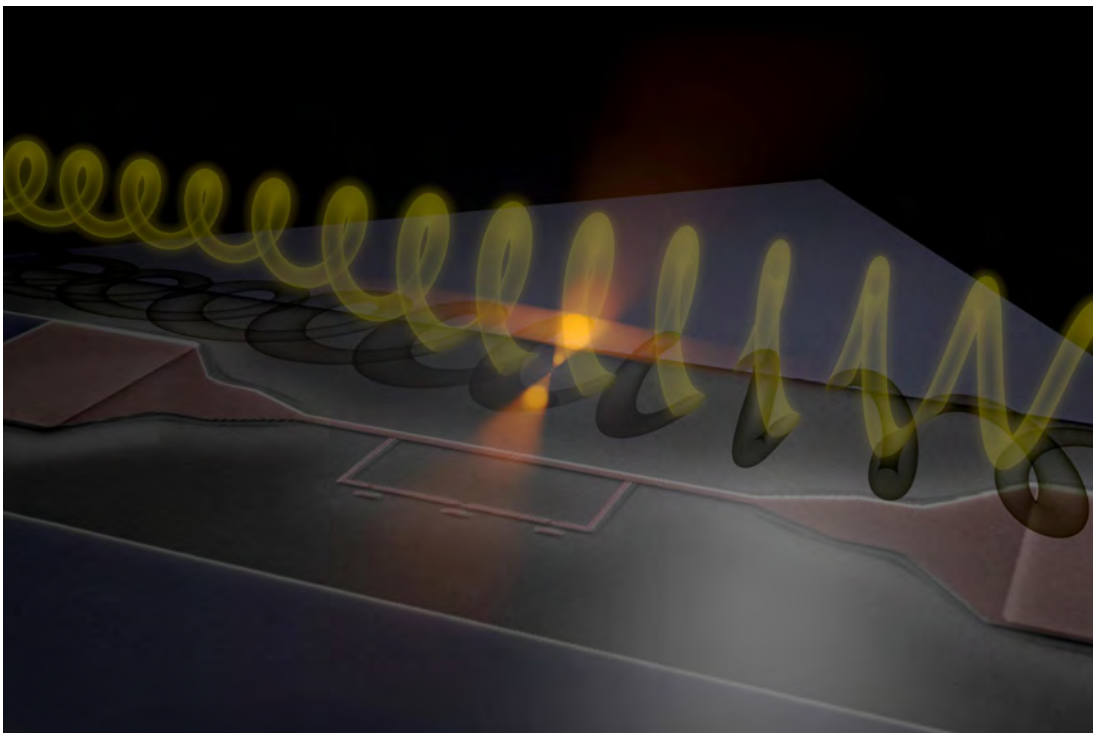

An artist's view of the interaction between a superconducting flux qubit incorporated into a stripline resonator with a microwave photon.

Analytic Ginzburg–Landau Description of Superconducting Cylinders

D. Einzel, R. Doll

Introduction. In a series of papers [1–4], one of the authors (D. E.) has investigated analytical approaches to the results of the BCS and GLAG theory, as applied to both conventional and unconventional superconductors. In ref. [4] the authors investigated in particular an analytic solution of the Ginzburg–Landau equations as applied to the problem of fluxoid quantization in *hollow* superconducting cylinders. This contribution is devoted to an analytical approach to the description of a *full* superconducting cylinder, which is exposed to an external magnetic field $\mathbf{H}^{\rm ext}$. Applied to the case of cylindrical symmetry, one may decompose the order parameter or pair field Ψ as follows

$$\Psi(r,\theta,T) = \sqrt{\frac{7\zeta(3)}{8}} n \frac{\Delta(r,\theta,T)}{\pi k_{\rm B} T_{\rm c}} = a_0(T) f(r,T) e^{i\varphi(\theta)} \;\; ; \;\; a_0^2(T) = \frac{n^{\rm s}(T)}{2} = n\left(1-\frac{T}{T_{\rm c}}\right) \qquad (1)$$

Here r and θ denote the radial and the azimuthal angular variable, respectively. $n^{\rm s}$ and Δ represent the superfluid density and the energy gap in the GL regime.

When applied to a cylinder of radius R, the pair of Ginzburg–Landau (GL) equations for Ψ reads in the variables (r,θ) ($f' = df/dr, A' = dA/dr$):

$$0 = \xi_{\rm GL}^2\left(f'' + \frac{f'}{r}\right) + f - f^3 - \frac{(2\pi\xi_{\rm GL})^2}{\Phi_0^2}\left[A - \frac{n\Phi_0}{2\pi r}\right]^2 f \quad \text{first GL Eq.} \qquad (2)$$

$$\frac{dB}{dr} = A'' + \frac{A'}{r} - \frac{A}{r^2} = \frac{f^2}{\lambda_{\rm L}^2}\left[A - \frac{n\Phi_0}{2\pi r}\right] \quad \text{second GL Eq.} \qquad (3)$$

$$\xi_{\rm GL}^2(T) = \frac{\hbar^2 v_{\rm F}^2}{6\Delta^2(T)} \;\; ; \;\; \lambda_{\rm L}^2 = \frac{mc^2}{4\pi n^{\rm s} e^2} \;\; ; \;\; \Phi_0 = \frac{hc}{2e}$$

Here $\xi_{\rm GL}$, $\lambda_{\rm L}$ and Φ_0 represent the GL coherence length, the magnetic penetration depth and the fluxoid quantum, respectively. The latter term arises together with the quantum number $n = 0, \pm1, \pm2, \ldots$ as a consequence of the uniqueness requirement for the pair field

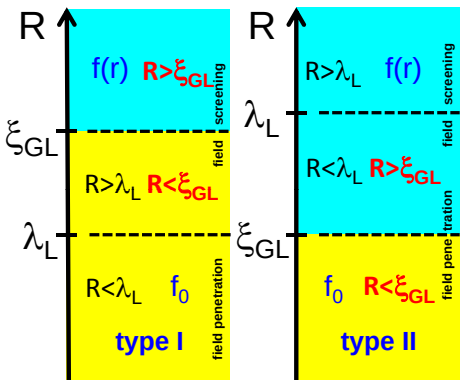

Figure 1: The three relevant length scales R, $\xi_{\rm GL}$ and $\lambda_{\rm L}$ in the GL description of superconducting full cylinders and associated regimes of constant and r–dependent order parameter $f(r)$ and magnetic field $B(r)$ in type I and type II superconductors.

Ψ [4]. $\Delta(T)$ and v_F represent the equilibrium gap in the GL regime and the Fermi velocity, respectively. The axial magnetic field $B(r) = dA(r)/dr + A(r)/r$ is generated as usual from the azimuthal component $A(r)$ of the vector potential. Aiming at the treatment of a full superconducting cylinder of radius R, we restrict further considerations to the case $n = 0$. An inspection of (2) and (3) shows, that the cylinder radius R has to be compared with two length scales for the spatial dependence of the first and second GL equation, respectively, namely the GL coherence length ξ_{GL} (first) and the magnetic penetration depth λ_L (second). The ratio $\kappa = \lambda_L/\xi_{GL}$ of these two quantities provides a distinction between type–I ($\kappa < 1/\sqrt{2}$) and type-II ($\kappa > 1/\sqrt{2}$) superconductivity. In Fig. 1 we have plotted the different regimes of these length scales. The yellow areas are characterized by the condition $\xi_{GL} > R$, which justifies the assumption $f(r) \approx f_0$ inside ($0 \le r \le R$) the superconducting cylinder. The blue areas refer to the more complicated case $\xi_{GL} < R$, in which the radial dependence of *both* the order parameter $f(r)$ *and* the vector potential $A(r)$ has to be accounted for. In this case only a numerical treatment of these two coupled differential equations seems to be applicable. A comprehensive and predominantly numerical treatment of the latter problem was provided by Robert Doll and Peter Graf [5]. In this contribution we wish to present an analytical treatment, which is based on the Taylor representations of the functions $f(r)$ and $A(r)$.

Taylor representation method. For general values of κ, the pair of GL equations can be solved using the following Taylor series representations:

$$f(r) = \sum_{k=0}^{\infty} f_{2k} \left(\frac{r}{\xi_{GL}}\right)^{2k} ; A(r) = \sum_{k=0}^{\infty} a_{2k+1} \left(\frac{f_0 r}{\lambda_L}\right)^{2k+1} ; B(r) = \frac{f_0}{\lambda_L} \sum_{k=0}^{\infty} (2k+2) a_{2k+1} \left(\frac{f_0 r}{\lambda_L}\right)^{2k} \quad (4)$$

Inserting these Taylor expansions into the first and second GL equation allows one, after an admittedly tedious calculation, to identify the Taylor coefficients a_{2k+1} and f_{2k}:

$$a_{2k+1} = \frac{g_{2k+1} a_1}{2^{2k} k!(k+1)!} \; ; \; f_2 = -\frac{f_0(1-f_0^2)}{4} \; ; \; f_4 = \frac{f_0(1-4f_0^2+3f_0^4)}{64} + \frac{f_0}{4} \frac{a_1^2}{H_0^2 \lambda_L^2} \frac{\xi_{GL}^4}{R^4} \quad (5)$$

Clearly, the Taylor coefficients f_{2k} are related to f_0 for $k > 0$. f_0 turns out to be fixed by the boundary condition

$$\left[\frac{df}{dr}\right]_{r=R} = \sum_{k=0}^{\infty} 2k f_{2k} \frac{R^{2k-1}}{\xi_{GL}^{2k}} = 0 \quad (6)$$

The quantities g_{2k+1} are found to be rather complex in structure. The first few of them read: $g_3 = 1$,

$$g_5 = 1 - 4\kappa^2 \frac{1-f_0^2}{f_0^2} \; ; \; g_7 = 1 - 16\kappa^2 \frac{1-f_0^2}{f_0^2} + 6\kappa^4 \frac{(1-f_0^2)(3-5f_0^2)}{f_0^4} + 96 \frac{a_1^2 \lambda_L^2}{R^4 H_0^2 f_0^4} \quad (7)$$

It should be emphasized, that the results for the Taylor coefficients f_{2k} and a_{2k+1}, $k = 0, 1, 2 \ldots$ have first been derived by Robert Doll and Peter Graf [5]. However, these authors did not recognize, that the quantities $(z/2)^{2k+\nu}/k!(k+\nu)!$ can be identified as the individual terms in the Taylor expansion of the *Modified Bessel functions* $I_\nu(z)$ [6]. Moreover, they restricted their investigations to the special case $f_0 = \frac{1}{2}$, $\kappa = \lambda_L/\xi_{GL} = \frac{1}{2}$ and $a_1 = \sqrt{2} H_{cb} \lambda_L/4$. It turns out, that a much more general treatment is possible: from the coefficients a_{2k+1}, $k = 0, 1, 2, \ldots$ we may construct the following *generalized Modified Bessel functions* $\mathcal{I}_0(z)$ and $\mathcal{I}_1(z)$, $z = f_0 r/\lambda_L$:

$$\mathcal{I}_\nu(z) = \sum_{k=0}^{\infty} \frac{g_{2k+1}}{k!(k+\nu)!} \left(\frac{z}{2}\right)^{2k+\nu} \quad ; \quad \nu = 0, 1, 2, \ldots \quad (8)$$

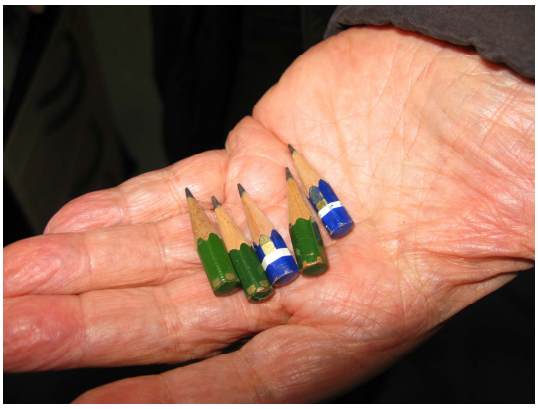

Figure 2: The vestige of the pencils used by one of the authors in order to derive Eqs. (2) and (4).

Clearly, one has $\mathcal{I}_\nu(z) \to I_\nu(z)$ in the limit $g_{2k+1} \to 1$. Making use of the property $d\mathcal{I}_1(z)/dz = \mathcal{I}_0(z) - \mathcal{I}_1(z)/z$, we may derive from these definitions the compact results for $A(r)$ and $B(r)$:

$$A(r) = 2a_1\mathcal{I}_1\left(\frac{f_0 r}{\lambda_\mathrm{L}}\right) \;\; ; \;\; B(r) = 2a_1\frac{f_0}{\lambda_\mathrm{L}}\mathcal{I}_0\left(\frac{f_0 r}{\lambda_\mathrm{L}}\right) \tag{9}$$

Clearly, the external field H^ext can be connected with the unknown integration constant a_1 via

$$B(R) \equiv H^\mathrm{ext} = 2a_1\frac{f_0}{\lambda_\mathrm{L}}\mathcal{I}_0\left(\frac{f_0 R}{\lambda_\mathrm{L}}\right) \;\; \leftrightarrow \;\; 2a_1 = \frac{\lambda_\mathrm{L}}{f_0}\frac{H^\mathrm{ext}}{\mathcal{I}_0\left(\frac{f_0 R}{\lambda_\mathrm{L}}\right)} \tag{10}$$

As a consequence we obtain

$$A(r) = \frac{\lambda_\mathrm{L}}{f_0}\frac{\mathcal{I}_1\left(\frac{f_0 r}{\lambda_\mathrm{L}}\right)}{\mathcal{I}_0\left(\frac{f_0 R}{\lambda_\mathrm{L}}\right)}H^\mathrm{ext} \;\; ; \;\; B(r) = \frac{\mathcal{I}_0\left(\frac{f_0 r}{\lambda_\mathrm{L}}\right)}{\mathcal{I}_0\left(\frac{f_0 R}{\lambda_\mathrm{L}}\right)}H^\mathrm{ext} \tag{11}$$

As a special case, the magnetic field on the cylinder axis is obtained as $B(0) = H^\mathrm{ext}/\mathcal{I}_0\left(f_0 R/\lambda_\mathrm{L}\right)$. Clearly, its value depends on the ratio R/λ_L and is small (large) for small (large) values of the magnetic penetration depth. The validity of the Taylor expansion method is demonstrated in Fig. 3, where we have plotted both the exact results for the magnetic field $B(r)$ and the vector potential $A(r)$ together with their Taylor representations (up to and including the sixth order) vs. r/R in the case $g_{2k+1} = 1, \forall i \geq 0$, i. e. in the extreme type–I limit. In the case $\lambda_\mathrm{L}/f_0 R = 0.1$ the deviation of the exact results for $B(r)$, $A(r)$ and their Taylor representations is considerable, not unexpectedly, however, only far away from the cylinder axis. However, this case corresponds to the physics of extreme field screening and is topologically equivalent to the case of a superconducting half space, for which the cylindrical symmetry is irrelevant. For $\lambda_\mathrm{L}/f_0 R = 0.4$, on the other hand, the agreement between the exact results and their Taylor representations is excellent, the error ranging, for example, below 0.18% for $0 < r/R < 1$ in the case of $B(r)$. It is worth emphasizing, that in the absence of an external magnetic field ($a_1 = 0$), $f(r)$ may in principle display an inhomogeneous (in fact bell–shaped) radial profile. However, the boundary condition $(df/dr)_R = 0$ for $f(r)$ wipes this possibility out in that it is seen to imply, that the Taylor coefficient f_2 factorizes out from

$$2|f_2|\underbrace{\left\{1 - 2\frac{R^2}{\xi_\mathrm{GL}^2}\frac{1-3f_0^2}{16} + 3\frac{R^4}{\xi_\mathrm{GL}^4}\frac{1-18f_0^2+21f_0^4}{576} - \ldots\right\}}_{\neq 0} = 0 \tag{12}$$

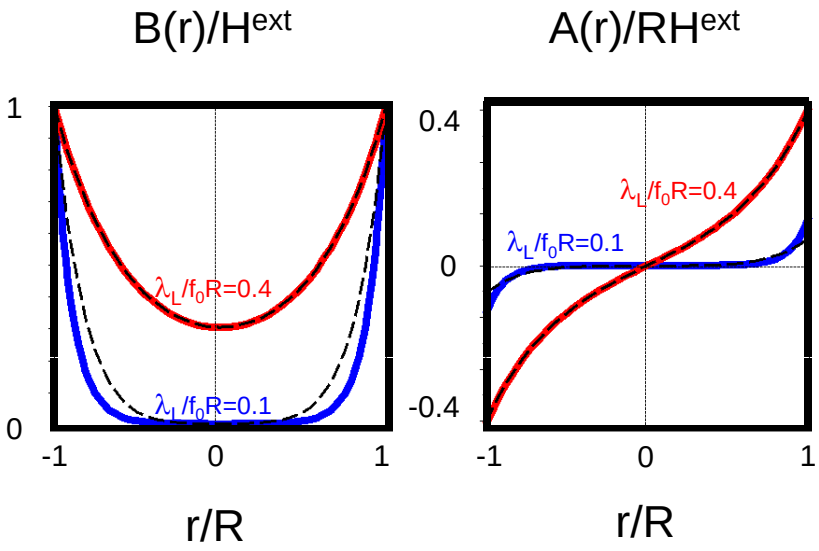

Figure 3: Normalized magnetic field $B(r)/H^{\rm ext}$ (left) and vector potential $A(r)/RH^{\rm ext}$ (right) vs. radial variable r/R for two values of the parameter $\lambda_{\rm L}/f_0R$. The dashed lines represent an evaluation of $B(r)$ and A(r) using the Taylor representation up to the sixth order in $f_0 r/\lambda_{\rm L}$.

Hence $f_2 = 0$, which immediately leads to the homogeneous result $f_0 \equiv 1$ for the order parameter in the absence of an external magnetic field.

References

[1] D. Einzel, J. Low Temp. Phys. **126**, 867–879 (2002).
[2] D. Einzel, J. Low Temp. Phys. **130**, 493–508 (2003).
[3] D. Einzel, J. Low Temp. Phys. **131**, 1–24 (2003).
[4] R. Doll, and D. Einzel, J. Supercond. Nov. Magn. **19**, 173–179 (2006).
[5] R. Doll, and P. Graf, Z. Phys. A Hadrons and Nuclei **197**, 172–191 (1966).
[6] M. Abramowitz, and I. A. Stegun (eds.) *Handbook of Mathematical Functions* (Dover Inc., New York).

Quantum and classical magnetoresistance oscillations in the electron-doped cuprate superconductor $Nd_{2-x}Ce_xCuO_4$

T. Helm, M. V. Kartsovnik, W. Biberacher, A. Erb, and R. Gross [1]
C. Putzke, E. Kampert, F. Wolff-Fabris, and J. Wosnitza [2]
A. Kiswandhi, and J. S. Brooks [3]

For hole-doped cuprate compounds a large number of high-field experiments has been accomplished, gaining new insights into the Fermiology of this material class. The breakthrough for the electron-doped cuprates came three years ago thanks to a new level in the quality of growing single-crystalline $Nd_{2-x}Ce_xCuO_4$ (NCCO) achieved in the Walther-Meißner-Institute [1]. The discovery of the Shubnikov-de Haas (SdH) effect for several differently doped crystals of NCCO revealed the existence of a well-defined Fermi surface (FS) and its dependence on the electron concentration [2]. After optimization of the sample preparation and the high-field measurement setup we were able to show that a translational symmetry breaking persists even for strong overdoping up to the higher edge of the superconducting region of the phase diagram [3]. It was found that at high enough magnetic fields magnetic breakdown occurs, enabling electrons to tunnel through the gap between electron- and hole-like parts of the reconstructed FS. In steady fields up to 34 T semiclassical angle-dependent magnetoresistance oscillations (AMRO) were found originating from a weakly warped cylindrical FS [3, 4]. This year's experiments in steady and pulsed fields up to 45 and 70 T, respectively, provided a link between magnetic breakdown and the AMRO effect in NCCO and extended our knowledge about the phase diagram.

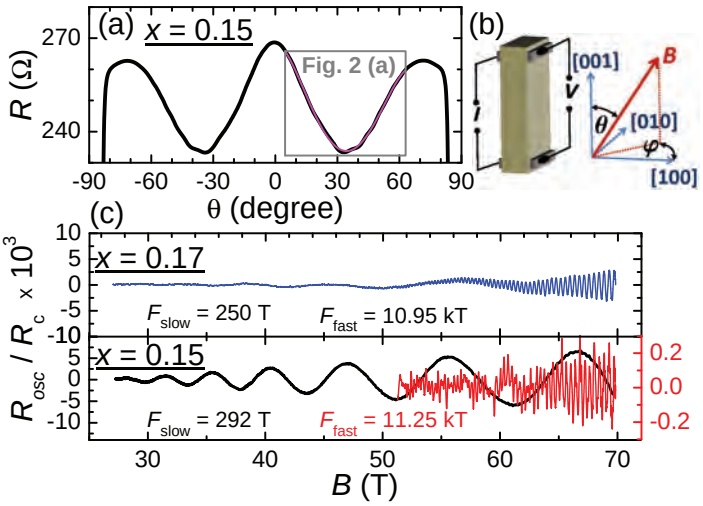

Figure 1: (a) Angle-dependent interlayer magnetoresistance of $Nd_{2-x}Ce_xCuO_4$ for $x = 0.15$ as a function of tilt angle θ at $B = 45$ T and $T = 1.9$ K; square at $0° \leq \theta \leq 60°$ marks angle-dependent SdH oscillations. (b) Sketch of the experimental configuration. (c) Slow and fast SdH oscillations for $x = 0.17$ (blue curve) and 0.15 (black curve) measured in pulsed fields; the red curve shows fast oscillations for $x = 0.15$ after filtering out the low frequency.

Fig. 1(a) exhibits the interlayer magnetoresistance of an $x = 0.15$ sample as a function of the polar angle θ [see the experimental geometry in Fig. 1(b)] measured in a static magnetic field of 45 T. Even at such a strong field we do not find AMRO on top of the magnetoresistance background, by contrast to higher doped, $x = 0.17$, samples where AMRO are clearly seen starting from fields $23 - 25$ T [4]. A possible explanation for the absence of AMRO at optimal doping is that its origin lies in a large breakdown orbit. This idea has been confirmed by studying the evolution of the breakdown with doping. From the relative amplitudes of the fast and slow oscillations we obtain an estimate of the magnetic breakdown field: $B_0 \approx 1$ T, 7 T and 15 T for

[1] This work was supported by the German Research Foundation via grant GR 1132/15, as well as by EuroMagNET II under the EC contract 228043 and by NHMFL user grant.
[2] Hochfeld-Magnetlabor Dresden, Forschungszentrum Dresden-Rossendorf, D-01328 Dresden, Germany
[3] Department of Physics and National High Magnetic Field Laboratory, Florida State University, Tallahassee, Florida 32310, USA

$x = 0.17$, 0.16 and 0.15, respectively. For $x = 0.16$ AMRO are very weak and only discernible at fields of 28 T or higher, i.e. at $B >> B_0$. Since B_0 for $x = 0.15$ is about two times larger than for 0.16 it should become possible to observe AMRO around 56 T. This is the reason why no AMRO are found up to 45 T in optimally doped samples. From the breakdown fields the energy gap between the electron- and hole-like bands arising from a superlattice potential is estimated as $\Delta = 5$, 10 and $15 - 17$ meV for the latter three doping levels. Most interestingly, for decreasing electron concentration the value of the gap is growing towards optimal doping as the critical temperature of superconductivity does. To get further information on a possible connection between the ordering and superconductivity, experiments are desired that investigate the region below optimal doping.

Taking a closer look at the $R(\theta)$ curve for $x = 0.15$ in Fig. 1(a) one can resolve slow angle-dependent SdH oscillations. The oscillatory part of the magnetoresistance fragment at $0° \leq \theta \leq 60°$, [data in the square frame in Fig. 1(a)] is plotted in Fig. 2(a) against the out-of-plane field component. It nicely coincides with the SdH oscillations recorded in a field sweep at $B||c$ [blue curve in Fig. 2(a)]. In Fig. 2(b) the frequency of the slow oscillations obtained from field sweeps at several fixed angles is plotted versus θ. It clearly demonstrates the $1/\cos\theta$ law characteristic of an almost perfectly cylindrical FS. Fig. 2(c) shows the angular dependence of the oscillation amplitude at $B = 40$ T. The green line is a fit of the experimental data to the Lifshitz-Kosevich formula, taking into account the spin-splitting factor. With an effective mass equal to the free electron mass [4] and a Dingle factor of 12 T, obtained from the field dependence in the 70 T pulse [Fig. 1(c) lower panel], the fit yields the gyromagnetic ratio $g = 1.6$. Its significant deviation from the electron-spin-resonance value $g \approx 2.0$ is most likely caused by many-body interactions. We note, however, that the above estimate is rather rough; a more accurate value can be obtained from "spin-zero" positions [e.g. $\theta = 58°$ for $g = 1.6$, see Fig. 2(c)]. Unfortunately the oscillation amplitude at 40 T was too small to resolve spin-zeros at $\theta > 56°$. Therefore, further experiments at higher (pulsed) magnetic fields are necessary for a reliable evaluation of the g-factor.

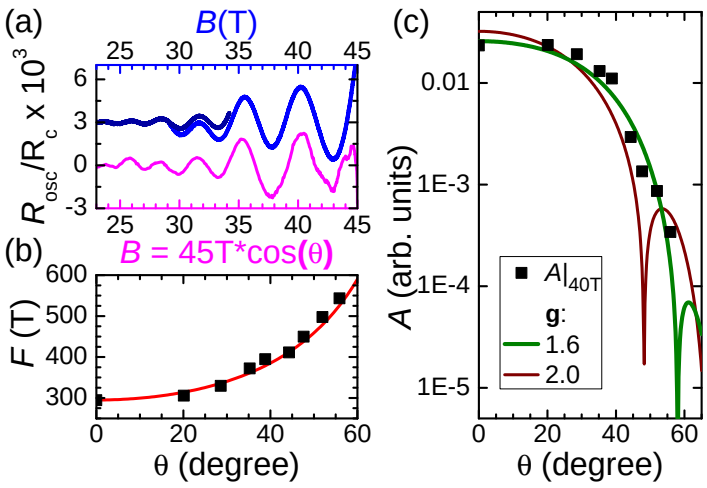

Figure 2: (a) Slow angle-dependent SdH oscillations at 45 T vs. the out-of-plane field component (pink curve). (b) Angle dependence of the SdH oscillation frequency; the red curve is a $1/\cos\theta$ fit. (c) SdH amplitude at 40 T for different polar angles θ; Livshitz-Kosevich fit (green curve); same formula as the fit but $g = 2.0$.

References

[1] M. Lambacher, T. Helm, M. V. Kartsovnik, and A. Erb, Eur. Phys. J. Special Topics **188**, 61–72 (2010).
[2] T. Helm, M. V. Kartsovnik, M. Bartkowiak, N. Bittner, M. Lambacher, A. Erb, J. Wosnitza, and R. Gross, Phys. Rev. Lett. **103**, 157002 (2009).
[3] T. Helm, M. V. Kartsovnik, I. Sheikin, M. Bartkowiak, F. Wolff-Fabris, N. Bittner, W. Biberacher, M. Lambacher, A. Erb, J. Wosnitza, and R. Gross, Phys. Rev. Lett. **105**, 247002 (2010).
[4] M. V. Kartsovnik, T. Helm, C. Putzke, F. Wolff-Fabris, I. Sheikin, S. Lepault, C. Proust, D. Vignolles, N. Bittner, W. Biberacher, A. Erb, J. Wosnitza, and R. Gross, New J. Phys. **13**, 015001 (2011).

Magnetoresistance in the Normal and Superconducting States of α-(BEDT-TTF)$_2$KHg(SCN)$_4$

M. Kunz, W. Biberacher, K. Neumaier, M. V. Kartsovnik [1]
V. N. Zverev[2] *, N. D. Kushch*[3] *, H. Müller*[4]

Unconventional superconductors are often characterized by the existence of competing ordering instabilities. In the high temperature superconductors there is a competition between Mott-insulating antiferromagnetic and superconducting ground states. In the highest-T_c (about 13 K) organic superconductors the superconducting state is also observed in close proximity of an antiferromagnetic ground state. The balance between the two states can easily be tuned by an external parameter like pressure or chemical composition. In our group we have observed superconductivity near a charge-density-wave (CDW) ground state in α-(BEDT-TTF)$_2$KHg(SCN)$_4$ [1, 2]. This compound shows a transition to a CDW state at about 8 K. Under pressure the transition temperature continuously decreases and at the critical pressure $p_c \approx 2.5$ kbar the CDW state is completely suppressed in zero magnetic field and a superconducting state is established. It is of particular interest to study the properties of both the normal metallic and superconducting states in the vicinity of the quantum critical point determined by the critical pressure.

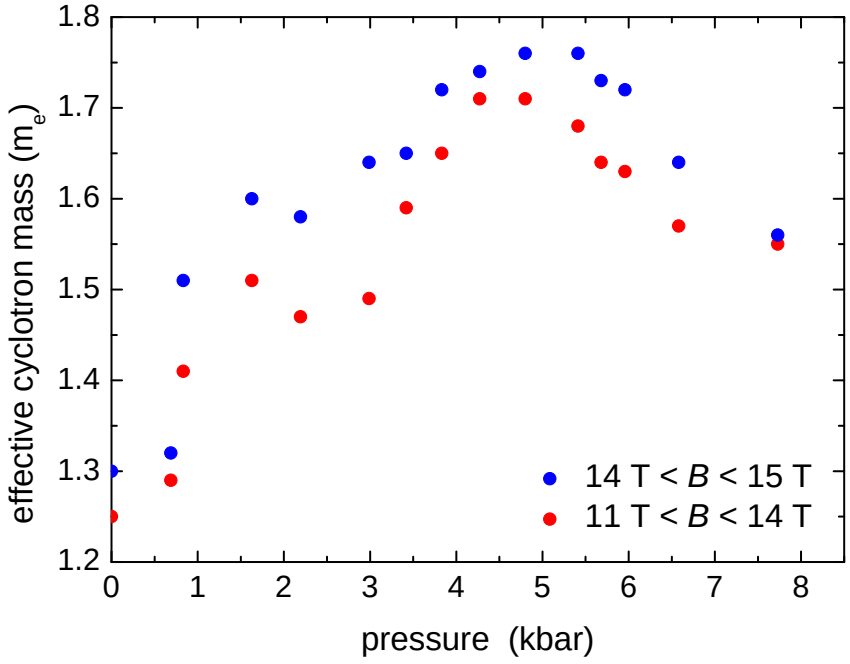

Figure 1: Pressure dependence of the effective cyclotron mass in units of the free electron mass.

To this end, we have investigated the pressure dependence of the effective cyclotron mass as determined from the Shubnikov-de Haas (SdH) effect in the interlayer magnetoresistance. The experiments were carried out in a He-flow cryostat with a superconducting solenoid in magnetic fields up to 15 T, the pressure was applied via a clamp cell technique. For the calculation of the effective mass we applied the Lifshitz-Kosevich theory to the temperature dependence of the SdH oscillation amplitude.

The results are summarized in Fig. 1. The red and black circles present the mass values determined for the field intervals $11 - 14$ T and $14 - 15$ T, respectively. The obtained nonmonotonic

[1] This work was supported by the German Research Foundation by grant numbers 436 RUS 113/926/0 and BI

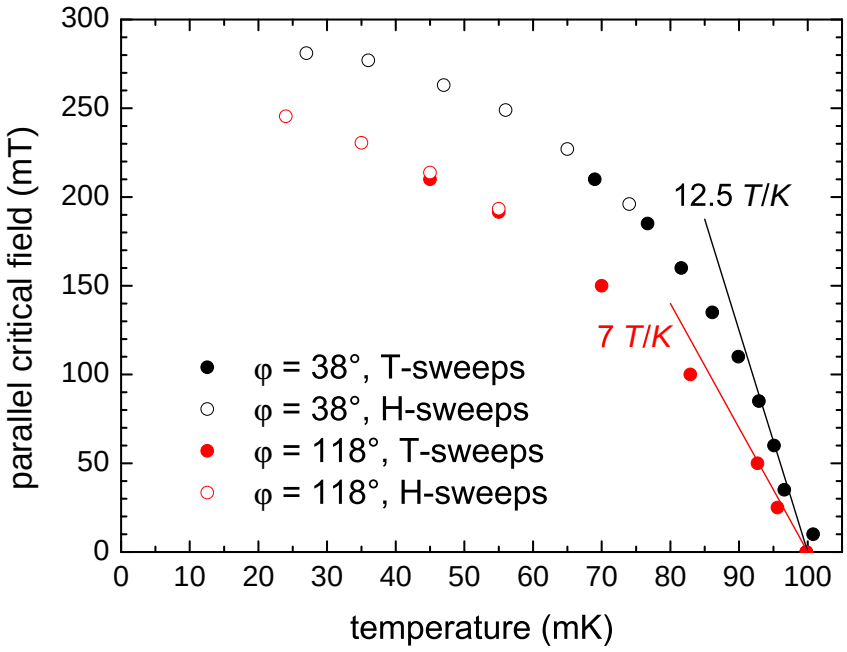

Figure 2: *B-T* phase diagram for fields parallel to the layers at different azimuthal angles.

pressure dependence is anomalous. In ordinary organic superconductors the application of pressure yields a continuous decrease of the effective mass. This is explained by a broadening of the conduction band under pressure and thereby weakening of correlation effects. In the present case one could expect an enhancement of the effective mass in the vicinity of the quantum critical point. However, the data in Fig. 1 shows a peak at a pressure of 5 kbar which is considerably higher than the critical value of 2.5 kbar mentioned above. To understand this, we should take into account that the present data is obtained at a strong magnetic field. As shown in our previous experiments [3, 4] a magnetic field applied perpendicular to conducting layers restores the CDW state at $p > p_c$ due to the orbital quantization effect. However, due to the competing, paramagnetic effect, this field-induced CDW (FICDW) state is eventually suppressed at a high enough pressure. The fact that the effective mass displays a peak at $p = 5$ kbar suggests that this is actually the critical pressure for the FICDW state.

The superconducting state of the present compound is characterized by a very low critical temperature ($T_{c,\max} = 0.11$ K) and, hence, low critical fields. Therefore its behavior should be strongly influenced by the zero-field critical pressure $p_c = 2.5$ kbar. Due to the low T_c, effects of superconducting fluctuations and flux motion are very small and the upper critical field B_{c2} is a well defined quantity which can be determined by e.g. resistive measurements. Detailed resistive studies of B_{c2} at a pressure of 2.8 kbar (i.e. close to p_c) were performed at the WMI by S. Jakob [5]. Here we have studied the B_{c2} behavior at a pressure of 3.4 kbar, i.e. almost 1 kbar away from the zero-field quantum critical point. The experiments were done using the home-made dilution refrigerator with vector magnet [5] which allows us to study the B_{c2} anisotropy by interlayer resistance measurements at temperatures down to 20 mK.

The zero-field critical temperature, $T_c \approx 100$ mK, at 3.4 kbar is about 10% lower than at 2.8 kbar; the critical field perpendicular to the conducting layers is extrapolated to be about

340/3-1

[2]Institute of Solid State Physics, 142432 Chernogolovka, Russia
[3]Institute of Problems of Chemical Physics, 142432 Chernogolovka, Russia
[4]European Synchrotron Radiation Facility, 38043 Grenoble, France

4.5 mT at $T = 0$ K. Both values are in perfect agreement with former measurements by D. Andres et al. [2]. For fields parallel to the layers the critical field $B_{c2,\parallel}$ shows a pronounced dependence on the azimuthal angle φ measured from the a-axis to the field direction. Near T_c the maximum slope $dB_{c2,\parallel}/dT = 12.5$ T/K is obtained for $\varphi = 40°$. For the orientation turned by 90° from this direction the slope is minimal and a factor 1.8 lower. The very high slope, comparable to what is observed on organic superconductors with 100 times larger T_c, indicates that the orbital pair-breaking effect is very weak in the present compound. Therefore, one could expect the Pauli paramagnetic effect to become important at low enough temperatures. Indeed, we observe a strong deviation of $B_{c2,\parallel}(T)$ from the initial slope upon cooling below $0.9\,T_c$ and a clear tendency towards saturation at lower temperatures. The in-plane anisotropy of $B_{c2,\parallel}$ decreases and for $T = 0$ the critical fields extrapolate to almost the same value (see Fig. 2). This is expected for the Pauli paramagnetic effect since the spin effect is isotropic. The saturation value of $B_{c2,\parallel}$ is a factor of 1.5 bigger than the Chandrasekhar-Clogston limit, derived for a weak coupling BCS superconductor. This suggests strong coupling effects to be important in this superconductor.

Comparing our results with the former measurements at $p = 2.8$ kbar [5], we observe for all field orientations that the initial (near T_c) slope $dB_{c2,\parallel}/dT$ decreased by 35% in our experiment. This cannot be explained simply by the 10% decrease of the zero-field critical temperature. Further experiments at higher pressures will hopefully shed light on this point. On the other hand, the orientation and magnitude of the azimuthal anisotropy of the in-plane critical field $B_{c2,\parallel}(\varphi)$ did not change on increasing the pressure. Moreover, the saturation value of $B_{c2,\parallel}(T)$ normalized to T_c is the same, within the experimental error, for both pressure values. This implies that the mechanism of superconducting pairing does not change between 2.8 and 3.4 kbar. Taking into account that the CDW instability is still strong at 3.4 kbar (as evidenced by the FICDW transitions), it is possible that charge fluctuations plays an important role in the pairing. It would be interesting to check how the superconducting properties develop with further increasing pressure beyond the FICDW range of the phase diagram.

References

[1] D. Andres, M.V. Kartsovnik, W. Biberacher, K. Neumaier, and H. Müller, J. Phys. IV France **12**, 87–88 (2002).

[2] D. Andres, M. V. Kartsovnik, W. Biberacher, K. Neumaier, E. Schuberth, and H. Müller, Phys. Rev. B **72**, 174513 (2005).

[3] D. Andres, M. V. Kartsovnik, W. Biberacher, H. Weiss, E. Balthes, H. Müller, and N. Kushch, Phys. Rev. B **64**, 161104 (2001).

[4] D. Andres, M. Kartsovnik, W. Biberacher, K. Neumaier, I. Sheikin, H. Müller, and N. Kushch, Fizika Nizkikh Temperatur **37**, 959–969 (2011).

[5] S. Jakob. *Magnetic field effects in the layered organic superconductor* $\alpha - (BEDT - TTF)_2KHg(SCN)_4$. Diplomarbeit, Technische Universität München (2007).

High Pressure Study of the Charge Density Waves in $ErTe_3$

H.-M. Eiter, R. Roßner, M. Lavagnini, M. Künzl, V. Kunkel, R. Hackl [1]
L. Degiorgi, [2] *J.-H. Chu, J. G. Analytis, I. R. Fisher* [3,4]

The origin of and the interactions leading to electronically ordered phases such as superconductivity or charge density waves (CDW) are among the most tantalizing open questions in solid state physics with the cuprates and the pnictides being in the focus. As a step toward an understanding of these complex compounds, the study simpler model systems with similar electronic order may be enlightening. Rare-earth tri-tellurides ($R\mathrm{Te}_3$) proved to be useful for the investigation of low dimensional interacting electrons and CDW order. By applying pressure, TbTe_3 could even be turned superconducting. [1] In general, phase transitions can be induced by varying external control parameters like temperature, doping or pressure. Using pressure, many properties can be studied in a reversible way on a single sample .

$R\mathrm{Te}_3$ are quasi two dimensional layered systems, consisting of stacked rare-earth-tellurium and tellurium layers which mainly determine the physical properties. For compounds with heavier rare-earth atoms the smaller ion radii lead to a decrease of the lattice parameter. The similarity to applied pressure is referred to as chemical pressure which reduces the transition temperature T_{CDW1} from 416 K for SmTe_3 to 244 K for TmTe_3. The heaviest members of the rare-earth series show a second transition to a bidirectional CDW phase at low temperatures [2]. In the case of $ErTe_3$ the transition temperatures are $T_{\mathrm{CDW1}} = 265\,\mathrm{K}$ and $T_{\mathrm{CDW2}} = 155\,\mathrm{K}$. In the CDW state a gap opens up in the single particle spectrum, and two new collective modes appear, associated with oscillations of amplitude and of phase of the CDW [3]. Raman scattering can detect both the signature of the energy gap and the corresponding amplitude mode (AM) [4]. We use the AM as a probe for the CDW phase transition to map out the high pressure phase diagram of $ErTe_3$. Fig. 1 shows the temperature and pressure dependences of the imaginary part $R\chi''(\omega)$ of the Raman response, obtained by dividing the measured spectra by the thermal Bose factor [5]. The spectra were measured at various applied hydrostatic pressure values in a home made diamond anvil cell loaded with He as a pressure transmission medium. The polarizations of both incoming and scattered photons are set along the crystallographic *a*-direction, parallel to the Te layers as indicated in the inset of Fig. 1 (a). In this configuration excitations from CDW1 can be detected. Panel (a) displays the temperature dependence of the Raman response at 1 GPa. At 150 K the two main features are a phonon at 95 cm^{-1} and a peak below 50 cm^{-1} which can be attributed

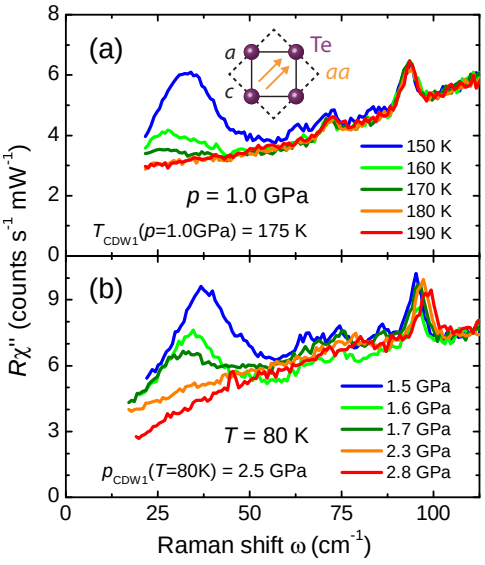

Figure 1: Raman spectra of $ErTe_3$ undergoing a metal-CDW phase transition at constant pressure (a) and temperature (b). The polarizations of incoming and scattered photons (represented by arrows) are both set along the *a*-axis of the tellurium *ac*-plane (dashed lines). The evolution of the amplitude mode (AM) excitation below 50 cm^{-1} is used to identify the phase transition.

[1] This work was supported by the German Research Foundation via HA 2071/5-1.
[2] Laboratorium für Festkörperphysik, ETH-Zürich, CH-8093 Zürich, Switzerland
[3] Stanford Institute for Materials and Energy Sciences, SLAC National Accelerator Laboratory, 2575 Sand Hill Road, Menlo Park, CA 94025, USA
[4] Geballe Laboratory for Advanced Materials & Dept. of Applied Physics, Stanford University, CA 94305, USA

to the AM [4]. With increasing temperature the AM loses spectral weight and moves to lower energy until it disappears between 170 K and 180 K, thus 175 K is identified as $T_{CDW1}(p)$. Above that temperature the sample is in the metallic state where the spectra depend only a weakly on temperature. A second set of measurements is shown in panel (b). Now the pressure is varied at constant temperature, $T = 80$ K. With increasing pressure the phonon at 95 cm^{-1} hardens as expected. Apart from that, increasing pressure has a similar effect as increasing temperature: The AM is more and more suppressed and finally disappears. At $T = 80$ K this is the case at a pressure in the range between 2.3 GPa and 2.8 GPa.

The phase diagram shown in Fig. 2 is the result of additional measurements with isobaric or isothermal conditions. Below 2 GPa $T_{CDW1}(p)$ decreases linearly with increasing pressure p. At higher pressure the phase separation line is expected to bend down for thermodynamical reasons as T_{CDW1} approaches zero [6]. Close to $p = 2.5$ GPa $T_{CDW1}(p)$ approaches zero and a quantum critical point is expected. Hence, $ErTe_3$ is another promising candidate for pressure-induced quantum criticality or superconductivity. The magnetic moment and, consequently, the de Gennes factor are smaller here than in $TbTe_3$, and T_c may be higher. Yet, no indications of superconductivity were found by susceptibility measurements in the pressure cell so far. Whereas the smaller de Gennes factor argues for a higher T_c than in $TbTe_3$ the second CDW transition at 155 K in $ErTe_3$ argues otherwise since superconductivity and CDW order compete for the Fermi surface. On the other hand, CDW fluctuations close to a quantum critical point may support superconductivity. For this reason, it is interesting to explore $ErTe_3$ also in the pressure range in which only CDW2 is suppressed. However, at 0.85 GPa the second CDW is already completely suppressed down to the lowest temperatures. For technical reasons it was not possible to go below 0.85 GPa. Although this question remains open our study reveals the first pressure-temperature phase diagram of $ErTe_3$ and provides evidence for a quantum critical point close to 2.5 GPa. In contrast, the CDW vanishes abruptly in $TbTe_3$ indicating a first order transition to the superconducting phase, that may, for instance, be related to a lattice transformation.

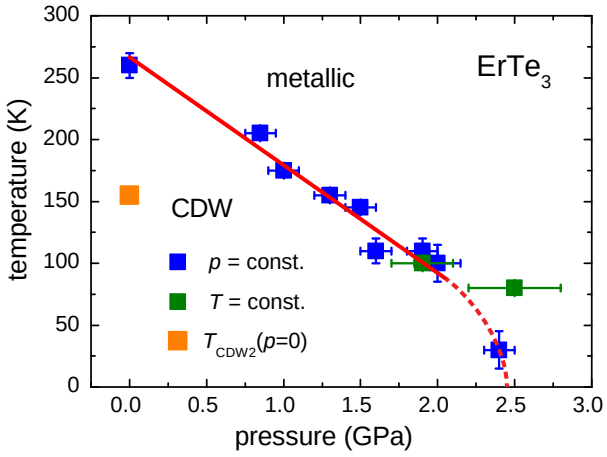

Figure 2: Phase diagram of $ErTe_3$. The experimental metal-CDW phase transition is indicated by blue and green squares for isobaric and isothermal sets of measurements, respectively. Below 2 GPa, T_{CDW1} decreases linearly with pressure (solid red line), while at higher pressure values the phase separation appears to bend down (dashes). Above 2.8 GPa the CDW order is completely suppressed even at 2 K. The orange square marks the transition into the second CDW state.

References

[1] J. J. Hamlin, D. A. Zocco, T. A. Sayles, M. B. Maple, J. H. Chu, and I. R. Fisher, Phys. Rev. Lett. **102**, 177002 (2009).

[2] N. Ru, C. L. Condron, G. Y. Margulis, K. Y. Shin, J. Laverock, S. B. Dugdale, M. F. Toney, and I. R. Fisher, Phys. Rev. B **77**, 035114 (2008).

[3] G. Grüner. *Density Waves in Solids* (Addison-Wesley, 1994).

[4] M. Lavagnini, H.-M. Eiter, L. Tassini, B. Muschler, R. Hackl, R. Monnier, J.-H. Chu, I. R. Fisher, and L. Degiorgi, Phys. Rev. B **81**, 081101 (2010).

[5] T. P. Devereaux, and R. Hackl, Rev. Mod. Phys. **79**, 175–233 (2007).

[6] M. Vojta, Reports on Progress in Physics **66**, 2069 (2003).

Selection Rules in a Strongly Coupled Qubit-Resonator System

T. Niemczyk, F. Deppe, E. P. Menzel, M. J. Schwarz, H. Huebl, F. Hocke, M. Häberlein, E. Hoffmann, A. Baust, A. Marx, R. Gross [1]
E. Solano, [2]*J. J. Garcia-Ripoll* [3]

Superconducting quantum circuits have proven to be versatile model systems for performing quantum optics experiments on a chip, allowing for the investigation of fundamental quantum mechanics and scenarios for scalable quantum information processing. With respect to the former, circuit quantum electrodynamics (QED) [1, 2] has gained exceptional importance in recent years. Here, the coupling of natural atoms to the photon field inside a three-dimensional optical cavity, known as cavity QED, is modeled using superconducting circuits. In particular, suitably designed Josephson junction based quantum circuits act as artificial two-level atoms (qubits) and transmission line resonators serve as "boxes" for microwave photons. Recently, even the new regime of ultrastrong light matter coupling has been reached, [2] where the coupling strength becomes a significant fraction of the total system energy. An important key feature of circuit QED is the design flexibility inherent to circuits on a chip and the ability to tune their properties *in situ* over a wide range of parameters. Recently, an experimental investigation of a two-photon driven flux qubit coupled to a lumped-element *LC* resonator demonstrated the controllability of fundamental symmetry properties of circuit QED systems. [3, 4]. In that work, a high loss rate of the *LC* resonator leading to a weakly coupled qubit-resonator system in combination with the presence of microscopic defects complicated the analysis of the data. Here, we report on one- and two-photon spectroscopy of a qubit-resonator system in the strong coupling limit. Our results provide clear evidence for the controlled transition from an operating point governed by dipolar selection rules to a regime where one- and two-photon excitations of the artificial atom coexist.

In our experiments, two superconducting persistent flux qubit are galvanically [2] connected to the center conductor of a high-Q niobium coplanar waveguide resonator with a fundamental resonance frequency ($\lambda/2$-mode) of $\omega_1/2\pi = 2.745\,\mathrm{GHz}$ (Fig. 1 a). The potential of the three-junction flux qubit can be tuned by an external flux bias Φ_x. At $\delta\Phi_x = \Phi_x - (k - 0.5)\Phi_0 = 0$, the opposite persistent current states $\pm I_p$ are degenerate. Here, $\Phi_0 = h/2e$ denotes the magnetic flux quantum and $k \in \mathbb{Z}$. The two flux qubits are fabricated with slightly different loop areas. For $|k| \geq 2$, the small area difference allows to investigate the individual qubit parameters separately. We monitor the amplified cavity transmission signal at ω_{rf} using a vector network analyzer (VNA). For spectroscopy measurements, the qubit can be excited by an additional microwave tone ω_s.

The transmission spectrum of the $3\lambda/2$-mode in Fig. 1 b reveals avoided crossings at flux positions ($\delta\Phi_x \approx \pm 2\,\mathrm{m}\Phi_0$) where the transition frequency of the qubit ω_q equals the resonator mode frequency ω_3. At these flux values, the system is resonant and energy can be coherently exchanged between qubit and resonator. There are no avoided crossings in the transmission spectrum of the λ-mode for qubit 1. Here, the system is in the dispersive regime for all $\delta\Phi_x$ values and the detuning between the qubit and the cavity modes is large in comparison to the coupling strength. Although qubit and resonator can not exchange energy directly, they are still interacting through a second order dispersive coupling. This leads to an ac-Zeeman shift of the cavity's resonance frequency ω_2 which depends on the qubit state and can be

[1] We acknowledge financial support from the German Research Foundation through SFB 631 and the German Excellence Initiative via NIM.
[2] Universidad del País Vasco and Ikerbasque Foundation, Bilbao, Spain
[3] Instituto de Física Fundamental, Madrid, Spain

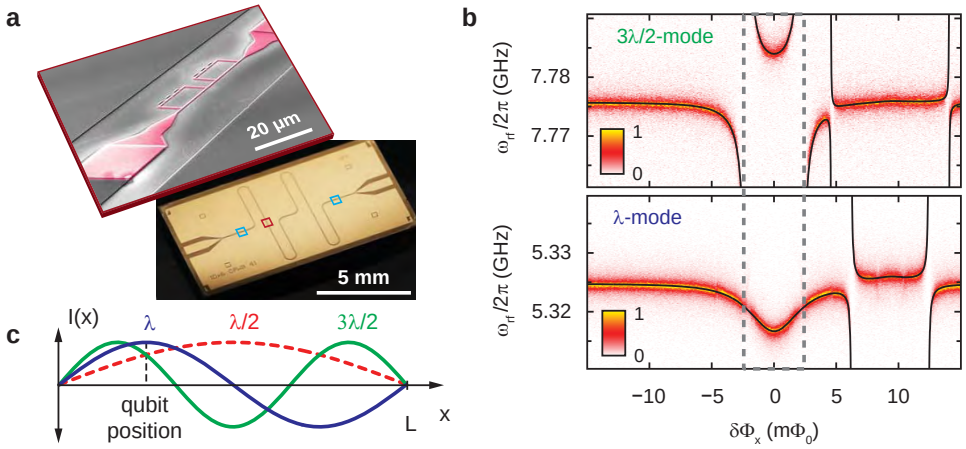

Figure 1: (a) Optical and false-color scanning electron images of the galvanically coupled quantum circuit. The position of the flux qubits (magenta) is indicated by the red box and the light blue boxes mark the position of the coupling capacitors. (b) Sketch of the current distribution $I(x)$ of the first three resonator modes. (c) Cavity transmission spectrum (linear scale, arb. units) for the $3\lambda/2$-mode (top panel) and the λ-mode (bottom panel) as a function of the relative flux bias $\delta\Phi_x$ of qubit 1 and the probe frequency ω_{rf}. The solid lines show the numerically evaluated full energy level spectrum.The broken gray lines mark the $\delta\Phi_x$ range plotted in Fig. 2.

utilized for two-tone spectroscopy measurements. Here, the cavity is monitored at maximum transmission by a probe tone of frequency ω_{rf}. A second microwave spectroscopy tone at the qubit resonance frequency ω_q leads to a dispersive qubit-cavity interaction.

The one-photon spectroscopy data is shown in Fig. 2 a and b and reflects the hyperbolic flux dependence of the qubit transition frequency. A flux-independent signature visible in Fig. 2 a and b can be attributed to a spurious fluctuator present in our system. A flux-dependent spectroscopic signature in the region from $7.4\,\mathrm{GHz} \lesssim \omega_s/2\pi \lesssim 7.6\,\mathrm{GHz}$ is consistent with a two-photon driven blue-sideband transition of the qubit and the $3\lambda/2$-mode. Figure 2 c and d shows the spectroscopic response of the qubit-cavity system under direct two-photon driving where the spectroscopy tone is applied around $2\omega_s = \omega_q$. The spectrum also shows a hyperbolic flux dependence with two anticrossings located symmetrically around $\delta\Phi_x = 0$, and a gradual disappearance of the qubit spectroscopy signal for $\delta\Phi_x \to 0$ which can be understood by considering the symmetry properties of our system which imply selection rules for the allowed transitions.

At $\delta\Phi_x = 0$, the two lowest qubit energy eigenstates $|g\rangle$ and $|e\rangle$ represent symmetric and antisymmetric superpositions of the persistent current states $|\pm I_p\rangle$. Transitions between $|g\rangle$ and $|e\rangle$ are induced by an external drive. It can be shown that the drive is an odd parity operator and as $|g\rangle$ and $|e\rangle$ correspond to states with different parities, one-photon transitions are allowed at the qubit degeneracy point. On the other hand, a two-photon (n-photon) transition is equivalent to the application of two (n) subsequent drives with frequency $\omega_q/2$ (ω_q/n). The two-photon drive is effectively an even parity operator and therefore two-photon transitions between $|g\rangle$ and $|e\rangle$ are forbidden. Away from the qubit degeneracy point ($\delta\Phi_x \neq 0$), the parity of the Hamiltonian is not well-defined. The gradual disappearance of the qubit signature can be qualitatively described using a Schrieffer-Wolff transformation in the dispersive limit to calculate the transition matrix elements [3, 4]. The anticrossings in the spectrum shown in Fig. 2 c and d are a direct manifestation of the one-photon qubit-resonator anticrossing under two-photon driving. The fact that these anticrossings are resolved so clearly indicates that the qubit-cavity system is in the strong coupling limit.

Our results provide clear experimental evidence for the controlled transition from an oper-

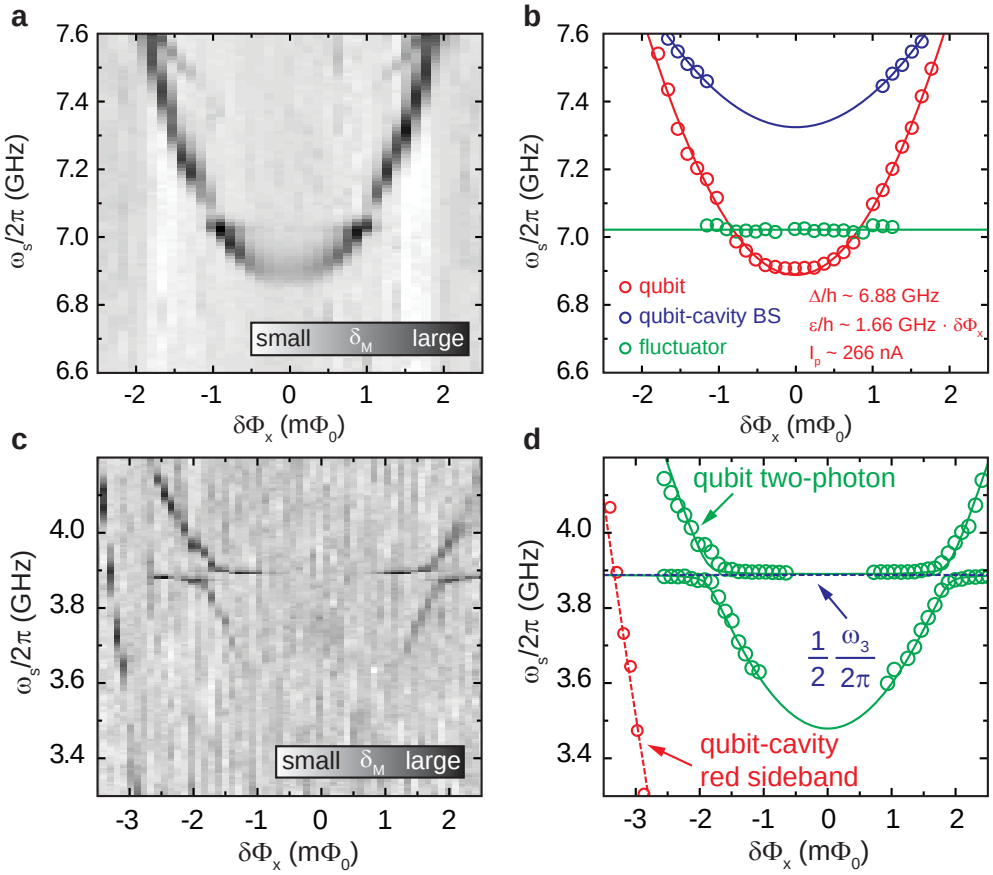

Figure 2: (a) One photon qubit spectroscopy. The relative change in the transmission magnitude δ_M is plotted as a function of $\delta\Phi_x$ and the spectroscopy frequency $\omega_s/2\pi$. (b) The magenta and blue circles indicate the fitted center frequencies of the qubit and a blue sideband spectroscopy signal, respectively. The solid magenta line is a fit to the energy level spectrum of Hamiltonian while the solid blue line is evaluated using the fit parameters derived from the qubit data. The flux-independent feature in the region $\omega_s/2\pi \approx 7\,\mathrm{GHz}$ is attributed to the presence of a spurious fluctuator. (c) Two-photon spectroscopy: relative change in the transmission magnitude. (d) Fitted center frequencies of the spectroscopic qubit response (green circles). The solid green line is the numerically evaluated energy level spectrum of the Hamiltonian with $\omega_q \to \omega_q/2$ and $\omega_n \to \omega_n/2$. Dotted blue line: $1/2 \cdot \omega_3/2\pi$. Dashed red line: calculated flux dependence of the red sideband transition.

ating point ($\delta\Phi_x = 0$) governed by dipolar selection rules to a regime where one- and two-photon excitations of the artificial atom coexist. While the former is strictly analogous to the case of natural atoms, the latter regime is a particular prominent feature of circuit QED. By tuning the external control parameter $\delta\Phi_x$ the symmetry of the system can be broken in a controlled way and two-photon driving of the coupled qubit-cavity system becomes possible.

References

[1] A. Wallraff, D. I. Schuster, A. Blais, L. Frunzio, R.-S. Huang, J. Majer, S. Kumar, S. M. Girvin, and R. J. Schoelkopf, Nature **431**, 162–7 (2004).

[2] T. Niemczyk, F. Deppe, H. Huebl, E. P. Menzel, F. Hocke, M. J. Schwarz, J. J. Garcia-Ripoll, D. Zueco, T. Hümmer, E. Solano, and et al., Nat. Phys. **6**, 772–776 (2010).

[3] F. Deppe, M. Mariantoni, E. P. Menzel, A. Marx, S. Saito, K. Kakuyanagi, H. Tanaka, T. Meno, K. Semba, H. Takayanagi, and et al., Nat. Phys. **4**, 686–691 (2008).

[4] T. Niemczyk. *From strong to ultrastrong coupling in circuit QED architectures.* Ph.D. thesis, TU München (2011).

Squeezing the Vacuum with a Flux-Driven Josephson Parametric Amplifier

E. P. Menzel, F. Deppe, A. Baust, P. Eder, A. Marx, R. Gross [1]
E. Solano, [2] *K. Inomata,* [3] *T. Yamamoto, Y. Nakamura* [4]

A squeezed state, in general, is a state where the uncertainty is decreased in one quadrature of the electromagnetic field and increased in the other such that their product still satisfies Heisenberg's relation [1]. Here, the term "quadrature" denotes a generalized description of amplitude and phase. Recently, squeezed vacuum has been used to reduce the noise of a laser interferometer for the detection of gravitational waves below the shot noise level resulting from vacuum fluctuations [2]. Other possible applications of squeezed states are quantum teleportation and quantum memories. Here, we report on the generation of a quantum microwave state, whose squeezed quadrature has an uncertainty below the vacuum noise level (standard quantum limit) [3, 4]. While it is already interesting on its own to study the quantum effect of squeezing, squeezed microwaves are also compatible with circuit quantum electrodynamics [5, 6] and can be used to generate unconditional distributable entanglement or to read out nano-mechanical resonators with low imprecision [7].

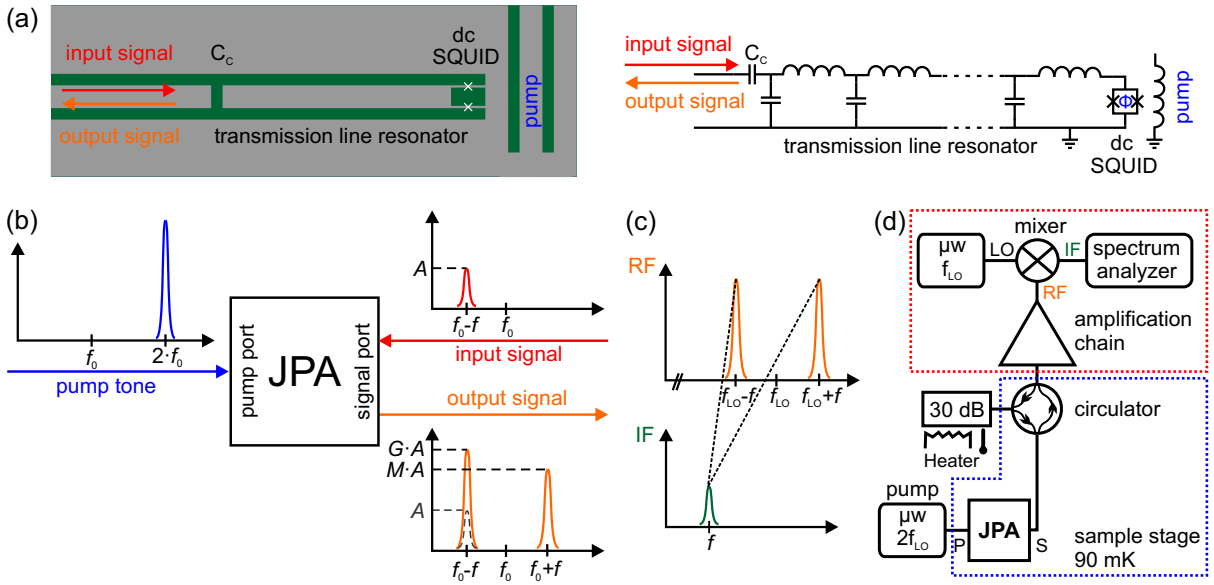

Figure 1: **(a)** Sample layout (left) and circuit diagram (right) of a flux-driven JPA. A magnetic flux Φ applied to the SQUID loop (loop with two crosses denoting Josephson junctions) via the pump line thereby modulates the resonant frequency f_0 of the transmission line resonator. Details of the actual sample can be found in [8]. **(b)** Working principle of a JPA. **(c)** Operation principle of a homodyne detector. In the mixer of the signal and idler mode (RF) are mapped onto the same intermediate frequency (IF), if the local oscillator (LO) frequency is set to half the pump frequency. **(d)** Simplified sketch of the experimental setup. The red rectangle marks the homodyne detector. The two microwave sources (μw) are phase locked.

In order to establish the quantum correlations of the photons in a squeezed state we use a flux-driven Josephson parametric amplifier (JPA) [9], whose sample layout and circuit diagram are displayed in Fig. 1(a). The operating principle of a JPA is analogous to a playground swing,

[1]We gratefully acknowledge financial support from the German Research Foundation through SFB 631, the German Excellence Initiative via NIM, and the EU Marie Curie Initial Training Network CCQED.
[2]Universidad del País Vasco and Ikerbasque Foundation, Bilbao, Spain.
[3]RIKEN, Wako-shi, Japan
[4]NEC Corporation, Green Innovation Research Laboratory, Tsukuba and RIKEN, Wako-shi, Japan

where the deflection amplitude is amplified by modulating the swing length (at twice the oscillation frequency). In the case of the JPA, the oscillating system is a microwave resonator, whose resonant frequency f_0 is determined by its capacitance and inductance. The latter can be varied by a flux-dependent nonlinear inductance provided by a superconducting quantum interference device (SQUID). Applying an ac flux (pump tone) at $2f_0$ modulates the resonant frequency periodically resulting in parametric amplification: A signal at $f_0 - f$ impinging at the signal port is amplified and back reflected, and at the same time an idler mode at $f_0 + f$ is created [see Fig. 1(b)]. If the incoming signal consists of vacuum fluctuations, this process is analogous to spontaneous parametric down conversion, where one pump photon is annihilated and two photons, one in the signal and the other one in the idler mode, are created. This is the origin of the strong quantum correlations between the signal and idler mode. These can be measured with a homodyne detector, where the signal and idler frequencies are mapped onto the same intermediate frequency [see Fig. 1(c)]. Depending on the phase between the local oscillator and the pump, signal and idler mode interfere constructively or destructively. The latter is also referred to as squeezing.

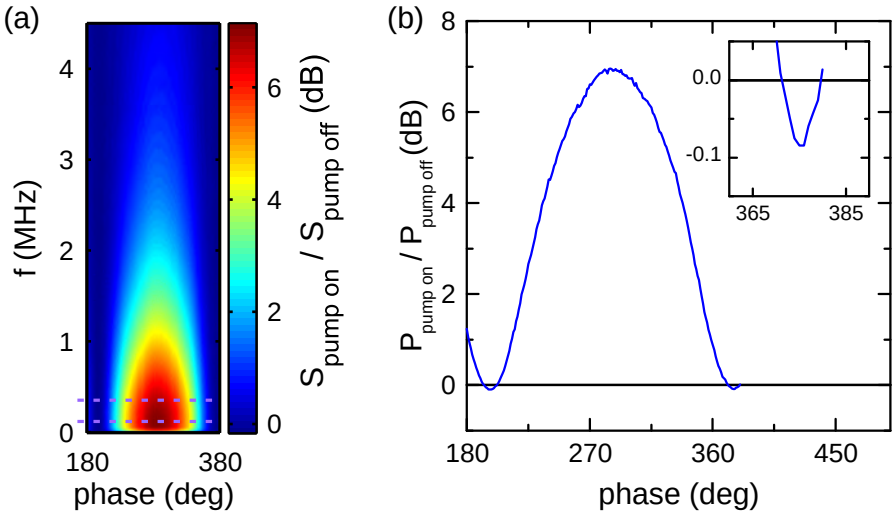

Figure 2: Squeezing of vacuum fluctuations. **(a)** Color map plot of spectra with active JPA divided by spectra with JPA off versus the relative phase between the pump and the homodyne detector. **(b)** Average of the plot in (a) over the frequencies in the range of 118-352 kHz marked by the dashed lines in (a). The inset magnifies the region close to the right minimum.

The experimental setup is shown in Fig. 1(d). When the 30 dB-attenuator is cooled to millikelvin temperatures, a vacuum state is fed via the circulator to the JPA. The circulator separates the outgoing from the incoming signal and isolates the JPA from the noise generated by the amplifiers in the output line. The amplified output signal is measured by a homodyne detector [see Fig. 1(d)]. Figure 2 presents our experimental results. For each phase value, the ratio of two spectra is determined, one measured with the JPA switched on and the other one with inactive JPA. In Fig. 2(b), the average over the frequency range from 118 to 352 kHz is plotted. The minimum has a negative decibel value meaning that the noise detected at the spectrum analyzer is smaller when the JPA is switched on as compared to the case when the JPA is switched off. This demonstrates the effect of noise squeezing. Taking into account the noise temperature of the homodyne detector, which has been measured separately by sweeping the temperature of the attenuator with inactive JPA, we retrieve a lower bound of 4 dB for the squeezing.

The achieved squeezed state is well suited to be reconstructed by our dual-path state reconstruction scheme for propagating quantum microwaves, on which we have reported last

year [10, 11]. Our squeezed state generator is an important element in the toolbox for quantum information processing with propagating microwaves.

References

[1] D. F. Walls, Nature **306**, 141–146 (1983).
[2] The LIGO Scientific Collaboration, Nature Phys. **7**, 962–965 (2011).
[3] R. Movshovich, B. Yurke, P. G. Kaminsky, A. D. Smith, A. H. Silver, R. W. Simon, and M. V. Schneider, Phys. Rev. Lett. **65**, 1419–1422 (1990).
[4] M. A. Castellanos-Beltran, K. D. Irwin, G. C. Hilton, L. R. Vale, and K. W. Lehnert, Nature Phys. **4**, 928–931 (2008).
[5] A. Blais, R.-S. Huang, A. Wallraff, S. M. Girvin, and R. J. Schoelkopf, Phys. Rev. A **69**, 062320 (2004).
[6] A. Wallraff, D. I. Schuster, A. Blais, L. Frunzio, R.-S. Huang, J. Majer, S. Kumar, S. M. Girvin, and R. J. Schoelkopf, Nature **431**, 162–167 (2004).
[7] J. D. Teufel, T. Donner, M. A. Castellanos-Beltran, J. W. Harlow, and K. W. Lehnert, Nature Nanotech. **4**, 820–823 (2009).
[8] A. Baust, E. P. Menzel, T. Niemczyk, E. Hoffmann, M. Häberlein, F. Deppe, A. Marx, R. Gross, K. Inomata, T. Yamamoto, and Y. Nakamura. In **Annual Report 2010** 34–35 (Walther-Meißner-Institut für Tieftemperaturforschung, Garching, 2010).
[9] T. Yamamoto, K. Inomata, M. Watanabe, K. Matsuba, T. Miyazaki, W. D. Oliver, Y. Nakamura, and J. S. Tsai, Appl. Phys. Lett. **93**, 042510 (2008).
[10] E. P. Menzel, F. Deppe, M. Mariantoni, M. Á. Araque Caballero, A. Baust, T. Niemczyk, E. Hoffmann, A. Marx, E. Solano, and R. Gross, Phys. Rev. Lett. **105**, 100401 (2010).
[11] E. P. Menzel, F. Deppe, M. Mariantoni, A. Baust, M. Á. Araque Caballero, E. Hoffmann, T. Niemczyk, C. Probst, K. Neumaier, K. Uhlig, A. Marx, E. Solano, and R. Gross. In **Annual Report 2010** 32–33 (Walther-Meißner-Institut für Tieftemperaturforschung, Garching, 2010).

Scaling Behavior of the Spin Pumping Effect

S. T. B. Goennenwein, F. D. Czeschka, M. Weiler, M. Althammer, J. Lotze, H. Huebl, R. Gross [1]
L. Dreher, M. S. Brandt [2]
I.-M. Imort, G. Reiss, A. Thomas [3,4]
W. Schoch, W. Limmer [5]

The functionality of today's electrical and electronic devices is based on the flow of charge currents $\mathbf{J}_c$. In analogy to a charge current, one can define a *pure spin current* $\mathbf{J}_s$ as the directed flow of spin angular momentum. In spite of the conceptual analogy, however, the properties of pure spin currents are very different from those of charge currents. For example, spin currents can flow in electrical insulators, since no charge motion is required for the propagation of angular momentum. Spin currents thus provide a pathway to exploit the spin degree of freedom in spin-electronic circuits. The spin pumping scheme, which we discuss in the following, is an elegant concept for the generation of pure spin currents.

The spin pumping scheme was proposed theoretically by Tserkovnyak, Brataas, and Bauer [1], and is illustrated in Fig. 1. The spin current generation takes place at the interface between a ferromagnet (F) and a normal metal (N). A microwave magnetic field $\mathbf{H}_1$ in combination with a static magnetic field $\mathbf{H}_0$ excites a resonant precessional motion of the ferromagnet's magnetization $\mathbf{M}$. One pathway for $\mathbf{M}$ to relax back into equilibrium is to transfer angular momentum in the form of a pure spin current $\mathbf{J}_s$ (orange arrow) across the interface into the adjacent N layer. The efficiency of this process is determined by the so-called spin-mixing conductance $g_{\uparrow\downarrow}$. Inside N, the spin current is converted into a conventional charge current $\mathbf{J}_c \propto \mathbf{J}_s \times \mathbf{M}$ (yellow arrows) due to the inverse spin Hall effect [2]. Under open circuit conditions, this results in a DC voltage V_{ISH}. Taken together, in a spin pumping/inverse spin Hall effect experiment, it should thus be possible to quantify the spin current $\mathbf{J}_s$ launched by the resonant magnetization precession by measuring the voltage V_{ISH} across the F/N bilayer with conventional ("charge") electronics.

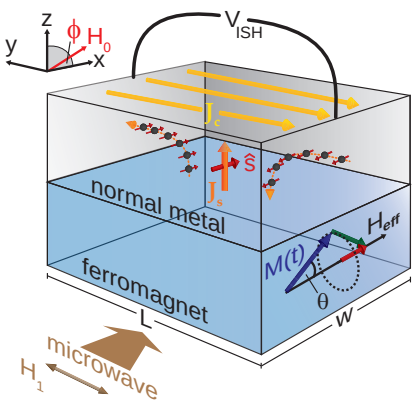

Figure 1: Sketch of the spin pumping process in a ferromagnet/normal metal heterostructure.

We have systematically tested this conjecture in a series of ferromagnet/Pt bilayers, using the 3d transition metals Ni, Co, and Fe, the full Heusler compounds Co_2FeAl and Co_2FeSi, the ferrite spinel Fe_3O_4, and the magnetic semiconductor (Ga,Mn)As as the ferromagnetic constituent, respectively [2]. Figure 2 exemplarily shows spin pumping data recorded at room temperature in a Ni/Pt bilayer. The sample was mounted in the microwave magnetic field antinode of a TE102 cavity in a Bruker magnetic resonance spectrometer operating at $\nu_{MW} = 9.3\,\text{GHz}$. The ferromagnetic resonance (FMR) of the Ni film, evident as a peak-dip structure in Fig. 2(a), is accompanied by a maximum in the DC voltage V_{ISH} across the sample (Fig. 2(b)). As expected, the FMR line does not change when the magnetic field orientation is inverted (Fig. 2(c)). In contrast, the inverse spin Hall voltage $V_{ISH} \propto \mathbf{J}_s \times \mathbf{M}$ should change sign upon $\mathbf{H}$ (and thus $\mathbf{M}$) inversion, as indeed observed in experiment (Fig. 2(d)).

[1] Financial support by the German Research Foundation via the Excellence Cluster *Nanosystems Initiative Munich (NIM)* is gratefully acknowledged.
[2] Walter Schottky Institut, Technische Universität München
[3] Fakultät für Physik, Universität Bielefeld
[4] A. T. and I.-M. I. are supported by the NRW MIWF.
[5] Institut für Quantenmaterie, Universität Ulm

To quantitatively evaluate our experimental data, we use the expression $V_{\mathrm{ISH}} = C\,(\nu_{\mathrm{MW}} P R w)\, g_{\uparrow\downarrow} \sin^2\Theta$ proposed by Mosendz *et al.* [3] for spin pumping in combination with the inverse spin Hall effect. R and w are the bilayer's electrical resistance and its width, respectively, and $0.5 \leq P \leq 1.3$ is a correction factor taking into account the ellipticity of the magnetization precession. The constant $C = e\alpha_{\mathrm{SH}}\lambda_{\mathrm{SD}} \tanh \frac{t_{\mathrm{Pt}}}{2\lambda_{\mathrm{SD}}}$ only contains material parameters of the platinum film and thus is the same for all samples investigated, since we used Pt films with the same thickness $t_{\mathrm{Pt}} = 7\,\mathrm{nm}$ in all cases. e is the electronic charge, α_{SH} the spin Hall angle of Pt, and λ_{SD} the spin diffusion length in Pt.

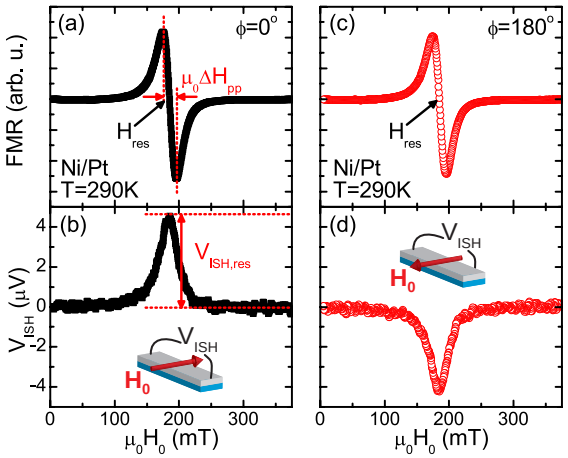

Figure 2: (a), (c) Ferromagnetic resonance signal, and (b), (d) DC voltage recorded at room temperature in a Ni/Pt bilayer, with **H** oriented as indicated in the insets.

We take $V_{\mathrm{ISH,res}}$ at the ferromagnetic resonance and calculate the **M** precession cone angle $\Theta_{\mathrm{res}} = \frac{2H_1}{\sqrt{3}\Delta H_{\mathrm{pp}}}$ from the FMR linewidth ΔH_{pp} observed in experiment and the microwave magnetic field H_1 in the cavity. This leaves the spin mixing conductance $g_{\uparrow\downarrow}$ (assumed to be real here for simplicity) as the only unknown quantity. From the point of view of theory, the magnitude of $g_{\uparrow\downarrow}$ should be essentially independent of the particular conductive ferromagnet used in the F/N bilayer. Thus, one would expect a scaling relation $V_{\mathrm{ISH}}/\,(\nu_{\mathrm{MW}} P R w) = C g_{\uparrow\downarrow} \sin^2\Theta$. This theoretical notion is indeed corroborated by experiment, as is evident from Fig. 3. As detailed in Ref. [2], our data yield $g_{\uparrow\downarrow} = (4 \pm 3) \times 10^{19}\,\mathrm{m}^{-2}$ for highly conductive ferromagnets such as the transition metals and the Heusler compounds, while for low-conductivity ferromagnets such as Fe3O4 or (Ga,Mn)As, $g_{\uparrow\downarrow}$ is about a factor of 6 smaller.

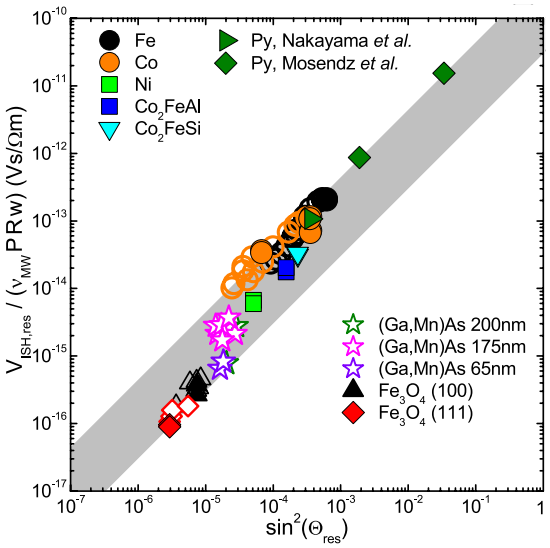

Figure 3: Scaling relation of the spin pumping effect in F/Pt bilayers made from conductive ferromagnets. Full symbols represent data taken at 290 K, open symbols correspond to data measured at lower T. The permalloy (Py) data are taken from Refs. [3, 4]

In summary, our experiments show that the spin pumping process is a robust and reliable source for pure spin currents – in quantitative agreement with the theory. The next step now is a systematic study of spin pumping and pure spin currents in ferromagnetic insulators.

References

[1] Y. Tserkovnyak, A. Brataas, and G. E. W. Bauer, Phys. Rev. Lett. **88**, 117601 (2002).
[2] F. D. Czeschka, L. Dreher, M. S. Brandt, M. Weiler, M. Althammer, I. Imort, G. Reiss, A. Thomas, W. Schoch, W. Limmer, H. Huebl, R. Gross, and S. T. B. Goennenwein, Phys. Rev. Lett. **107**, 046601 (2011).
[3] O. Mosendz, V. Vlaminck, J. E. Pearson, F. Y. Fradin, G. E. W. Bauer, S. D. Bader, and A. Hoffmann, Phys. Rev. B **82**, 214403 (2010).
[4] H. Nakayama, K. Ando, K. Harii, Y. Kajiwara, T. Yoshino, K.-i. Uchida, and E. Saitoh, IEEE Trans. Magn. **46**, 2202 –2204 (2010).

Elastically Driven Ferromagnetic Resonance

M. Weiler, S. T. B. Goennenwein, M. Pernpeintner, C. Heeg, H. Huebl, R. Gross [1]
L. D. Dreher, M. S. Brandt [2]

The magnetic properties of most ferromagnetic materials are affected by elastic deformations. This so-called magneto-elastic coupling enables the "spin-mechanics" magnetization control scheme in ferromagnetic/ferroelectric hybrid structures [1]. In this scheme, the magnetization vector **M** in the ferromagnetic constituent is manipulated via an elastic stress field generated in the ferroelectric constituent by an electric field [2]. For several years, we have been working to transfer the spin-mechanics scheme to the radio frequency (rf) limit, i.e., to GHz frequencies. The main objective hereby is to study the physics of magnon-phonon coupling in single magnetic nanostructures that play an important role in the emerging field of spin caloritronics. The demonstration of purely elastically driven magnetization dynamics represents an important milestone in this direction. We recently could show that the rf elastic strains induced by a surface acoustic wave (SAW) in a ferromagnetic nickel (Ni) thin film allow to excite resonant magnetization dynamics in the latter [3]. Here, we briefly review these elastically driven ferromagnetic resonance (FMR) experiments.

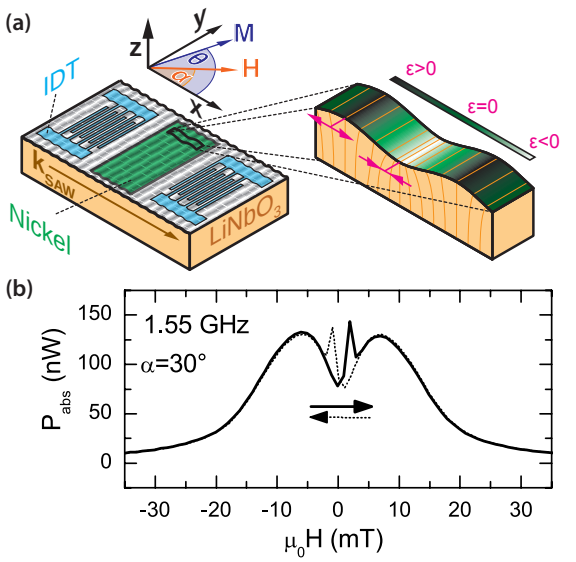

Figure 1: (a) The sample used in the acoustic FMR experiments consists of a ferroelectric $LiNbO_3$ substrate, onto which two interdigital transducers (IDTs) and a nickel thin film were patterned using optical lithography. The propagating SAW induces local tensile ($\epsilon > 0$) or compressive ($\epsilon < 0$) elastic strains. (b) The SAW absorption is strongly magnetic field dependent. The two broad maxima around $|\mu_0 H| \approx 7\,\mathrm{mT}$ are the signature of acoustic FMR, while the sharp, hysteretic features at $|\mu_0 H| \approx 2\,\mathrm{mT}$ are due to **M** reversal. The data were taken at $T = 295\,\mathrm{K}$ with a SAW frequency of 1.55 GHz and with the external, in plane magnetic field at 30° to the SAW propagation direction. The full and dotted line represent H field up- and down-sweep, respectively.

Elastically driven or acoustic FMR is complementary to conventional, microwave photon driven FMR in many aspects. One key difference is the wavelength of the respective excitation: the phonons driving the acoustic FMR propagate at the speed of sound $c_{\mathrm{sound}} \approx 3 \times 10^3\,\mathrm{m/s}$, such that $\lambda_{\mathrm{phonon}} = c_{\mathrm{sound}}/\nu \approx 300\,\mathrm{nm}$ for a typical FMR frequency $\nu = 10\,\mathrm{GHz}$. In contrast, the photons used in conventional FMR measurements propagate with the speed of light, which implies $\lambda_{\mathrm{photon}} \approx 30\,\mathrm{mm} = 10^5 \times \lambda_{\mathrm{phonon}}$. Acoustic FMR thus naturally enables the local excitation and investigation of magnetization dynamics.

For our acoustic FMR experiments, we use the ferromagetic/ferroelectric hybrid sample schematically shown in Fig. 1(a) (see also the Annual Report 2009 [4]). A SAW is generated at the interdigital transducer on the left (IDT1), propagates across the Ni film, and is detected at IDT2. Using vector network analysis with an output power of 0.1 mW, we systematically studied the SAW transmission from IDT1 to IDT2 as a function of the magnitude and the orientation of an externally applied, in-plane magnetic field **H**. As exemplarily shown in Fig. 1(b),

[1] Financial support by the German Research Foundation via the Excellence Cluster *Nanosystems Initiative Munich (NIM)* is gratefully acknowledged.
[2] Walter Schottky Institut, Technische Universität München

the power P_{abs} absorbed from the SAW by the ferromagnetic thin film is strongly magnetic field dependent. In addition to sharp, hysteretic features at the coercive fields $|\mu_0 H_{\mathrm{c}}| \approx 2\,\mathrm{mT}$ of the Ni film, two broad, non-hysteretic absorption peaks appear at higher magnetic fields. These are the signature of acoustically driven FMR, since (i) they depend on the magnitude, but not on the sign of H, (ii) they shift to higher H with increasing SAW frequency ν, and (iii) they characteristically depend on the orientation of $\mathbf{H}$, as shown in the upper row of Fig. 2. In these false color plots, P_{abs} and the dispersed power P_{disp} obtained from SAW transmission measurements are shown as a function of $\mathbf{H}$ orientation α and H.

To model the SAW magneto-transmission, we use the well established Landau-Lifshitz-Gilbert equation $\partial_t \mathbf{m} = -\gamma \mathbf{m} \times \mu_0 \mathbf{H}_{\mathrm{eff}} + a\mathbf{m} \times \partial_t \mathbf{m}$ for the motion of the magnetization unit vector $\mathbf{m} = \mathbf{M}/M$, and introduce the rf elastic drive in the form of a virtual magnetic field $\mu_0 \mathbf{h}_{\mathrm{mag-el}} = -\nabla_{\mathrm{m}} G$, where G is the system's magnetic free enthalpy [3]. Here, γ is the gyromagnetic ratio, $\mathbf{H}_{\mathrm{eff}}$ is the effective magnetic field including shape and magnetic anisotropy contributions, and a is a phenomenological damping coefficient. The power absorbed in resonance is then given by the time average $P = \mu_0 M_{\mathrm{s}} V \langle \mathbf{h}_{\mathrm{mag-el}} \partial_t \mathbf{m} \rangle_t$, with the saturation magnetization M_{s} and the sample volume V. P is complex valued and can be decomposed into the real power absorbed (P_{abs}) and dispersed (P_{disp}). The bottom panels in Figure 2 show the thus simulated P_{abs} and P_{disp}. The simulations accurately reproduce all the salient features of the SAW magneto-absorption observed in the experiment. In particular, the fourfold, rosette-like SAW absorption pattern is clearly evident in both experiment and modeling. It represents the fingerprint of acoustic FMR, since the virtual rf driving field $\mathbf{h}_{\mathrm{mag-el}}$ is finite and appropriately oriented for the excitation of magnetization dynamics only for certain external magnetic field orientations.

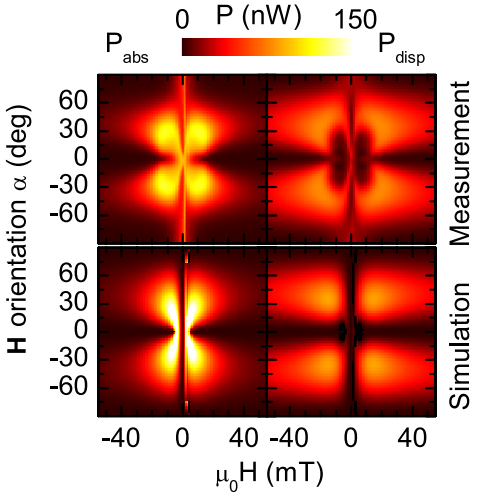

Figure 2: Quantitative comparison of experimentally determined (top row) and simulated (bottom row) absorbed and dispersed power as a function of $\mathbf{H}$ magnitude and in-plane orientation α.

Taken together, we have quantitatively studied surface acoustic wave driven, acoustic FMR in a ferromagnetic/ferroelectric hybrid structure. Our findings show that magnetization dynamics indeed can be driven all-elastically. This opens an avenue for the study of magnon-phonon coupling effects. In particular, the role of spin-phonon coupling for spin-caloritronic effects such as the spin Seebeck effect can be explored.

References

[1] M. Weiler, A. Brandlmaier, S. Geprägs, M. Althammer, M. Opel, S. T. B. Goennenwein, R. Gross, C. Bihler, H. Huebl, and M. S. Brandt. *Annual Report 2008*, 64–67 (Walther-Meißner-Institut für Tieftemperaturforschung, Garching, 2008).

[2] M. Weiler, A. Brandlmaier, S. Geprägs, M. Althammer, M. Opel, C. Bihler, H. Huebl, M. S. Brandt, R. Gross, and S. T. B. Goennenwein, New J. Phys. **11**, 013021 (2009).

[3] M. Weiler, L. Dreher, C. Heeg, H. Huebl, R. Gross, M. S. Brandt, and S. T. B. Goennenwein, Phys. Rev. Lett. **106**, 117601 (2011).

[4] M. Weiler, C. Heeg, H. Söde, A. Brandlmaier, R. Gross, S. T. B. Goennenwein, R. Huber, D. Grundler, J. Manz, and M. S. Brandt. *Annual Report 2009*, 51–53 (Walther-Meißner-Institut für Tieftemperaturforschung, Garching, 2009).

Graphite Oxide Structure and Acidity

A. Lerf
P. Feicht, J. Breu [1]
T. Szabó, I. Dékány [2]

Graphite oxide (GO) has been prepared in 1860 by Brodie [1]. Despite a lot of experimental work GO has received great attention only recently as a precursor of functionalized graphene layers (excellently reviewed by Ruoff et al.) [2, 3]. Considering the wide range of potential applications (as an electrode in lithium cells, e.g. [4], as supercapacitors, as nanocomposites [5] and as a catalyst, e.g. [6]) precise knowledge of the structure of GO is essential. In 1998 Lerf et al. [7] proposed a new structural model based on solid-state nuclear magnetic resonance experiments, assuming the existence of epoxy groups (as proposed by Hofmann et al. [8]) instead of ether functions, hydroxyl groups and unchanged aromatic regions. The carbon layers are therefore slightly bent and warped in regions containing sp^3 orbitals, but flat in the region bonded with sp^2 orbitals. Modifications of this general model take into considerations also isolated and conjugated double bonds. This model is now well confirmed by molecular simulation [9] and chemical modification of the oxygen functions [3].

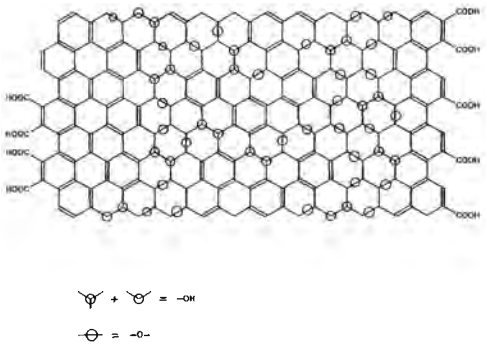

Figure 1: The structural model of graphite oxide as proposed by Lerf et al. [7]

In this structural model the tendency to form stable, negatively charged colloidal suspensions and the high cation exchange capacity cannot be explained easily. If one follows the argumentation of Hofmann, Boehm and coworkers [10–12] the degree of deprotonation depends on the base which is used for titration: 1 acidic group per 8 C atoms should result by applying NaOH as the base and 1 acidic group per 5 C atoms in the case of sodium ethanolate ($NaOC_2H_5$). The resulting acidity is so large that the negative charge resulting from full deprotonation of the OH functions is in the order of that of low charged montmorillonites [12].

However, the carboxyl groups at the periphery of the graphene sheets which are considered to be present in all published structural models are not enough to explain the high acidity [13]. These authors discussed additional carboxyl groups located at the border of internal wholes in partially broken graphene sheets. Even this is not enough. Although these CO_2^--groups have been detected in most recent ^{13}C MAS-NMR spectra, their concentration is very low (<5%).

Clauss et al. brought into discussion the presence of more acidic groups like enols or phenols with pK_a values of 8 - 10 [12]. However, enols are very unstable and transform easily into ketons or aldehyds. For this functional unit a new signal at about 90 - 100 ppm should appear in the ^{13}C NMR spectra. Most recent ^{13}C NMR spectra with higher resolution show a signal at 102 ppm but also an additional one at 190 ppm, both of very low intensity [14]. A combination of signals 110 ppm/190 ppm could be indicative for keto-enol tautomerism as observed in acetylacetone or dimedone. It cannot be ruled out that such sort of arrangements exist at the external border of the graphene sheets. To explain the high acidity of GO these groups

[1]Institut für Anorganische Chemie I, Universität Bayreuth, Universitätsstraße 31, Bayreuth, Germany.
[2]Department of Physical Chemistry and Materials Sciences, University of Szeged, Szeged, Hungary.

should be spread over the whole graphene sheets. However, this would be accompanied with a partial destruction of the carbon grid [12].

Phenols (characterized by ^{13}C chemical shifts at 150 ppm and 110 ppm) cannot be detected in as-prepared GO, but can indeed be formed to a considerable extent under special experimental conditions (heat treatment in vacuum, reaction with iodide) [7]. As in the case of the keto-enol system the formation of phenols on the graphene sheets is unambiguously connected with a breaking of C-C bonds. According to our own experiments we have no evidence that just base treatment at room temperature produces the quantity of these peculiar OH functions required to explain the high acidity of GO (see Jahresbericht 2009), and, if so, we would expect an irreversible increase of the acidity which has never been observed [15].

To cope with this contradiction there are two possibilities:

The pH of about 3 measured in an aqueous suspension of native GO is mainly due to the carboxyl functions at the circumference of graphene sheets. The negative charge produced by deprotonation and the uptake of water in the hydrophilic interlayer space are responsible for the formation of a colloidal dispersion. The higher acidities at the application of stronger bases are pretended by the simultaneous uptake of the base and the corresponding cation (effect of intersalation). To prove this suggestion GO has been treated with sodium acetate and characterized by ^{13}C NMR spectroscopy without washing the sample. However, there is no evidence for the uptake of the acetate ion into GO. On the contrary, after treatment of GO with sodium ethanolate we found the typical chemical shifts of the ethyl group even after washing the sample with dry alcohol [16]. This has been considered as evidence for the covalent attachment of ethanolate to the carbon grid. Surprisingly, the NMR peaks assigned to alcohol and epoxide functions are not changed significantly in intensity. Therefore, it seems to be probable that sodium enolate is intersalated in the interlayer space and not bound covalently to the carbon grid.

The second alternative is to rethink the distribution and possible correlations of the functional groups with respect to the possibility of enhancing the acidity by co-operative interactions. An extreme modification of our previous structural model shows a grid of carbon hexagons carrying one epoxide function, one isolated double bond and two OH functions in a completely regular distribution [17]. A more random distribution of the functional groups is shown in Fig. 1) [3, 18]. In these new arrangements one can recognize coupled functionalities, for example allylic alcohols or vicinal diols with the OH in cis positions. This is not in conflict with the ^{13}C NMR data: so it is not possible in solid state NMR to distinguish aromatic from isolated C=C double bonds; in addition the chemical shift of the allylic OH (1-en-3-ol) is also around 60 ppm as for epoxides; the chemical shifts of the alcohol functions with 70 ppm is found more frequently for carbons in adjacent vicinal diols than for carbons carrying OH groups in molecular tertiary alcohols.

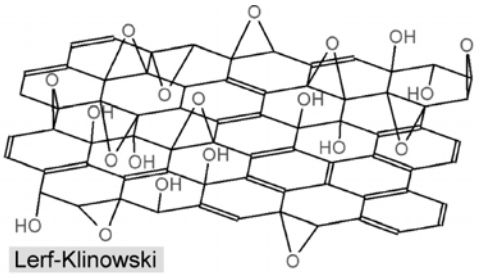

Figure 2: The modified structural model of graphite oxide. Figure taken from [18]

This reinterpretation of the GO structure is supported particularly, at least for the suggested allylic alcohol arrangements. In a previous paper we showed the NMR spectrum of GO treated with acetic acid anhydride, a specific reagent for alcoholic functions [16]. We could detect the CH_3 groups and the carboxyl functions of acids or esters, but only a tiny reduction of the signal assigned previously to epoxide functions (60 ppm) as opposed to our expectation

(reduction of the signal intensity of the 70 ppm peak). If we take into consideration that the signal at 60 ppm is a superposition of epoxide and allylic alcohol functions the result is in perfect agreement with the assumption that only the allylic OH functions have reacted with the acetic acid anhydride and the epoxide portion is left. In a most recent paper an additional example is given for a very specific functionalization of allylic alcohol groups in GO [19].

Fortunately, allylic alcohol has a pK_a value of 15.5 in water. This value is three to four orders of magnitude lower than for tertiary butanol. Calculated pK_a values of cyclohexane species carrying varying numbers of double bonds, epoxide and adjacent OH functions are even lower. That is the right tendency towards higher acidities, i.e. lower pK_a values, but these values are still too high. To explain the titration curves one would expect pK_a values between 7 and 10. All these considerations about acidity are based on the assumption that the acidity of GO-OH functions is comparable with the acidity of alcohols in molecular species. However, nobody knows whether these calculated values from low molecular species have any meaning for a solid. Since there are no hydrogen atoms at the carbons of the C-grid the acidity may be even lower in the solid. In addition there could be also some sort of mesomeric stabilization by the close contact of aromatic and isolated alkene bonds, vicinal OH functions and hydrogen bond interactions.

References

[1] B. Brodie, Ann. Chim. Phys. **59**, 466–472 (1860).
[2] S. Park, and R. S. Ruoff, Nature Nanotechn. **4**, 217–224 (2009).
[3] D. D. Dreyer, S. Park, C. W. Bielawski, and R. S. Ruoff, Chem. Soc. Rev. **39**, 228–240 (2010).
[4] T. Cassagneau, and J. H. Fendler, Adv. Mater. **10**, 877–881 (1998).
[5] T. Kuilla, S. Bhadra, D. Yao, N. H. Kim, S. Bose, and J. H. Lee, Prog. Polym. Sci. **35**, 1350–1375 (2010).
[6] J. Pyun, Angew. Chem. **123**, 46–48 (2011).
[7] A. Lerf, H. He, M. Forster, and J. Klinowski, J. Phys. Chem. **102**, 4477–4482 (1998).
[8] U. Hofmann, A. Frenzel, and E. Csalan, Lieb. Ann. Chem. **510**, 1–41 (1934).
[9] J. Paci, T. Belytschko, and G. E. Schatz, J. Phys. Chem. C **111**, 18099–18111 (2007).
[10] U. Hofmann, and R. Holst, Ber. Dtsch. Chem. Ges. **72**, 754–771 (1939).
[11] W. Scholz, and H. P. Boehm, Z. Anorg. Allg. Chem. **369**, 327–340 (1969).
[12] A. Clauss, R. Plass, H. P. Boehm, and U. Hofmann, Z. Anorg. Allg. Chem. **291**, 205–220 (1957).
[13] U. Hofmann, and E. Koenig, Z. Anorg. Allg. Chem. **234**, 311–336 (1937).
[14] W. Gao, L. B. Alemany, L. Ci, and P. M. Ajayan, Nature Chem. **1**, 403–408 (2009).
[15] T. Szabó, E. Tombácz, E. Illés, and I. Dékány, Carbon **44**, 537–545 (1996).
[16] H. He, T. Riedl, A. Lerf, and J. Klinowski, J. Phys. Chem. **100**, 19954–19958 (1996).
[17] A. Buchsteiner, A. Lerf, and J. Pieper, J. Phys. Chem. B **110**, 22328–22338 (2006).
[18] T. Szabó, O. Berkesi, P. Forgó, K. Josepovits, Y. Sanakis, D. Petridis, and I. Dékány, Chem. Mater. **18**, 2740–2749 (2006).
[19] W. R. Collins, W. Lewandowski, E. Schmois, J. Walish, and T. M. Swager, Angew. Chem. **123**, 9010–9014 (2011).

Application–Oriented Research

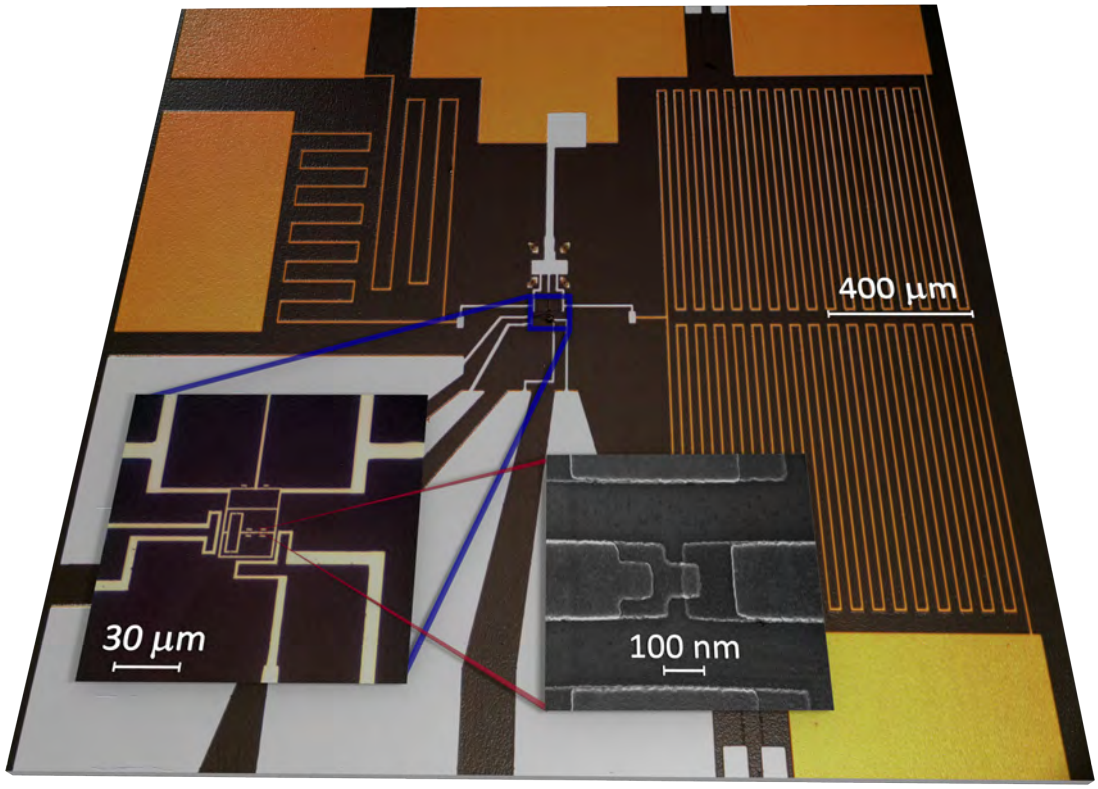

Gradiometric superconducting flux quantum bit embedded into a complex electromagnetic environment.

Gradiometric Flux Quantum Bits with Tunable Tunnel Coupling

M. J. Schwarz, J. Goetz, T. Niemczyk, F. Deppe, A. Marx, R. Gross [1]

Superconducting quantum bits (qubits) based on Josephson junctions are promising candidates for the implementation of quantum information processing architectures [1]. The well-known scalability and the tunability inherent to solid-state circuits provide significant advantages over qubits realized in other physical systems. Moreover, coupling these artificial atoms to microwave resonators has paved the way for the prospering field of circuit quantum electrodynamics (circuit QED), where the study of very strong light-matter-interaction on a macroscopic scale has revealed fascinating new physics [2]. Depending on the degree of freedom that is used to encode quantum information, different types of superconducting qubits can be distinguished. At the WMI, we focus on flux qubits, where quantum information is encoded in the magnetic flux generated by a circulating current in a superconducting loop containing three or more Josephson junctions. In particular, we have studied a gradiometric design with a tunable tunnel coupling. This qubit layout provides for an in situ controllable energy gap without detuning the qubit from the point of optimal coherence.

The original design of a flux qubit consists of a superconducting loop interrupted by three nm-sized Josephson junctions (JJs) [3, 4]. While two of these JJs have the same area $A \approx 0.02\,\mu m^2$ and, hence, the same critical current I_c, the third JJ is smaller by a factor $\alpha \approx 0.6 - 0.8$, thus allowing for the formation of a quantum two-level system. A tunnel coupling Δ between two states corresponding to clockwise and counterclockwise circulating currents in the superconducting ring structure at a flux bias of half a flux quantum leads to a symmetric and antisymmetric superposition of the two states. The qubit can be excited from the ground to the excited state by applying microwave radiation. The qubit state can be detected using a dc-SQUID via the flux signals generated by the clock- and counterclockwise circulating currents in the qubit loop [5].

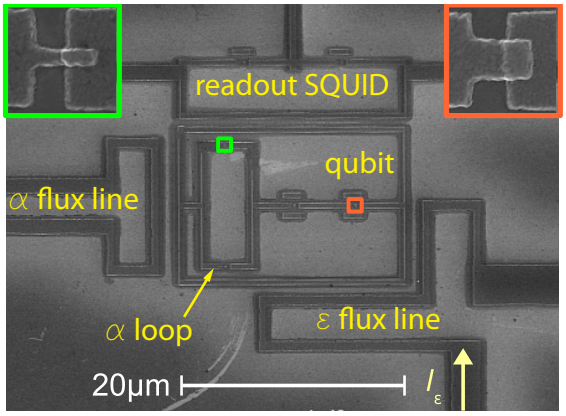

Figure 1: Scanning electron micrograph of the sample layout with readout SQUID, qubit and on-chip flux bias lines. The qubit is implemented in a gradiometric design and one JJ is replaced by a dc-SQUID (α-loop). The insets show enlarged views of the JJs.

Numerous circuit QED experiments require a controllable coupling of superconducting qubits to microwave resonators e.g. to switch on and off the coupling between qubit and resonator. To this end, the development of a flux qubit design allowing for a tunability of the transition frequency is highly required. Since the qubit transition frequency E_{eg}/h can be approximated by [3]

$$E_{eg} = \sqrt{\varepsilon^2 + \Delta^2}, \tag{1}$$

it can be changed by either varying the magnetic energy bias ε or by varying the minimal transition frequency Δ/h, the so called qubit gap. The first way is easy to achieve for a 3-JJ qubit

[1] We gratefully acknowledge financial support by the German Research Foundation through SFB 631, the German Excellence Initiative through NIM, and the EU Marie Curie Initial Training Network CCQED.

by changing the magnetic flux bias via an external solenoid. On the other hand, varying the qubit gap Δ while staying at the anti-crossing point with minimal transition frequency, implies a major advantage: Since the energy of the qubit is stationary with respect to variations of the magnetic flux at this point, minimal flux noise and therefore maximal phase coherence of the qubit is obtained [5]. Δ strongly depends on the factor α, which is fixed during fabrication for a regular 3-JJ qubit. However, a recently proposed new flux qubit design [6] allows to vary α and thus Δ in situ by replacing the smaller α-junction with a dc-SQUID loop, consisting of two junctions with suitably designed critical current (cf. Fig. 1). The critical current of the α-loop then depends on the magnetic flux applied to this loop and can be varied via an additional flux bias line or via an external solenoid. In order not to change the flux bias of the qubit with this externally applied flux, a gradiometric design of the qubit is used, rendering the qubit insensitive to any homogeneous magnetic field that is applied symmetrically to both loops of the eight-shaped gradiometric qubit. Consequently, an inhomogeneous magnetic field is required to adjust the flux bias of the qubit which is generated via the ε flux line. Furthermore, the outer ring of the gradiometric qubit is used as a trap loop for magnetic flux quanta, enabling a magnetic pre-biasing of the qubit avoiding too large currents in the on-chip bias line which would result in intolerable heating of the sample.

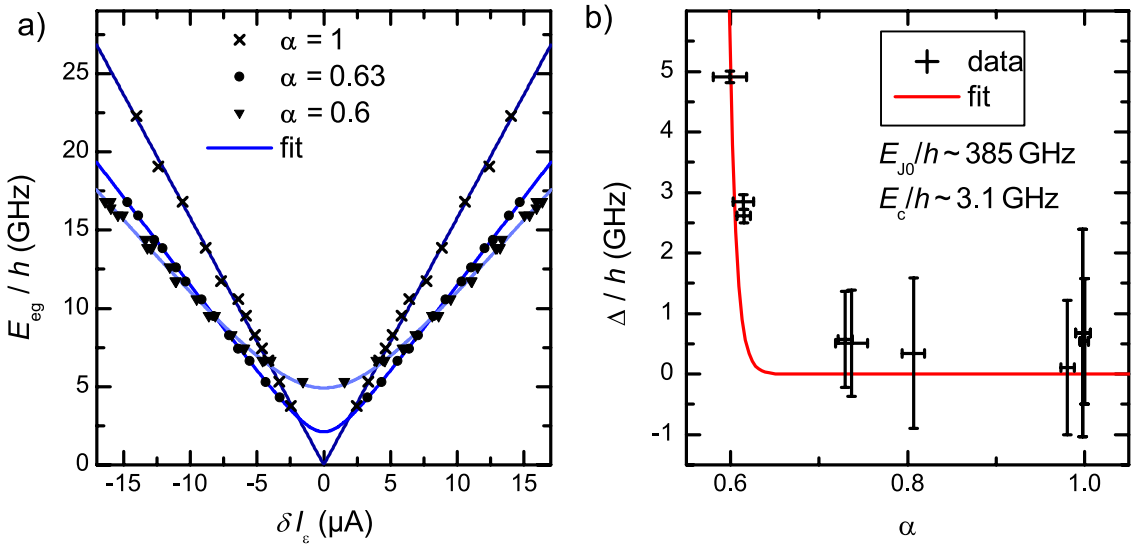

Figure 2: a) Transition frequency of the qubit for three exemplary α-values (adjusted using the solenoid) as a function of magnetic flux generated by a current through the ε line. Blue curves correspond to two-parameter fits. The change of the minimal transition frequency Δ/h can be clearly observed as a change of each curve's minimum; **b)** Minimal transition frequency Δ/h plotted as a function of the α-value. A fit for Δ (red curve) is in good agreement with the data and yields reasonable values $E_{J0}/h = 383\,\text{GHz}$ and $E_c/h = 3.1\,\text{GHz}$. This fit shows in a formidable way that the tunnel coupling of a gradiometric qubit can be tuned in a reliable and controllable way.

Using our well-established fabrication processes [4] we have fabricated tunable flux qubits in a gradiometric design together with readout SQUIDs. Fig. 2a) shows the flux dependent transition frequency for different effective values of α extracted from qubit spectroscopy via the readout SQUID at a temperature of about 30 mK. The blue lines are two-component fits to the measured data (symbols) using Eq. (1). A change of the qubit hyperbolae corresponding to different values of α is clearly observable. The qubit gap Δ obtained from the fits is plotted in Fig. 2b) as a function of the effective value of α. These data are consistent with a fit (red curve) based on an analytical expression for Δ [7] with the fitting parameters charging energy E_c and Josephson coupling energy E_{J0} resulting in reasonable values. These results show that the qubit gap Δ/h can be tuned in a reliable and controllable way from zero to a value of at least 5 GHz. Besides tuning the qubit gap by a solenoid we have also used the on-chip flux

bias line to change the effective value of α, where we have obtained a tunability of Δ/h in the range of $0.5 \ldots 4.5\,\mathrm{GHz}$ with a suitable constant bias set by the solenoid. The maximally obtainable energy gap of the tunable qubit design is expected to increase by slightly changing the fabrication processes which is desirable to match the modes of the microwave resonators from 5 GHz up to 8 GHz typically used in our circuit QED experiments. Nevertheless, the range of tunability is sufficient to couple and decouple the qubit to a microwave resonator.

In conclusion, we have fabricated a gradiometric flux qubit with a tunnel coupling tunable in situ. We have demonstrated a large tunability of the qubit gap both with an external solenoid and an on-chip bias line. An implementation of this qubit into circuit QED experiments with a qubit coupled to a microwave resonator will now be pursued.

References

[1] J. Clarke, and F. K. Wilhelm, Nature **453**, 1031 (2008).

[2] T. Niemczyk, F. Deppe, H. Huebl, E. P. Menzel, F. Hocke, M. J. Schwarz, J. J. Garcia-Ripoll, D. Zueco, T. Hummer, E. Solano, A. Marx, and R. Gross, Nature Phys. **6**, 772 (2010).

[3] T. P. Orlando, J. E. Mooij, L. Tian, C. H. van der Wal, L. S. Levitov, S. Lloyd, and J. J. Mazo, Phys. Rev. B **60**, 15398 (1999).

[4] T. Niemczyk, F. Deppe, M. Mariantoni, E. P. Menzel, E. Hoffmann, G. Wild, L. Eggenstein, A. Marx, and R. Gross, Supercond. Sci. Technol. **22**, 034009 (2009).

[5] F. Deppe, M. Mariantoni, E. P. Menzel, S. Saito, K. Kakuyanagi, H. Tanaka, T. Meno, K. Semba, H. Takayanagi, and R. Gross, Phys. Rev. B **76**, 214503 (2007).

[6] F. G. Paauw, A. Fedorov, C. J. P. M. Harmans, and J. E. Mooij, Phys. Rev. Lett. **102**, 090501 (2009).

[7] J. Goetz. *Gradiometric flux quantum bits with tunable tunnel coupling*. Diploma thesis, TU München (2011).

Compact Superconducting Coplanar Beam Splitters

N. Kalb, M. Haeberlein, F. Deppe, A. Marx, R. Gross [1]

In circuit quantum electrodynamics (QED), superconducting circuits acting as artificial two-level atoms exhibit an interaction of unprecedented strengths [1, 2] with circuits playing the role of cavities for microwave light. In this way, studies on fundamental light matter coupling as well as quantum information processing schemes can be performed in analogy to quantum optical cavity QED. In a similar analogy to quantum optics, microwave beam splitters are attractive devices when dealing with concepts based on quantum microwaves propagating in open transmission lines. Examples for such concepts are the dual-path state reconstruction scheme [3] and quantum computing in the spirit of all-optical quantum information processing [4]. Among the various types of superconducting transmission lines, coplanar structures are particularly popular because they exhibit high field densities and low dielectric losses [5]. However, standard microwave beam splitters such as the 180° hybrid ring [6] have a rather large diameter of 9.56 mm at a center frequency of 5.6 GHz, a property clearly hindering scalability. Therefore, in this work we fabricate and characterize a superconducting hybrid ring with coplanar feed lines and minimized dimensions.

Our beam splitters are patterned into a 100 nm thick niobium film on a SiO_2 (50 nm) covered 250 µm thick silicon substrate. Fig. 1 shows the design of the compact 180° hybrid ring discussed in this work. The four feed lines are 50 Ω matched coplanar waveguides with finite groundplanes, whereas the circumference waveguide is a so-called coplanar microstrip. The interference of the incident microwave with itself determines the centre frequency $f_0 = 7.4$ GHz. An input signal at port one is evenly split into a clockwise and a counterclockwise propagating wave. These two waves interfere constructively at ports two and four (coupling) or destructively at ports one and three (isolation) with each other. The compactness of our beam splitter is guaranteed by two design features. First, a crossover between port two and port three causes a local phase jump of 180° and makes the use of a space consuming delay line unnecessary. Second, the specific choice of the characteristic impedance of the coplanar microstrip results in a reduced length $\lambda_0/6$ of the four ring segments (this length is $\lambda_0/4$ in standard designs [6]). Here, λ_0 is the wave length corresponding to f_0.

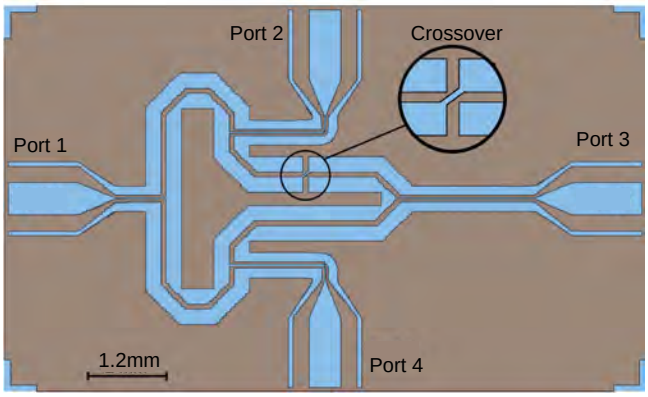

Figure 1: Sketch of the compact 180° hybrid ring used in our experiments. Blue areas: niobium. Grey area: substrate.

The device is mounted into a gold-coated copper box and cooled down to a temperature of 4.2 K. A two-port vector network analyzer is connected to ports i and j while terminating the remaining two ports with 50 Ω loads. We measure the scattering parameters S_{ij} $(i, j = 1 \ldots 4)$, which describe the ratio of the amplitude of the wave incident at port j to that of the wave leaking out of port i. The results of our measurements in the frequency band of 5.8-9.9 GHz

[1] We acknowledge financial support by the SFB 631 of the German Research Foundation, the German Excellence Initiave via NIM, and the EU Marie Curie Initial Training Network CCQED.

are shown in Fig. 2. We observe a good isolation of 36.9 dB at f_0 and more than 25 dB within a bandwidth of 0.5 GHz around f_0. In the same frequency window, the coupling of 3.5 ± 0.3 dB is close to the value of 3 dB expected for an ideal lossless beam splitter. Taking into account a rescaling to a center frequency of approximately 6 GHz, which is compatible with other experiments at the WMI, the compact hybrid ring occupies only an area of 16 mm^2.

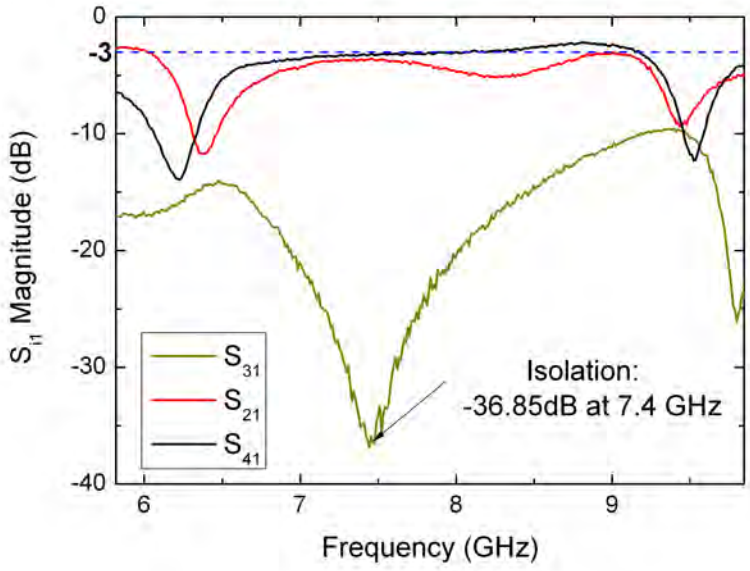

Figure 2: Scattering parameters S_{ij} of the compact 180° hybrid ring.Blue dashed line: the coupling value for an ideal lossless beam splitter.

In summary, we have successfully fabricated and charactzerized a coplanar superconducting beam splitter, which occupies only 23% of the area of a standard 180° hybrid ring [6]. Our device is a promising candidate as element for photon based quantum computing with superconducting circuits or state reconstruction of propagating quantum microwaves.

References

[1] A. Wallraff, D. I. Schuster, A. Blais, L. Frunzio, R.-S. Huang, J. Majer, S. Kumar, S. M. Girvin, and R. J. Schoelkopf, Nature **431**, 162–167 (2004).
[2] T. Niemczyk, F. Deppe, H. Huebl, E. P. Menzel, F. Hocke, M. J. Schwarz, J. J. Garcia-Ripoll, D. Zueco, T. Hümmer, E. Solano, A. Marx, and R. Gross, Nature Physics **6**, 772–776 (2010).
[3] E. P. Menzel, F. Deppe, M. Mariantoni, M. A. Caballero, A. Baust, T. Niemczyk, E. Hoffmann, A. Marx, E. Solano, and R. Gross, Phys. Rev. Lett. **105**, 100401 (2010).
[4] J. L. O'Brien, Science **318**, 1567–1570 (2007).
[5] M. Göppl, A. Fragner, M. Baur, R. Bianchetti, S. Filipp, J. M. Fink, P. J. Leek, G. Puebla, L. Steffen, and A. Wallraff, J. Appl. Phys. **104**, 8 (2008).
[6] E. Hoffmann, F. Deppe, T. Niemczyk, T. Wirth, E. P. Menzel, G. Wild, H. Huebl, M. Mariantoni, T. Weißl, and A. Lukashenko, Appl. Phys. Lett. **97**, 222508 (2010).

Distributed Coupling of Superconducting Transmission Line Resonators

M. Haeberlein, F. Deppe, L. Augsbach, U. Ehmann, N. Kalb, A. Marx, R. Gross [1]
D. Zueco [2], *T. Weissl* [3], *J. J. Garcia-Ripoll* [4], *E. Solano* [5]

In the last decade, the fundamentals of light-matter coupling were investigated in several physical systems including atoms, trapped ions, quantum dots, and superconducting quantum circuits [1, 2]. With respect to the latter, microwave light is stored in linear *LC*-resonators and matter is represented by Josephson junction based circuits acting as artificial two-level atoms (also called quantum bits or qubits). Prominent experiments at the WMI [3] and elsewhere [4] showed that the rate at which a single qubit is coupled to a microwave mode can be increased significantly beyond the regime found for natural atoms. In addition to such interesting and novel physics, another motivation for engineering high coupling rates resides in the potential of building a superconducting quantum processor from qubits and resonators [5]. For such a task, one wants to fit as many gate operations as possible into the coherence times of the involved quantum circuits. The resulting requirements on coherence times can, to some extent, be relaxed by engineering larger coupling strengths. In this situation, we may need to consider not only the qubit-resonator [4] coupling, but also the resonator-resonator interaction strength.

In this work, we study distributed coupling between two superconducting microstrip transmission line resonators. Our microstrip resonators consist of a thin superconducting niobium strip on top of a SiO_2 (50 nm) covered 250 µm thick silicon wafer with a superconducting groundplane on its bottom. Microstrips are *LC*-circuits whose inductance L and capacitance C are evenly distributed over the whole resonator length. Two capacitances of several picofarad isolate each resonator from its microstrip feedlines [see Fig. 1(a) and Fig. 1(c)]. They act as semi-transparent mirrors, giving rise to the formation of standing electromagnetic waves and allowing for signals to couple in and out of the resonator. The standing current and voltage waves inside the resonator have a position dependent amplitude, a wave length λ of twice the resonator length (we may neglect higher harmonics here), and a relative phase shift of 90°. The center frequencies $\omega/2\pi$ of our resonators are in the range of 6-7 GHz. Two resonators can be coupled by bringing them in close vicinity to each other for some part of their length [see Fig. 1(a) and Fig. 1(c)] so that their field modes overlap. We use the term distributed coupling when the amplitude of the field mode varies considerably over the coupling length. We measure the transmission spectrum of the coupled resonators and that of the corresponding single resonator in a ^{4}He evaporation cryostat using a vector network analyzer. For the single resonators, we expect a single Lorentzian peak at the center frequency. For the coupled resonators, this peak is expected to split into two. The magnitude of this splitting equals approximately twice the coupling rate g.

In a first approach, we couple two resonators inductively at their centers in a small region. A typical relative coupling rate for such punctiform coupling is $g/\omega = 1.8\%$ (sample layout and transmission data not shown). As a next step, the resonators can be coupled over a

[1] We acknowledge financial support from the SFB 631 of the German Research Foundation, the German Excellence Initiative via NIM, and the EU Marie Curie Initial Training Network CCQED.
[2] CSIC-Universidad de Zaragoza, Zaragoza, Spain
[3] Institute Néel, Grenoble, France
[4] Instituto de Física Fundamental, CSIC, Madrid, Spain
[5] Universidad del País Vasco and Ikerbaske Foundation, Bilbao, Spain

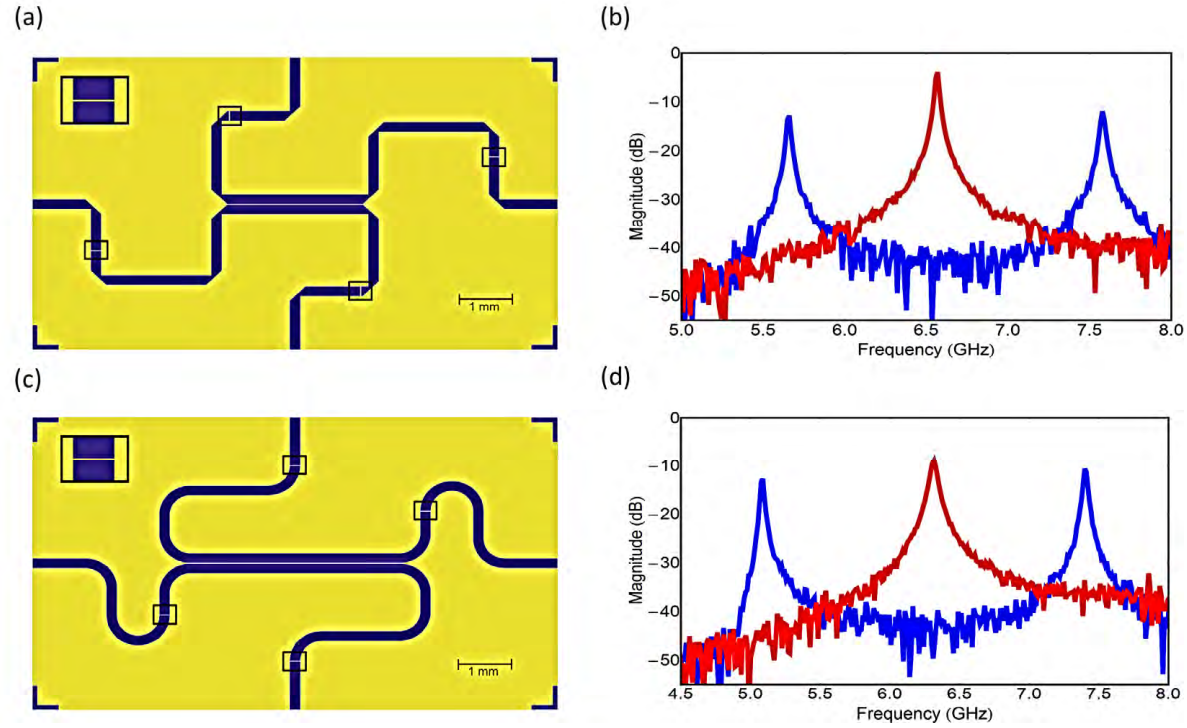

Figure 1: (a), (c) Top view of the distributed coupling samples discussed in this work. Blue: Niobuim microstrips, thickness 100 nm. Yellow: Substrate. Black boxes: Region of the coupling capacitors. Inset: Enlarged coupling capacitor. **(b), (d)** Transmission spectrum of a single (red) and coupled (blue) microstrip resonators for the structures shown in (a) and (c), respectively.

larger length [see Fig. 1(a) and Fig. 1(c)] to further increase g. For such distributed coupling, inductive and capacitive coupling mechanisms characterized by the rates g_i and g_c, respectively, coexist. An accurate treatment based on the full Lagrangian of the system leads to the Hamiltonian

$$\hat{H} = \hbar\tilde{\omega} \sum_{i=1,2} \hat{a}_i^\dagger \hat{a}_i - \hbar\left(g_\mathrm{i} + g_\mathrm{c}\right)\left(\hat{a}_1^\dagger \hat{a}_2 + \hat{a}_1 \hat{a}_2^\dagger\right) - \hbar\left(g_\mathrm{i} - g_\mathrm{c}\right)\left(\hat{a}_1^\dagger \hat{a}_2^\dagger + \hat{a}_1 \hat{a}_2\right), \tag{1}$$

where $\hat{a}_i^\dagger$ and $\hat{a}_i$ are bosonic creation and annihilation operators associated with the fundamental mode of resonator i. We note two main features: first, the resonator frequency is renormalized to $\tilde{\omega}$. This can give rise to an asymmetry of the position of the two coupled resonator peaks with respect to that of the single resonator peak [see, for example, Fig. 1(d)]. Second, the coupling between the two effective resonators is, in contrast to the punctiform case, no longer strictly dipolar. This implies that, in general, the beam splitter term describing the exchange of real photons between the resonators may have a different coupling constant $(g_\mathrm{i} + g_\mathrm{c})$ than the counterrotating terms describing virtual excitations $(g_\mathrm{i} - g_\mathrm{c})$. The punctiform inductive coupling is recovered for $g_\mathrm{c} = 0$. We use the above Hamiltonian to extract the microscopic circuit parameters of the resonator samples shown in Fig. 1(a) and Fig. 1(c) from their transmission spectra of Fig. 1(b) and Fig. 1(d). For space reasons, we omit further the-

oretical details of this procedure here. For the structures of Fig. 1(a) and Fig. 1(c), we obtain $l_m/l_0 = 0.365$, $c_m/c_0 = 0.136$ and $l_m/l_0 = 0.404$, $c_m/c_0 = 0.0789$, respectively. Here, l_0 and c_0 are the self inductances and capacitances per unit length of the microstrips and l_m and c_m are the mutual inductances and capacitances in the coupling region. The results show good agreement. We attribute the remaining differences to geometry effects not included in the model.

In terms of relative coupling rates, we achieve $g/\tilde{\omega} \sim 14\%$ for the sample shown in Fig. 1(a) and $g/\tilde{\omega} \sim 18\%$ for the sample shown in Fig. 1(c). These rates are already comparable to the ultrastrong qubit-resonator coupling rates of 7-12% measured in Ref. [4]. Therefore, a possible quantum processor using ultrafast quantum gates [6] and coupled resonators would not be not limited by the latter. Furthermore, our resonators are candidates for measuring the breakdown of thermal entanglement [7] with cross-correlation techniques [8]. In such a measurement, only coupling strengths comparable to those presented in this work allow for a transition temperature above 100 mK, which is well accessible with today's dilution refrigerators. Finally, we note that Eq. (1) provides us with the possibility to minimize the sometimes disturbing influence of counterrotating wave terms while keeping the desired beam splitter coupling strength large by choosing a suitable coupling region.

References

[1] J. Clarke, and F. K. Wilhelm, Nature **453**, 1031–1042 (2008).
[2] R. J. Schoelkopf, and S. M. Girvin, Nature **451**, 664–669 (2008).
[3] A. Wallraff, D. I. Schuster, A. Blais, L. Frunzio, R.-S. Huang, J. Majer, S. Kumar, S. M. Girvin, and R. J. Schoelkopf, Nature **431**, 162–167 (2004).
[4] T. Niemczyk, F. Deppe, H. Huebl, E. P. Menzel, F. Hocke, M. J. Schwarz, J. J. Garcia-Ripoll, D. Zueco, T. Hümmer, E. Solano, A. Marx, and R. Gross, Nature Physics **6**, 772–776 (2010).
[5] M. Mariantoni, H. Wang, T. Yamamoto, M. Neeley, R. C. Bialczak, Y. Chen, M. Lenander, E. Lucero, A. D. O'Connell, D. Sank, M. Weides, J. Wenner, Y. Yin, J. Zhao, A. N. Korotkov, A. N. Cleland, and J. M. Martinis, Science **334**, 61–65 (2011).
[6] G. Romero, D. Ballester, Y. M. Wang, V. Scarani, and E. Solano. arXiv:110.0223v1 (2011).
[7] G. Vidal, and R. F. Werner, Phys. Rev. A **65**, 032314 (2002).
[8] E. P. Menzel, F. Deppe, M. Mariantoni, M. Á. A. Caballero1, A. Baust, T. Niemczyk, E. Hoffmann, A. Marx, E. Solano, and R. Gross, Phys. Rev. Lett. **105**, 100401 (2010).

Superconducting Microstrip Resonators for Circuit Quantum Electrodynamics Experiments

A. Baust, M. Krawczyk, M. Haeberlein, E. Hoffmann, U. Ehmann, N. Kalb, F. Deppe, A. Marx, R. Gross [1]

Superconducting waveguide resonators acting as "photon boxes" are fundamental elements of most circuit quantum electrodynamics (QED) [1] setups. In contrast to the widely used coplanar waveguide (CPW) geometries, microstrip resonators are promising with respect to scalability. The microrstrip geometry (cf. Fig. 1) facilitates the straightforward implementation of additional circuit elements and control lines. Furthermore, the transmission spectra of microstrip resonators typically exhibit almost no parasitic modes up to 20 GHz even for more intricate geometries. On the downside, due to their field distribution microstrip resonators are not expected to show high quality factors even at very low temperatures.

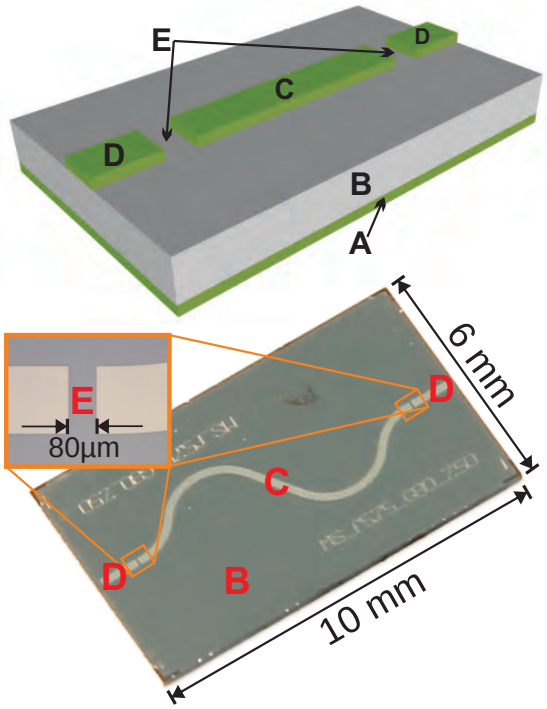

Figure 1: Schematic (top) and photograph (bottom) of a microstrip resonator. **A** Nb ground plane. **B** Silicon substrate. **C** Resonator. The resonance frequency is mainly determined by the length ($l = 9200\,\mu$m) of the line. **D** Feed lines connecting the resonator to external circuitry. **E** Gaps defining the coupling capacity between resonator and feed lines.

The quality factor $Q = \left|\omega_R \cdot E(t) \Big/ \left(\frac{dE(t)}{dt}\right)_t\right|$ relates the total energy $E(t)$ stored in the resonator to the energy loss per second, where ω_R is the angular resonance frequency. Fortunately, Q-factors between 1000 and 10000 are sufficient for many circuit QED experiments. In this work, we present a systematic study [2] of microstrip resonators with emphasis on the temperature and excitation power dependence of their Q-factors. The resonators are made of 100 µm thick Nb on a SiO_2 (50 nm) coated 250 µm thick Si substrate (cf. Fig. 1). They have a resonance frequency of $\omega/2\pi \approx 5.8$ GHz and are coupled to the feed lines via two gap capacitors with gap widths ranging from 5 µm to 320 µm. Both resonator and feed lines are 50 Ω-matched. We determine the Q-factors from transmission experiments with a vector network analyzer. From the spectra we extract the loaded quality factor $Q_L = \left(Q_{ext}^{-1} + Q_{int}^{-1}\right)^{-1}$. The external quality factor Q_{ext} accounts for the energy coupled in and out of the resonator via the gap capacitors. The internal quality factor Q_{int} includes all energy losses caused by imperfections of the resonator such as quasiparticle excitations in the superconductor, dielectric losses or radiation into free space. At 4.2 K in a liquid He bath cryostat and high excitation power ($\gg -60$ dBm), we find that Q_L increases from 210 for the smallest to 19000 for the largest gap (cf. Fig. 2).

[1] This work is supported by the German Research Foundation via SFB 631, the German Excellence Initiative via NIM and the EU Marie-Curie network CCQED.

In addition, we have characterized the microstrip resonators with 80 µm and 320 µm gap at millikelvin temperature. We use attenuated input lines and an amplification chain limited by the noise of a cryogenic HEMT amplifier at the resonator output. We study the transmission through the resonators with probe powers down to those typically used in circuit QED experiments at different temperatures ranging from 40 – 600 mK using a vector network analyzer. The results, which are shown in Fig. 3, qualitatively agree with those for CPW geometries [3]. For both resonators types, Q saturates at low and high values for low and high probe powers, respectively. This can be understood considering that the main loss mechanism is the coupling of the resonator to a bath of two-level states (TLS) in the dielectric. At high power and high temperatures, these TLS are saturated, but for low power they absorb and disperse energy [4]. For microstrip resonators these TLS are more relevant than for coplanar waveguides because all electric field lines going from the resonator's signal line to its ground plane penetrate the dielectric.

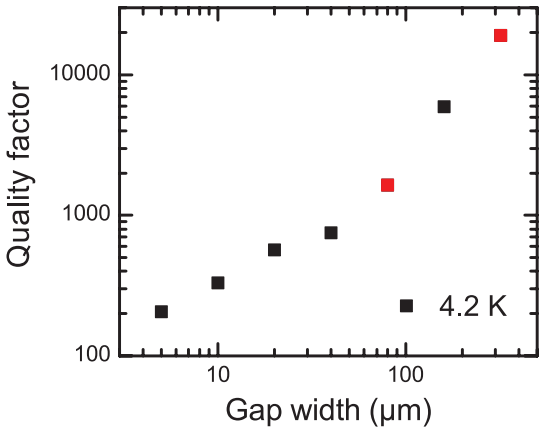

Figure 2: Loaded quality factor plotted against the gap width. Increasing the gap from 5 µm to 320 µm increases the quality factor by two orders of magnitude. The red dots denote the resonators also measured at mK-temperatures.

For the resonator with the 80 µm gap the loaded quality factor is limited by the small external quality factor at high power. Hence, we extract an external quality factor of $Q_{\mathrm{ext}} = (3.1 \pm 0.2) \cdot 10^3$ for a temperature of 40 mK, assuming that Q_{int} is at least one order of magnitude larger than Q_{ext}. Further assuming that the external quality factor is independent of probe power, we can calculate the internal quality factor for low power from the loaded quality factor $Q_{\mathrm{L}} = (1.7 \pm 0.1) \cdot 10^3$ and find a value of $Q_{\mathrm{int}} = (3.8 \pm 0.6) \cdot 10^3$, again at 40 mK. For the 320 µm-gap resonator we observe a loaded quality factor of $Q_{\mathrm{L}} = (5.9 \pm 0.1) \cdot 10^4$ at a temperature of 40 mK and high power defining a lower limit for both the external and the internal quality factor. For low power, the loaded quality factor of $Q_{\mathrm{L}} = (3.7 \pm 0.3) \cdot 10^3$ yields an internal quality factor of $Q_{\mathrm{int}} = (3.85 \pm 0.45) \cdot 10^3$. As expected, the low-power internal quality factors of both resonators, which should not depend on the gap width, are in

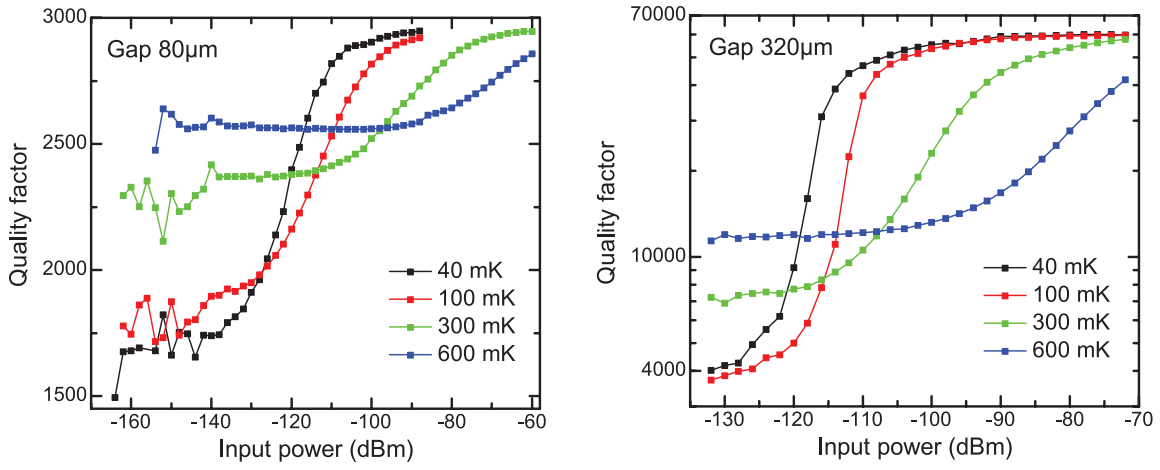

Figure 3: Loaded quality factors at millikelvin temperatures as a function of the power applied to the input port of the respective resonator sample.

agreement with each other within the uncertainty bound. We find for both resonators that the low-power saturation value of the loaded quality factor rises with increasing temperature. This can be understood considering that the number of saturated TLS in the dielectric increases with increasing temperature. For a temperature of 600 mK, the resonator with the 320 µm gap shows an internal quality factor of $Q_{\mathrm{int,600mK}} = (1.35 \pm 0.15) \cdot 10^4$, provided that the external quality factor is independent of the temperature.

In conclusion, we have characterized microstrip resonators with different gap widths at various temperatures and probe power values. At millikelvin temperatures and low probe power, we have demonstrated internal quality factors $Q_{\mathrm{int}} \approx 4000$ which are suitable for circuit QED applications. However, a study on microwave dielectric loss performed by O'Connell *et al.* [4] suggests that using a different substrate, e.g. sapphire or high-resistivity silicon, the latter possibly without SiO_2 layer, could further increase Q_{int} significantely.

References

[1] R. J. Schoelkopf, and S. M. G, Nature **451**, 664–669 (2008).

[2] M. Krawczyk. *Superconducting microstrip resonators for circuit quantum electrodynamics experiments*. Master thesis, TU München (2011).

[3] P. Macha, S. H. W. van der Ploeg, G. Oelsner, E. Il'ichev, H.-G. Meyer, S. Wünsch, and M. Siegel, Appl. Phys. Lett. **96**, 062503 (2010).

[4] A. D. O'Connell, M. Ansmann, R. C. Bialczak, M. Hofheinz, N. Katz, E. Lucero, C. McKenney, M. Neeley, H. Wang, E. M. Weig, A. N. Cleland, and J. M. Martinis, Appl. Phys. Lett. **92**, 112903 (2008).

Electric Field-Controlled Manipulation of the Magnetization in Ni/$BaTiO_3$ Hybrid Structures

S. Geprägs, A. Brandlmaier, M. Opel, R. Gross, and S. T. B. Goennenwein [1]

New functionalities arise if the magnetic and the dielectric degrees of freedom are coupled in a given material [1]. Such a magnetoelectric interaction will be particularly strong in systems which simultaneously exhibit both ferromagnetism and ferroelectricity, i.e. in magnetoelectric multiferroics. Unfortunately, these materials are scarce in nature. Attractive alternatives are composites, in which ferromagnetic and ferroelectric compounds are artificially assembled. In these structures, large extrinsic magnetoelectric effects at room temperature can be engineered by exploiting the elastic coupling between the two ferroic constituents: An electric field applied to the ferroelectric layer results in an expansion or contraction of its shape caused by converse piezoelectric effects. Due to the intimate contact of the ferroelectric and ferromagnetic constituents, this distortion is mechanically transferred into the ferromagnetic layer and entails a variation of the magnetization due to converse magnetostriction [e.g. Ref. [2]].

Here, we report on the manipulation of the ferromagnetic magnetization M via electric fields E in Ni/$BaTiO_3$ hybrid structures. The samples consist of polycrystalline Ni films deposited on $BaTiO_3$ single crystals [3]. Figure 1 shows the electric field dependence of the projection of the magnetization $M(E)$ along a constant magnetic field H. Reversible changes of M up to 20% are observed as a function of E. Furthermore, the $M(E)$ loops exhibit a butterfly like shape. This indirectly proves that the elastic strain transferred from the $BaTiO_3$ substrate into the Ni thin film is the driving force here. At room temperature, $BaTiO_3$ is tetragonal with the polarization along the c-axis of the unit cell, which yields six possible ferroelectric or three different ferroelastic domains. If the polarization is pointing out-of-plane, the corresponding domains are called c-domains, while domains with in-plane polarization are denoted by a_1- and a_2-domains. By applying an electric field across the $BaTiO_3$ substrate, a ferroelastic single c-domain state can be obtained imposing uniform strain in the overlying ferromagnetic Ni thin film. Upon decreasing the electric field to zero, a_1- and a_2-domains are formed with equal probability in the $BaTiO_3$ substrate. However, by using miscut $BaTiO_3$ substrates, the formation of one kind of a-domains is preferred [4]. In this case, a ferroelastic multi-domain state is present at $E = 0\,\mathrm{kV/m}$ consisting of ferroelastic c- and a_2-domains [see Fig. 2]. The tetragonal unit cells of the emerging a_2-domains are oriented with the longer c-axis parallel to the $BaTiO_3$ surface and therefore induce tensile strain in parts of the Ni thin film, which are elastically clamped to these ferroelastic domains. This tensile strain causes a large uniaxial magnetic anisotropy due to converse magnetoelastic effects and thus changes the orientation of the magnetization. In contrast, the magnetic properties of Ni on top of ferroelastic c-domain regions stay nearly unaffected. Therefore, the mixed ferroelastic multi-domain state close to $E = 0\,\mathrm{kV/m}$ induces a heterogeneous magnetic state in the overlying Ni thin film.

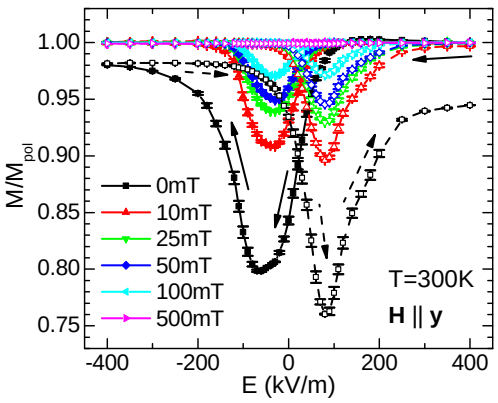

Figure 1: Magnetization M as a function of the applied electric field E of a 100 µm thick Ni film deposited on a 0.5 mm thick $BaTiO_3$ substrate. M is normalized to $M_{\mathrm{pol}} = M(400\,\mathrm{kV/m})$.

[1] This work is supported by the German Research Foundation via GO 944/3-1 and the German Excellence Initiative via the "Nanosystems Initiative Munich (NIM)".

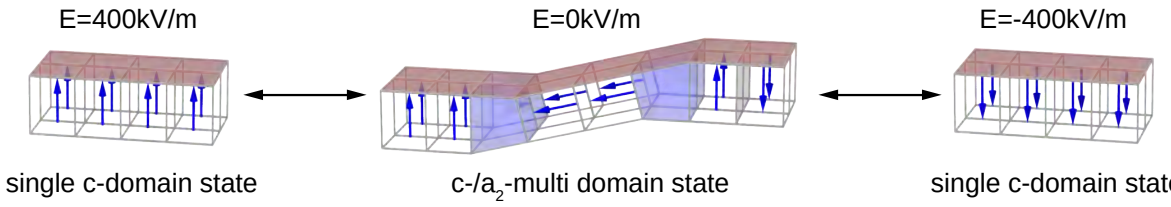

Figure 2: Ferroelastic domain evolution in miscut $BaTiO_3$ substrates as a function of the applied electric field E. The ferroelectric polarization P is denoted by blue arrows and the overlying Ni thin film is marked in red.

Hence, the $M(E)$ loops shown in Fig. 1 should be a direct measure of the volume fraction of the emerging a_2-domains in the $BaTiO_3$ substrate.

Due to the ferroelastic nature of the $BaTiO_3$ substrate, irreversible domain wall effects can play a dominant role during the formation of c- and a-domains under weak electric field conditions, which results in non-linearities of the converse piezoelectric response. The non-linear strain dependence causes a hysteretic $M(E)$ behavior in the Ni thin film with two different values of M at $E = 0\,\mathrm{kV/m}$, depending on the sweep history [see Fig. 3(a)]. This can be utilized to switch the remanent magnetization M from one electro-remanent state at $E = 0\,\mathrm{kV/m}$ to another, and back to the initial state, by applying the electric field sequence $+20\,\mathrm{kV/m} \rightarrow 0\,\mathrm{kV/m} \rightarrow -20\,\mathrm{kV/m}$ to the $BaTiO_3$ substrate [see Fig. 3(b)]. Therefore, it is possible to change the magnetization M electrically between two well-defined remanent magnetic states.

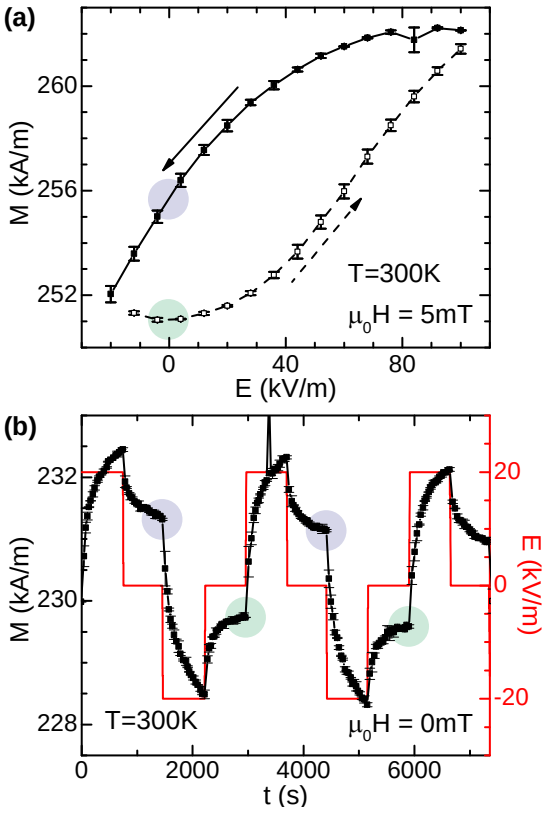

Figure 3: (a) $M(E)$ measured at a constant magnetic field of 5 mT. The two different magnetic states at $E = 0\,\mathrm{kV/m}$ are marked by the full circles. (b) M can by switched between two electro-remanent states (full circles) by appropriately ramping the electric field (red line).

In summary, we showed that the interaction between dielectric, mechanical, and magnetic degrees of freedom allows us to tune electrically the magnetization in $Ni/BaTiO_3$ hybrid structures. In these structures, the magnetization can be changed reversibly by about 20% due to the combined action of converse piezoelectric and magnetoelastic effects. Furthermore, two different remanent magnetization states can be realized electrically, which enables a non-volatile all-electronic magnetization control.

References

[1] S. Geprägs, M. Opel, S. T. B. Goennenwein, and R. Gross, Phil. Mag. Lett. **87**, 141 (2007).
[2] A. Brandlmaier, S. Geprägs, G. Woltersdorf, R. Gross, and S. T. B. Goennenwein, J. Appl. Phys. **110**, 043913 (2011).
[3] S. Geprägs, A. Brandlmaier, M. Opel, R. Gross, and S. T. B. Goennenwein, Appl. Phys. Lett. **96**, 142509 (2010).
[4] S. Geprägs. *Magnetoelectric Interactions in Multiferroic Thin Films and Composites*. Phd thesis, TU München (2011).

Spin injection and spin transport in the wide bandgap semiconductor zinc oxide

M. Althammer, D. Venkateshvaran, R. Gross, S. T. B. Goennenwein, M. Opel [1]
C. Schwark, V. Klinke, B. Beschoten [2]

The wide bandgap semiconductor ZnO has been proposed as a candidate for semiconductor spintronics because of its small spin-orbit coupling [1] implying in a large spin coherence length. However, its electronic and excitonic structures have been debated for a long time. Only few measurements of the carrier relaxation or coherent spin dynamics in ZnO have been published to date [2–4] yielding spin coherence times of 2 ns for epitaxial ZnO thin films. We apply time-resolved Faraday rotation (TRFR, all-optical pumping/probing) as well as Hanlé–magneto-optical Kerr effect (Hanlé–MOKE, electrical pumping/optical probing) to investigate the spin dynamics in thin films of ZnO.

High quality thin film deposition

Thin films of ZnO are most commonly grown on Al_2O_3 (sapphire). However, due to the large lattice mismatch between ZnO ($a = 0.3250$ nm, $c = 0.5213$ nm) and Al_2O_3 ($a = 0.4754$ nm, $c = 1.299$ nm) which amounts to 18.4% even after a 30° in-plane rotation the as-grown ZnO films usually show a large mosaic spread indicated by a full width at half maximum (FWHM) of the rocking curves of $> 0.5°$, high residual carrier densities (most likely due to native defects) and low mobilities. It was shown recently, that employing a MgO/ZnMgO buffer layer on the (0001)-oriented Al_2O_3 substrate leads to a smoother thin film surface and can significantly improve the structural quality of the top ZnO layer [5, 6].

The samples for the TRFR experiment (sample A) were grown at the WMI by laser molecular beam epitaxy (laser-MBE) with a KrF excimer laser ($\lambda = 248$ nm) from a stoichiometric ZnO target in 10^{-3} mbar of oxygen on a single crystalline, (0001)-oriented Al_2O_3 substrate. After annealing the substrate at 850°C for 1 h, a 300 nm thin ZnO film was deposited at 400°C with a laser fluence of 1 J/cm^2 and a repetition rate of 2 Hz. High-resolution X-ray diffraction (HR-XRD) shows no secondary phases in the ω-2θ scan (Fig. 1(a)). Around the ZnO(0002) reflection, satellites due to Laue oscillations are clearly visible (Fig. 1(b)), indicating the high structural quality of the ZnO thin film and coherent growth with small surface and interface roughness. The rocking curve at the ZnO(0002) reflection yields a full width at half maximum (FWHM) of only 0.03° (Fig. 1(c)) despite the large lattice mismatch of 18.4% to the substrate, indicating a low mosaic spread and demonstrating that the structural quality is on par with other reports [6].

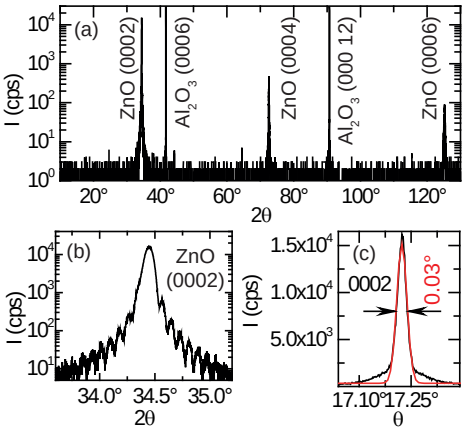

Figure 1: HR-XRD data from a ZnO thin film deposited on a (0001)-oriented Al_2O_3 substrate. (a) ω-2θ-scan indicating no secondary phases, (b) ZnO(0002) reflection on an enlarged scale showing satellites due to Laue oscillations, (c) rocking curve of the ZnO(0002) reflection with Gauss fit (red).

[1] This work was supported by the "German Research Foundation" via priority program SPP1285 (project number GR 1132/14).

[2] 2. Physikalisches Institut A, RWTH Aachen, Germany.

The samples for the Hanlé-MOKE experiment (sample B) were prepared in the same way with a ZnO thickness of 200 nm. Then, a 15 nm thin polycrystalline Co layer was deposited *in-situ* at room temperature using electron beam evaporation. Using photolithography and Ar ion beam milling, a ring-shaped mesastructure was defined. As a final production step, the 30 nm thin Au top electrode was deposited via RF sputtering and lift-off technique. Samples A and B were mechanically polished on the back side for better optical transmission characteristics.

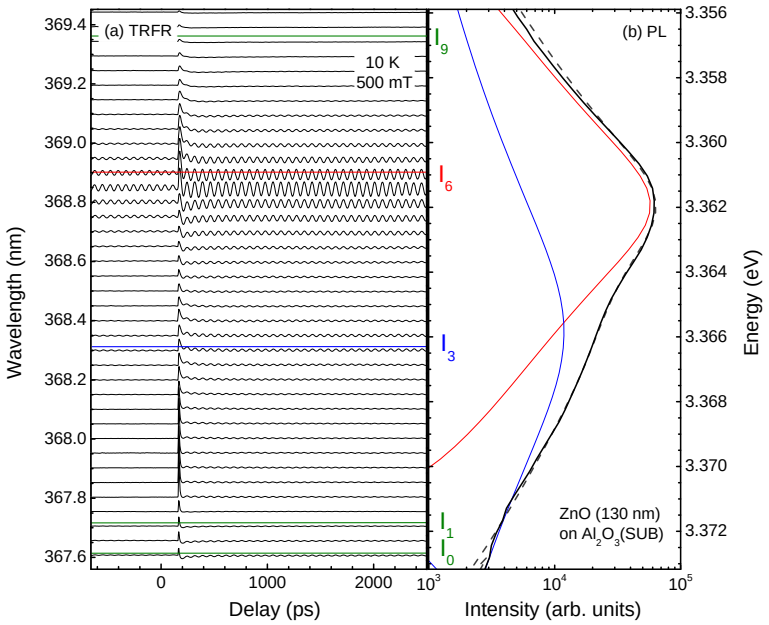

Figure 2: Comparison of (a) wavelength-dependent TRFR data and (b) PL data, at 10 K and 500 mT for sample A.

Spin relaxation and spin coherence: optical pumping & optical probing

In collaboration with the RWTH Aachen University, we investigated the spin dephasing time of sample A by TRFR experiments. A circularly polarized laser pulse with a wavelength close to the bandgap creates a spin polarization in the conduction band of ZnO. After a certain delay time and in an external magnetic field applied in-plane perpendicular to the incident beam, the precession of this spin ensemble is being probed by a second linearly polarized laser pulse. The magnitude of this TRFR signal is found to depend on the pump/probe wavelength (Fig. 2(a)). Its maximum is correlated to the prominent excitonic *I*-lines in the photoluminescence (PL) spectra (Fig. (b)). At 10 K, the obtained spin coherence time shows a maximum of $T_2^* = 15$ ns for a wavelength of 368.9 nm corresponding to an exciton bound to a neutral aluminum donor (I_6-line, red in Fig. 2). A second maximum for 368.3 nm corresponds to the I_3-line of an ionized donor-bound exciton (blue) and yields $T_2^* = 10$ ns. These values are by far exceeding published data for ZnO thin films [2]. With increasing temperature, the TRFR signal becomes weaker and disappears between 50 K and 70 K (not shown here). This is in good agreement with the

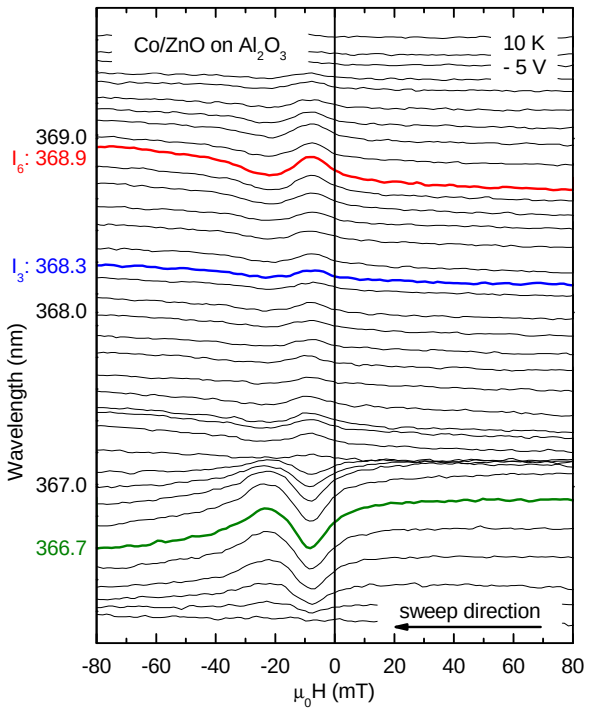

Figure 3: Hanlé–MOKE data from sample B as a function of the probe wavelength at 10 K. The voltage applied to the sample for spin injection was −5 V, the magnetic field was swept from positive to negative values.

behavior of donor-bound excitons as they thermally dissolve around 60 K such that we do no longer expect a TRFR signal at the corresponding wavelengths.

Hanlé–MOKE: electrical spin injection & optical probing

We further analyzed the electrical injection of spin-polarized carriers into ZnO in sample B via a dc current from the Co electrode by an optical detection scheme (Hanlé–MOKE). A linearly polarized probe pulse is used to determine the projection of the spin polarization while sweeping the external magnetic field. At 10 K, we again find a strong dependence of the Hanlé–MOKE amplitude on the energy of the probing laser beam (Fig. 3). Maxima in the amplitude at the I_6-line, the I_3-line, and at 366.7 nm appear in the spectra. Interestingly, the measured $T_2^* = 1$ ns is independent of the wavelength of the probing laser beam. Moreover, the observed Hanlé–MOKE signal vanishes for temperatures above 40 K (not shown here), again indicating a correlation between donor-bound excitons and the observed spin injection signal. To our knowledge, these experiments are the first successful realization of electrical spin injection into ZnO thin films. The injection efficiency of the heterostructure is still low, giving room for further improvement in the future. We plan to extend these Hanlé–MOKE experiments to half-metallic injection electrodes in epitaxial Fe_3O_4/ZnO heterostructures.

References

[1] J. Y. Fu, and M. W. Wu, J. Appl. Phys. **104**, 093712 (2008).
[2] S. Ghosh, V. Sih, W. H. Lau, D. D. Awschalom, S.-Y. Bae, S. Wang, S. Vaidya, and G. Chapline, Appl. Phys. Lett. **86**, 232507 (2005).
[3] S. Ghosh, D. W. Steuerman, B. Maertz, K. Ohtani, H. Xu, H. Ohno, and D. D. Awschalom, Appl. Phys. Lett. **92**, 162109 (2008).
[4] N. Janßen, K. M. Whitaker, D. R. Gamelin, and R. Bratschitsch, Nano Lett. **8**, 1991 (2008).
[5] A. El-Shaer, A. C. Mofor, A. Bakin, M. Kreye, and A. Waag, Superlattices Microst. **38**, 265 (2005).
[6] T. A. Wassner, B. Laumer, S. Maier, A. Laufer, B. K. Meyer, M. Stutzmann, and M. Eickhoff, J. Appl. Phys **105**, 023505 (2009).

Materials, Thin Film and Nanotechnology, Experimental Techniques

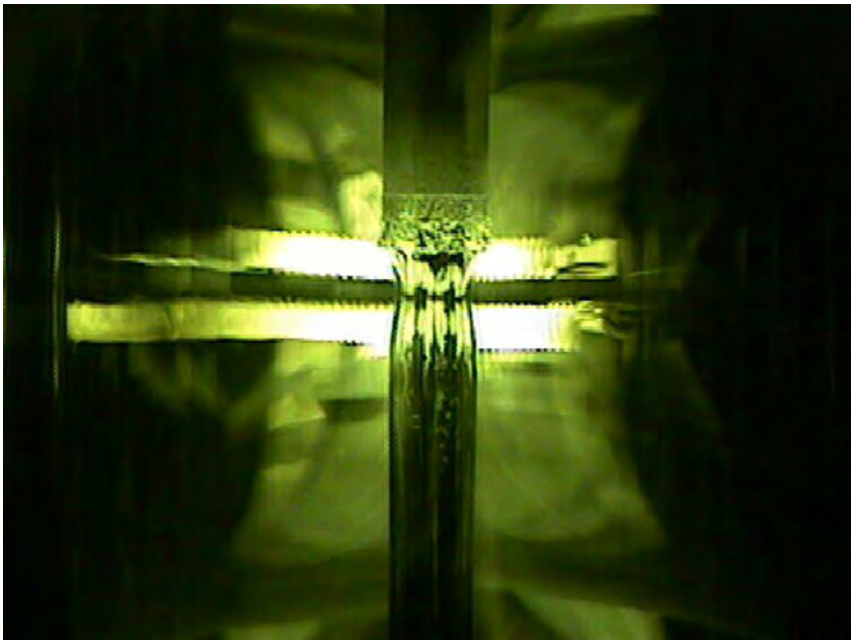

Growth of a $Pr_{2-x}Ce_xCuO_4$ single crystal by the traveling solvent floating zone method in a four-mirror image furnace.

New! Cryogen-free Dilution Refrigerator with 1K-Circuit

K. Uhlig

General remarks

In cryogen-free dilution refrigerators (CF-DR) there is no 1K-stage to condense the back-streaming ^{3}He. Instead, after being pre-cooled by a two-stage pulse tube refrigerator (PTR) [1], the ^{3}He is condensed in a counter-flow heat exchanger where the latent heat of vaporization is transferred to the cold ^{3}He gas pumped from the still of the DR [2]. Currently, all commercial manufacturers of CF-DRs use this method.

There are experimental applications, however, where high cooling capacities are required at a temperature near 1 K to cool amplifiers and to heat sink cables. For applications where the cooling capacity of the still ($T \approx 0.7$ K) is not sufficient (e.g. superconducting quantum circuitry), an additional cooling stage is desirable [3, 4].

In last year's annual report, we described how a ^{4}He-JT-circuit was installed in our CF-DR; operating temperatures of the cooling circuit were near 1K, and cooling capacities up to 100 mW . So far, the new 1K-stage was run alone without the DR in operation. Now, the dilution refrigeration unit and the 1K-stage are installed in the cryostat. They are pre-cooled by the same PTR [5].

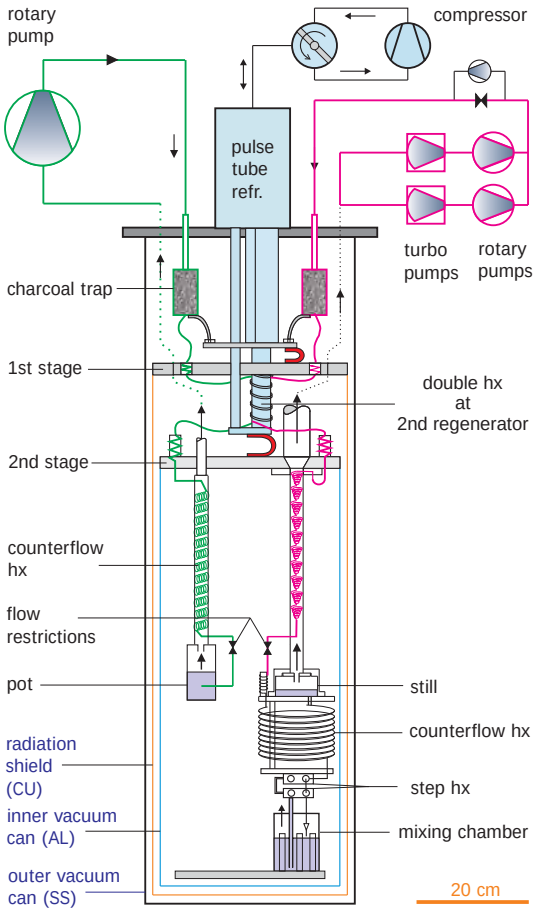

Figure 1: Cross section of our CF-DR (pink) with 1K-stage (green). Both flow circuits are pre-cooled by the same pulse tube cryocooler.

Most commercial DRs are equipped with quite powerful PTRs with power consumptions of over 9 kW. In our cryostat a small PTR (4.7 kW) [6] is used to demonstrate that a PTR with low power consumption (and a low level of vibration) is sufficient to pre-cool a powerful mK-cryocooler and an additional 1K-circuit.

Cryostat, results

In Fig. 1, the layout of the cryostat is depicted. The ^{3}He of the DR and the ^{4}He of the 1K-stage enter the cryostat through charcoal traps which are thermally anchored at the 1st stage of the PTR ($T \approx 50$ K); there are no LN_2 cooled traps in the DR. Next, the gas streams are further cooled in a double heat exchanger (hx) which consists of two capillaries which are soldered to the outside of the 2nd regenerator of the PTR. Here, the large heat capacity of the cold He gas of

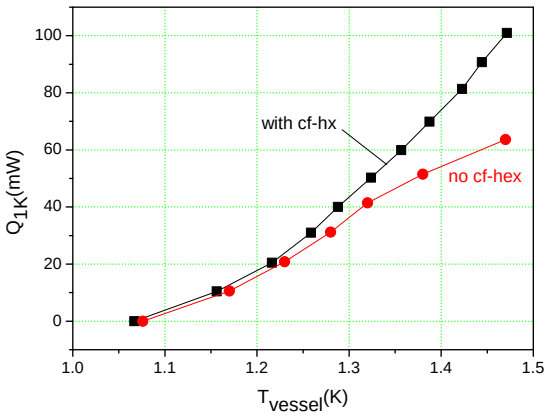

Figure 2: Cooling capacity Q_{1K} of the 1K-circuit as a function of its temperature. The black curve shows Q_{1K} when a counterflow hx is installed (Fig. 1). The red curve is for a setup where the counterflow hx was omitted [5].

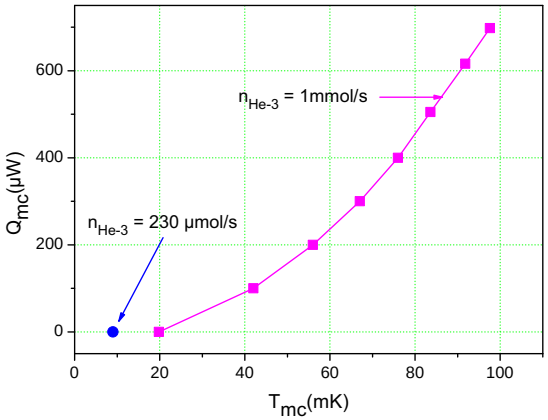

Figure 3: Refrigeration capacity Q_{mc} of the mixing chamber of the DR. The pink curve is for a high ^{3}He flow of 1 mmol/s; Q_{mc} reaches 700 μW at a temperature of 100 mK. The lowest temperature is just below 10 mK for a flow of 0.23 mmol/s.

the PTR is used to cool the small helium streams of the DR and the 1K-circuit to 2.5 K < T < 3 K; thereby, the cooling capacity of 2nd stage of the PTR is not noticeably affected [7]. This heat exchanger is extremely important to make the best use of the refrigeration capacity of the PTR.

At the 2nd stage of the PTR, the liquid ^{3}He/^{4}He streams are liquefied and cooled to 2.5 K in two little heat exchangers. Next, the streams are further cooled in counter-flow heat exchangers before they are expanded in flow restrictions. The counter-flow heat exchangers are made from capillaries, but are not identical; in one case the capillaries were bent to a stack of small cones (DR), and in the other one it was made from a spiral construction (photo in [8]). The liquid fraction of the ^{4}He of the 1K-stage can accumulate in a vessel, whereas the ^{3}He of the DR is run to the dilution unit. The two flow circuits are not coupled so they can be operated separately or together [9, 10]. Their cooling capacities are shown in Fig. 2 and Fig. 3, respectively.

With our present setup, a refrigeration capacity of up to 100 mW could be reached with the 1K-circuit. At the same time the maximum cooling power of the DR was 0.7 mW at a temperature of the mixing chamber of 100 mK, and an additional amount of $\approx$ 30 mW was available at the still at a temperature of 0.8 K. We plan to adopt the novel concept described above in a new cryostat which is being built for experiments on superconducting quantum circuits.

References

[1] R. Radebaugh. Development of the pulse tube refrigerator as a efficient and reliable cryocooler. Tech. Rep., NIST, Boulder (2000).
[2] K. J. Uhlig, Adv. Cryo. Eng. **53B**, 1287–1291 (2007).
[3] M. Hollister, and A. Woodcraft, Cryogenics **49**, 371–375 (2009).
[4] K. Uhlig, Cryocoolers **16**, 509–513 (2010). Http://hdl.handle.net/1853/38855.
[5] K. Uhlig, Adv. Cryo. Eng. **56** (2011). To be published.
[6] Cryomech Inc., Syracuse, N.Y.
[7] K. Uhlig, Cryogenics **48**, 138–141 (2008).
[8] K. Uhlig, Cryogenics **27**, 454–457 (1987).
[9] K. Uhlig, Jounal of Physics: Conference Series (2011). To be published.
[10] K. Uhlig. Ann. Rep. WMI, 71-73; www.wmi.badw.de/publications/jahresberichte/2010.pdf (2010).

The WMI Sample Basis for High T_c Superconductor Research

Andreas Erb [1]

Probing the Phase Diagram of the Cuprates

For comprehensive studies of the exciting phenomena of high temperature superconductivity in the cuprates the study of the doping dependence of different physical properties and ordering phenomena seems to be crucial to solve the enigma of the underlying mechanism of superconductivity in these compounds. While in the early days of research in high temperature superconductivity, most experiments were performed on optimally doped samples it is now understood that the key to the understanding may most probably be found in the regions of doping which are in close vicinity to the antiferromagnetic region and in the region where superconductivity vanishes at high doping. Many superconducting cuprates have been successfully synthesized in the last 20 years but there are only a few compounds, which can be grown as stable high quality single crystals in a wide region of doping. Even though some compounds like $Bi_2Sr_2CaCu_2O_8$ can be grown relatively easily, and their easy cleaving crystals make ideal samples for spectroscopic methods the off-stoichiometric ratio of the metals Ba,Ca and Sr in these compounds leads to local inhomogeneities in doping and thus hamper their use in doping dependent studies. The same applies for the Tl- and Hg- based compounds with additional difficulties due to toxicity and volatility of Hg and Tl. The ideal crystal system in terms of crystal perfection is of course a crystal with fixed atomic ratios in a compositional phase diagram, however no variation in doping is possible with fixed atomic ratios which makes such a compound useless for studies of the doping dependence,. A lucky partial exception is the cuprate $YBa_2Cu_3O_{7-\delta}$, which at least has a fixed atomic ratio in the metal sublattice and only the oxygen content, which can be varied between 6 and 7 does all the doping from the antiferromagnetic insulator with oxygen content of 6.0 over the so-called region of optimal doping with an oxygen content of 6.9, to the already slightly overdoped fully oxygenated samples of $YBa_2Cu_3O_7$. It should be noted here that many of the most striking results in the last years on $YBa_2Cu_3O_{7-\delta}$ samples in the studies of vortex matter [1–3] or in transport measurements revealing clear Shubnikov-de Haas (SdH) oscillations [4–6] have been obtained on either fully oxygenated samples or on well ordered samples with oxygen contents of 6.25 or 6.5. As it can be seen from the phase diagram in Fig. 1 the region for the use of $YBa_2Cu_3O_{7-\delta}$ as the only compound on the hole doped side of the cuprates is limited by the oxygen content of 7.0, which means that only a slight overdoping can be achieved.

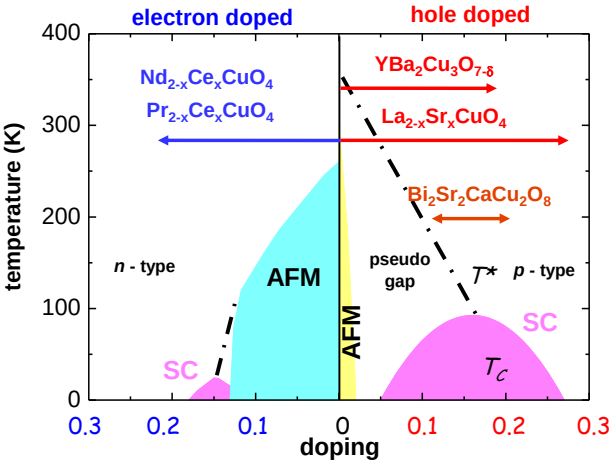

Figure 1: The phase diagram of the high temperature superconductors and the accessible regions for the different compounds

[1]The project has been supported by the German Research Foundation via the Research Unit FOR 538 and grant GR 1132/15.

The WMI Sample Basis

As noted above a single crystal of a stoichiometric compound is of course the most perfect single crystal possible, however given the limited number of cuprate compounds with a wide doping range, the first choice are the so-called 214-compounds, which are represented by $La_{2-x}Sr_xCuO_4$ on the hole- and with $Nd_{2-x}Ce_xCuO_4$ on the electron doped side of the phase diagram. The similarity of the compounds $La_{2-x}Sr_xCuO_4$ and $Nd_{2-x}Ce_xCuO_4$, differing only in the absence apical oxygen sites for $Nd_{2-x}Ce_xCuO_4$, the absence of bi-layers in these compounds and the similarity in the critical temperature allows a more direct comparison of the n- and p-doped side of the phase diagram. In the past years we have not grown $YBa_2Cu_3O_{7-\delta}$ in the nowadays canonical way invented by the author [7] and reproduced by one other group [8], but also mastered the production and growth of the 214 compounds to a level that even the formerly not well understood electron doped side of the phase diagram can be probed with samples of such a quality that Shubnikov-de Haas (SdH) oscillations could be obtained on such samples [9, 10]. The crystal growth group of the WMI is now in the quite unique and exceptional situation that we can supply samples over the whole span of the phase diagram of the cuprates in monocrystalline form and pristine quality. This not only led to numerous publications from groups working inside the WMI [11–14], but also to a demand for samples from leading international groups resulting in several collaborations and publications [15–17] (only 2011 publications mentioned here). In this way the crystal growth group of Walther-Meißner-Institute (WMI) not only supports the worldwide efforts in research on high T_c materials, but also increases the outside visibility of WMI.

References

[1] J. White, V. Hinkov, R. Heslop, R. Lycett, E. Forgan, C. Bowell, S. Straessle, A. Abrahamsen, M. Laver, C. Dewhurst, J. Kohlbrecher, J. Gavilano, J. Mesot, B. Keimer, and A. Erb, Phys. Rev. Lett. **102**, 097001 (2009).
[2] S. P. Brown, D. Charalambous, E. Jones, E. Forgan, P. Kealey, A. Erb, and J. Kohlbrecher, Phys. Rev. Lett. **92**, 067004 (2004).
[3] M. Roulin, A. Junod, A. Erb, E. Walker, R. Flükiger, and J. Sierro, Phys. Rev. Lett. **80**, 1722 (1998).
[4] N. Doiron-Leyraud, C. Proust, D. LeBoeuf, J. Levallois, J.-B. Bonnemaison, R. Liang, D. A. Bonn, W. N. Hardy, and L. Taillefer, Nature **447**, 565 (2007).
[5] C. Jaudet, D. Vignolle, A. Audouard, J. Levallois, D. LeBoeuf, N. Doiron-Leyraud, B. Vignolle, M. Nardone, A. Zitouni, R. Liang, and et al., Phys. Rev. Lett. **100**, 187005 (2008).
[6] S. E. Sebastian, N. Harrison, E. Palm, T. P. Murphy, C. H. Mielke, R. Liang, D. A. Bonn, W. N. Hardy, and G. G. Lonzarich, Nature **454**, 200 (2008).
[7] A. Erb, E. Walker, and R. Flukiger, Physica C **245**, 245–251 (1995).
[8] R. Liang, D. A. Bonn, and W. N. Hardy, Physica C **304**, 105 (1998).
[9] M. Lambacher, T. Helm, M. Kartsovnik, and A. Erb, Eur. Phys. J. Special Topics **188**, 61–72 (2010).
[10] T. Helm, M. V. Kartsovnik, M. Bartkowiak, N. Bittner, M. Lambacher, A. Erb, J. Wosnitza, and R. Gross, Phys. Rev. Lett. **103**, 157002 (2009).
[11] N. Munnikes, B. Muschler, F. Venturini, L. Tassini, W. Prestel, S. Ono, Y. Ando, D. C. Peets, W. N. Hardy, R. Liang, D. A. Bonn, A. Damascelli, H. Eisaki, M. Greven, A. Erb, and R. Hackl, Phys. Rev. B **84**, 144523 (2011).
[12] S. Caprara, C. D. Castro, B. Muschler, W. Prestel, R. Hackl, M. Lambacher, A. Erb, S. Komiya, Y. Ando, and M. Grilli, Phys. Rev. B **84**, 054508 (2011).
[13] B. Moritz, S. Johnston, T. P. Devereaux, B. Muschler, W. Prestel, R. Hackl, M. Lambacher, A. Erb, S. Komiya, and Y. Ando, submitted to Physical Review B **arXiv:1106.5798** (2011).
[14] M. V. Kartsovnik, T. Helm, C. Putzke, F. Wolff-Fabris, I. Sheikin, S. Lepault, C. Proust, D. Vignolles, N. Bittner, W. Biberacher, A. Erb, J. Wosnitza, and R. Gross, New J. Phys. **13**, 015001 (2011).
[15] J. White, R. Heslop, A. Holmes, E. Forgan, V. Hinkov, N. Egetenmeyer, J. Gavilano, M. Laver, C. Dewhurst, R. Cubitt, and A. Erb, Phys. Rev. B **84**, 104519 (2011).
[16] S. Bosma, S. Weyeneth, R. Puzniak, A. Erb, A. Schilling, and H. Keller, Phys. Rev. B **84**, 024514 (2011).
[17] M. Reibelt, S. Weyeneth, A. Erb, and A. Schilling, Supercond. Sci. Technol. **24**, 105019 (2011).

Preparation of Highly Ordered $YBa_2Cu_3O_{6+x}$ Single Crystals

P. Jaschke, M. Gangl, A. Erb, R. Hackl [1]

In the cuprates disorder reduces the superconducting transition temperature T_c and influences or even conceals intrinsic electronic properties. Only $YBa_2Cu_3O_{6+x}$ (Y-123) can be prepared with stoichiometric cation composition and extremely high purity [1] in the wide carrier doping range $0 \leq p \leq 0.18$ corresponding to $0 \leq x \leq 1$. In this doping range, the interrelation of superconductivity and magnetism, the suppression of T_c near $p = 1/8$, [2] the pseudogap [3] or the onset point of superconductivity at $p \simeq 0.05$ can be studied. Doping can be adjusted with high precision by thermal treatment of the crystals in oxygen atmosphere. Oxygen content and order are equally important. For example, oxygen clusters are effective pinning centers. [4] Low-temperature annealing protocols improve the order substantially, [5, 6] and mean free paths ℓ as large as several microns can be obtained. [7] In this report we describe methods to prepare highly ordered samples having a well-defined carrier doping level p. We characterize the samples by susceptibility and Raman measurements and compare the results to those obtained from samples with a lower degree of order.

For a homogeneous oxygen content, the samples have to be annealed in an appropriate oxygen atmosphere and the correct pressure-temperature relationship has to be maintained during cool down. [8] To this end, a furnace with adjustable oxygen partial pressure was built. For a doping level of $x = 0.7$ we anneal the samples at 550 C and 16.4 mbar O_2 for at least 2 days and then slowly cool down to 300 C during one day. From there we can quench the samples without changing the oxygen content in the surface layer by too much due to the slow oxygen kinetics. After the annealing procedure the samples show only one single or very few rather smooth transitions to the superconducting state. This is already a sign of a highly homogeneous oxygen distribution.

The homogeneity of the oxygen can be improved further. First, the crystals are being detwinned in order to reduce strain in the lattice. For the next step, the equilibration, we seal the crystals in an evacuated quartz vial along with sinter material of the same oxygen content. Quartz cylinders fill the dead volume, and gold disks shield the samples from thermal radiation during the melt-off process. The single crystals are placed in voids of sintered cylinders to preserve the high surface quality. The vial is kept at $350 - 450$ C for at least 5 days. Because of the much bigger mass most of the oxygen originates from the sinter. In this way we achieve an oxygen partial pressure in the vial that is very close to the equilibrium conditions of the crystal at all temperatures. Possible contaminations are adsorbed by the sintered grains having a much larger surface than the crystal. For cooling down, the vial is quenched in water. During this step temperature gradients are unavoidable particularly in thick samples and may reintroduce twin boundaries. Further experiments are needed to increase the yield of twin free material. Finally, the crystals are annealed at room temperature for at least a week to arrange the oxygen chains in the right sequence. At $x = 0.7$ this is a series of two full and one empty chain (orthorhombic OIII phase) (see inset of Fig. 2).

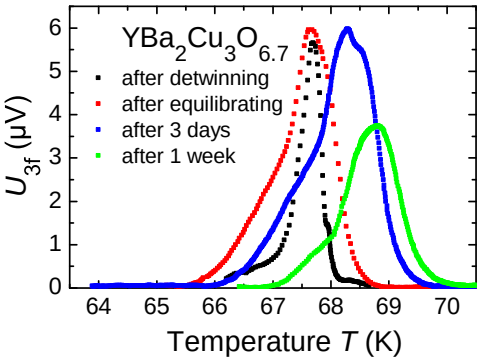

Figure 1: Non-linear susceptibility of the $YBa_2Cu_3O_{6.7}$ after the subsequent annealing steps. The signal is recorded at three times the excitation frequency f.

[1] Funding by the DFG via the Collaborative Research Center TRR 80 and the Priority Program SPP 1458, grant-no. Ha2071/7, is gratefully acknowledged.

In Fig. 1, we show susceptibility measurements performed after subsequent preparation steps. The signal at the third harmonic frequency $3f$ of the excitation turns out to be particularly sensitive to inhomogeneities. [9] After detwinning, the susceptibility shows multiple transitions manifesting themselves as narrow peaks. The small width originates from pinning due to oxygen disorder. After equilibration, T_c rises and the peak in the non-linear susceptibility broadens. This indicates a reduction of pinning and an increased homogeneity. Yet, to finally determine the distribution of oxygen and the correlation lengths of the highly ordered OIII domains x-ray diffraction experiments have to be performed.

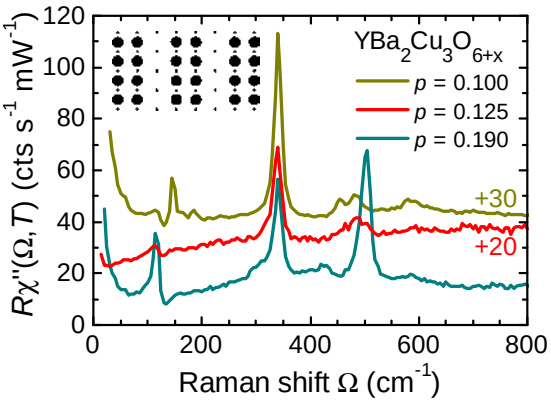

Figure 2: Raman response of the $YBa_2Cu_3O_{6+x}$. The oxygen content of the three samples is $x = 0.5$, 0.7, and 0.98 corresponding to $p = 0.10$, 0.125, and 0.19, respectively. The spectra of the underdoped samples are shifted as indicated. The inset shows schematically the optimal chain ordering of the $O_{6.7}$ sample (OIII phase). The spectra of the samples with $p = 0.10$ and 0.19 were measured by M. Opel (private communication).

To get insight into intrinsic electronic properties we started Raman scattering experiments on the highly ordered Y-123 sample as shown in Fig. 2. Until now, there are no systematic studies monitoring the various annealing steps, and we can compare the results only to well ordered samples having $x \simeq 0.5$ ($p \simeq 0.10$) and $x \simeq 0.98$ ($p \simeq 0.18$) measured by Opel *et al.* [10]. The yy-polarized spectra (incoming and scattered photons parallel to the crystallographic b-axis) measured at the three doping levels have phonon-related modes at approximately 120, 180, 340, 470-505, and 580-600 cm^{-1}. The latter feature appears only in the presence of defects in the chains. The absence of this vibration in the sample with $p = 0.125$ directly indicates highly ordered chains. Indirectly, high order manifests itself also in the phonon line at 340 cm^{-1}. The asymmetry of the this mode originates from electron-phonon coupling (Fano effect). Upon doping the van Hove singularity of the band structure approaches the Fermi energy. The resulting increase of the density of states N_F enhances the coupling λ. [10] In samples with disorder the doping becomes inhomogeneous and the effect becomes next to invisible. Although superconductivity-induced features in the electronic spectra could not be identified yet because of the reduced surface quality there are clear indications of a highly ordered phase at $p = 0.125$.

References

[1] A. Erb, E. Walker, and R. Flükiger, Physica C **245**, 245 (1995).
[2] R. Liang, D. A. Bonn, and W. N. Hardy, Phys. Rev. B **73**, 180505 (2006).
[3] T. Timusk, and B. Statt, Rep. Prog. Phys. **62**, 61 (1999).
[4] A. Erb, J.-Y. Genoud, F. Marti, M. Däumling, E. Walker, and R. Flükiger, J. Low Temp. Phys. **105**, 1023 (1996).
[5] R. Liang, D. A. Bonn, and W. N. Hardy, Physica C **336**, 57 (2000).
[6] R. Liang, D. A. Bonn, W. N. Hardy, J. C. Wynn, K. A. Moler, L. Lu, S. Larochelle, L. Zhou, M. Greven, L. Lurio, and S. G. J. Mochrie, Physica C **383**, 1 (2002).
[7] R. Harris, P. J. Turner, S. Kamal, A. R. Hosseini, P. Dosanjh, G. K. Mullins, J. S. Bobowski, C. P. Bidinosti, D. M. Broun, R. Liang, W. N. Hardy, and D. A. Bonn, Phys. Rev. B **74**, 104508 (2006).
[8] T. B. Lindemer, J. F. Hunley, J. E. Gates, A. L. S. Jr., J. Brynestad, C. R. Hubbard, and P. K. Gallagher, J. Am. Ceram. Soc **72**, 1775 (1989).
[9] F. Venturini. *Raman Scattering Study of Electronic Correlations in Cuprates: Observation of an Unconventional Metal-Insulator Transition*. Dissertation, Technische Universität München (2003).
[10] M. Opel, R. Hackl, T. P. Devereaux, A. Virosztek, A. Zawadowski, A. Erb, E. Walker, H. Berger, and L. Forró, Phys. Rev. B **60**, 9836–9844 (1999).

Epitaxial Yttrium-Iron-Garnet ($Y_3Fe_5O_{12}$) Thin Films

M. Althammer, M. Wagner, J. Lotze, H. Huebl, S. T. B. Goennenwein, M. Opel

Yttrium-iron-garnet, called *YIG*, is a synthetic garnet with the chemical composition $Y_3Fe_5O_{12}$. The five Fe^{3+} ions occupy two octahedrally and three tetrahedrally coordinated sites, with the Y^{3+} ions coordinated by eight oxygen ions in an irregular cube. The Fe^{3+} ions in the two coordination sites exhibit opposite spins, resulting in a ferrimagnetic behavior with a Curie temperature of 550 K. The material is insulating and shows an extremely low magnetization damping. This makes it an interesting material for high-frequency electronics, as magnetic excitations can propagate across the material on a length scale of several mm. Moreover, pure spin currents can be investigated without accompanying charge transport. Single crystalline YIG spheres exhibit excellent magneto-optical properties and extremely narrow linewidths of only 0.02 mT in ferromagnetic resonance (FMR) experiments at 3.3 GHz [1]. They are used in microwave resonators and network analyzers where their resonance frequency is tuned via external magnetic fields. Thick films are applied in magnetostatic wave devices, such as bandpass filters or phase shifters [2]. They are fabricated using liquid phase epitaxy which is incompatible with the standard fabrication and lithography processes in semiconductor electronics [3]. For the epitaxial growth of *thin* YIG films, pulsed laser deposition (PLD) has been successfully applied by several groups in recent years [3, 4]. Here, we report on the deposition as well as the structural and magnetic characterization of the first PLD-grown YIG thin films at the WMI.

The samples were fabricated in an ultra-high vacuum laser-MBE system on (111)-oriented $Gd_3Ga_5O_{12}$ (GGG) substrates, exhibiting a lattice mismatch of -0.057%. Epitaxial thin films of YIG were grown by PLD from a stoichiometric, polycrystalline target using an KrF excimer laser at 248 nm. The growth parameters were optimized with regard to the structural and magnetic properties of the thin films. Highest quality was obtained for a laser fluence of $2\,J/cm^2$, a substrate temperature of 550°C, and an O_2 atmosphere of 2.5×10^{-2} mbar.

The structural properties of the samples were investigated by high-resolution X-ray diffractometry (HR-XRD, Fig. 1). The ω-2θ scan in out-of-plane direction (111) for one representative sample with a thin film thickness of 43 nm does not display any secondary phases. On an enlarged scale around the GGG(444) reflection, satellites due to Laue oscillations are visible close to the main reflection (Fig. 1(a)) indicating coherent growth and low surface and interface roughness. The YIG(444) reflection itself, however, cannot be resolved unambiguously due to the small lattice mismatch between film and substrate. The left shoulder of the main reflection may be attributed to the YIG thin film. Rocking curves for the (444) reflection (not shown here) display a full width at half maximum of only 0.034°, evidencing a low mosaic spread.

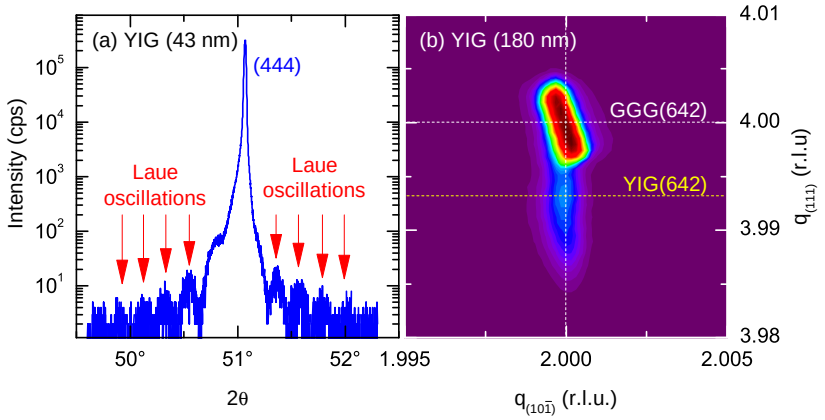

Figure 1: HR-XRD data from $Y_3Fe_5O_{12}$ (YIG) thin films deposited on (111)-oriented $Gd_3Ga_5O_{12}$ (GGG) substrates. (a) Out-of-plane ω-2θ-scan around the (444) reflection. (b) Reciprocal space map around the (642) reflection.

The reflection of the thin film can be better distinguished from that of the substrate in a reciprocal space map, as displayed for another representative sample with a thin film thickness of 180 nm in Fig. 1(b). For the in-plane $(10\bar{1})$ direction, the asymmetric (642) reflection from the YIG thin film is located at the same position as that of the substrate. This demonstrates the coherently strained growth of a (111)-oriented YIG thin film with the GGG in-plane lattice parameters.

The magnetostatic properties were studied by superconducting quantum interference device (SQUID) magnetometry at room temperature with the magnetic field applied in-plane (Fig. 2(a)). For the 43 nm thin film sample from Fig. 1(a), the magnetization M shows a ferrimagnetic behavior with a coercivity of 3 mT. The saturation magnetization is 125 kA/m, i.e. 88% of the bulk value of 142.65 kA/m. We attribute the deviation to uncertainties about the exact volume of the thin film as well as strain effects.

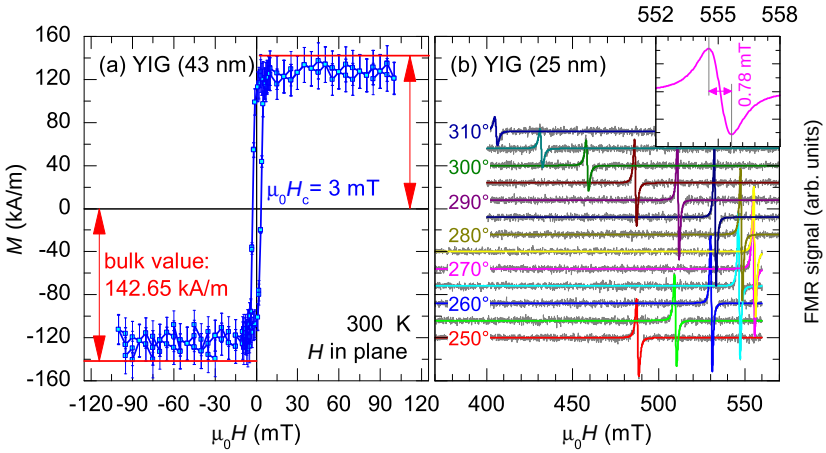

Figure 2: Room-temperature magnetic properties of $Y_3Fe_5O_{12}$ (YIG) thin films deposited on (111)-oriented $Gd_3Ga_5O_{12}$ (GGG) substrates. (a) Magnetization M versus magnetic field H applied in-plane for a 43 nm thin film. The contribution from the paramagnetic substrate has been subtracted. The coercivity is 2.98 mT, the saturation magnetization almost reaches the bulk value of 142.65 kA/m. (b) FMR spectra (grey) and fit curves (color) from a 25 nm thin film for different angles between the magnetic field and the sample surface. The inset shows the FMR resonance in out-of-plane direction (270°). The peak-to-peak linewidth is $\mu_0 \Delta H_{pp} = 0.78$ mT.

The magnetization dynamics was investigated by ferromagnetic resonance (FMR) in the X band (10.3 GHz) at room temperature. In Fig. 2(b), typical FMR spectra from a 25 nm thin YIG film are shown for different angles between the magnetic field and the sample surface. The lowest linewidth is obtained in out-of-plane direction (270°) with $\mu_0 \Delta H_{pp} = 0.78$ mT (inset in Fig. 2(b)). This still significantly exceeds the value of 0.02 mT which was reported for polished spheres [1]. However, the latter value was obtained at 3.33 GHz and should therefore be multiplied by 3.1 for better comparison. With regard to PLD-grown thin films, our ΔH_{pp} values are still one order of magnitude larger than those reported by other groups [2].

In forthcoming experiments, we will systematically investigate the influence of the thin film thickness and the surface roughness on the magnetic properties. Moreover, we will study a possible effect of post-annealing in oxygen atmosphere which is reported to enhance the overall properties of PLD-grown YIG thin films on GGG substrates, in particular regarding magnetic damping [2].

References

[1] C. Kittel. *Einführung in die Festkörperphysik*, p. 550 (R. Oldenbourg Verlag GmbH München, 1991), 9 edn.
[2] S. A. Manuilov, S. I. Khartsev, and A. M. Grishin, J. Appl. Phys. **106**, 123917 (2009).
[3] S. A. Manuilov, R. Fors, S. I. Khartsev, and A. M. Grishin, J. Appl. Phys. **105**, 033917 (2009).
[4] Y. Krockenberger, K.-S. Yun, T. Hatano, S. Arisawa, M. Kawasaki, and Y. Tokura, J. Appl. Phys. **106**, 123911 (2009).

Growth and Characterization of High-Purity $CaWO_4$ Scintillating Single Crystals for the Low-Temperature Direct Dark Matter Search Experiments CRESST-II and EURECA

Andreas Erb
Jean-Côme Lanfranchi [1,2]

Introduction. One of the great scientific enigmas remaining today is the nature and direct detection of Dark Matter. According to astrophysical and cosmological observations the Universe contains ∼4% of baryonic matter, ∼23% of Dark Matter and ∼73% of Dark Energy. The impact of non-luminous matter up to now can only be observed indirectly via gravitational effects, e.g. by measuring the anomaly of rotation curves of galaxies and galaxy clusters. At present the influence of Dark Matter can be seen on all scales in the Universe leaving its imprint not only in the Cosmic Microwave Background (CMB), but also in the large scale structure formation as we observe it today. A well motivated candidate to account for the "missing" matter is the Weakly Interacting Massive Particle (WIMP) of which the mass range could span between 10 to 1000 GeV/c^2 with interaction cross sections with baryonic matter as low as 10^{-47}cm^2. The direct search for these particles is part of the activities at the Cluster of Excellence "Origin and Structure of the Universe" since 2007. One of the experiments in this context is the CRESST-II experiment (Cryogenic Rare Event Search with Superconducting Thermometers) located deeply underground in the Laboratori Nazionali del Gran Sasso (LNGS) in Italy.

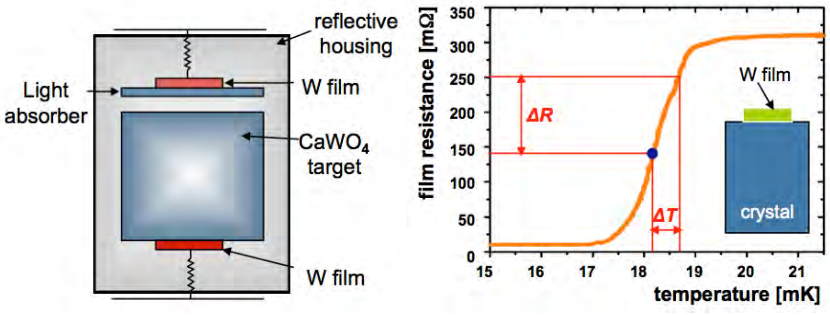

Figure 1: (Left panel) Working principle of a CRESST-II detector module consisting of two individual low-temperature detectors housed in a reflective and scintillating cavity: a scintillating $CaWO_4$ target crystal (∼300g) equipped with an α-tungsten transition edge sensor (TES,$T_c \approx$ 10mK) detects the energy produced by a particle (e.g. WIMP) interaction; a silicon on sapphire (SOS) or pure silicon light detector also equipped with an α-tungsten TES detects the associated scintillation light produced by an interaction in the $CaWO_4$ crystal. (Right panel) Working principle of a TES: the TES is stabilized in its transition region between the normal- and superconducting state; a change in temperature due to an energy deposition is translated into a change in resistance, which is read out by a dedicated SQUID circuit.

CRESST-II consists of a ^{3}He/^{4}He-dilution refrigerator which extends via an ultra-pure copper cold-finger into an extremely well shielded volume. With several tons of polyethylene, lead, copper and an active muon veto an ultra-low background environment is achieved. Here, a total of 33 detector modules (i.e. ∼10 kg of active target mass) can be operated at ∼10mK. The CRESST-II detector modules consist of two individual low-temperature detectors: a scintillating $CaWO_4$ single crystal target (∼300g) equipped with an α-tungsten transition edge sensor (TES, $T_c \approx$ 10mK) detects the energy produced by a particle (e.g. WIMP) interaction; a second silicon on sapphire (SOS) or pure silicon light detector also

[1]Chair E15, Physics Department TU Munich, Germany.
[2]Cluster of Excellence for Fundamental Physics: Origin and Structure of the Universe.

equipped with an α-tungsten TES detects the associated scintillation light produced by an interaction in the $CaWO_4$ crystal. WIMPs are expected to produce nuclear recoils, whereas gammas and electrons induce electron recoils. The simultaneous measurement of both quantities (heat and scintillation) is the prerequisite to achieve a highly efficient background suppression on an event-by-event basis to disentangle various types of events in the crystal. The peculiarity of CRESST-II is the use of a multi-material target for WIMPs ($CaWO_4$), i.e. it is presently the only direct Dark Matter search experiment with the ability to probe several WIMP-mass scenarios in the same setup. In addition, CRESST-II is also unique with respect to its high sensitivity to "light"-WIMPs ($\sim$10-30 GeV/c^2). For further reading we recommend [1, 2] and references therein.

Crystal Growth of $CaWO_4$. $CaWO_4$ is a natural mineral also known as scheelite, which is relatively abundant in nature and actually the main source for the metal tungsten. Despite its relative abundance in nature it is not easily grown as a high purity single crystal. High-purity scintillating single crystals, however, are the prerequisite for the use as a particle detector for WIMPs where radio-purity is a crucial issue due to the low count-rate expected for WIMPS ($\leq$0.1cts/kg/d). Despite the fact that $CaWO_4$ is a congruently melting compound it exhibits several challenges concerning its growth. First, it has a high melting temperature of $\sim$ 1600°C, secondly, it is an oxide, with the consequence that for clear and transparent crystals the growth needs to be performed in the presence of oxygen in the growth atmosphere. From the purity point of view a containerless crystal growth method would be highly beneficial for the production of the detector crystals, however, $CaWO_4$ in its high-purity form is transparent to IR- and visible light hampering the use of optical furnaces. Since it is also insulating the floating zone method with direct inductive heating cannot be applied. Due to its extreme proneness to cleaving in the presence of temperature gradients the use of the Verneuil technique is impossible as well. Thus, for massive bulk crystals with several hundreds of grams in weight a crystal growth method with a crucible involved, e.g. the Bridgeman or a the Czochralski technique needs to be applied. $CaWO_4$ being an oxide with a melting point of 1600 °C, and an at least partially oxidative atmosphere the possible choice of crucible materials is restricted and the choice lies basically amongst metals of the platinum group. We have chosen rhodium because of its high chemical inertness and resistance against oxygen compared to platinum and iridium, even though rhodium is the most expensive metal in the platinum group.

Figure 2: $CaWO_4$ crystal of 886 g with seed holder and seed after growth. The slightly grey colour of the crystal is due to an oxygen deficiency originating from the low oxygen partial pressure in the growth atmosphere. The grey colour can be removed by a subsequent annealing procedure in pure oxygen at elevated temperatures.

Czochralski Growth of $CaWO_4$ At present the detectors used for the CRESST-II experiment are of cylindrical shape with 40 mm in diameter and 40 mm in height and with a mass of about 300 g, which means that the grown ingots need to be at least 44 mm in diameter regarding the cylindrical part of the crystal. For the growth of such crystals we use a pure rhodium

crucible of 750 g with an inner diameter of 80 mm and 80 mm in height which can hold about 1.6 kg of molten $CaWO_4$. Since $CaWO_4$ has a tetragonal structure with a pronounced cleavage plane perpendicular to the 001 direction and birefringence we use c-oriented seeds to grow the crystals along c-direction. Czochralski growth is performed in a high frequency heated commercial furnace (Cyberstar Grenoble, Oxypuller 20-04) equipped with an active after-heater to overcome the cleavage problem due to temperature gradients or rapid cooling.

The high frequency operates at ∼7 kHz and heats the crucible directly by induction. The pulling head of the furnace is equipped with a precision balance, capable of measuring the crystal's weight up to ∼8.2 kg with a resolution of 1 mg. The crystal shape can be "designed" prior to crystal growth and the theoretical weight gain of the constructed crystal can be compared with the measured weight gain of the growing crystal. The deviation of these 2 values is used to regulate the power of the high frequency generator, which in turn determines the diameter of the isotherms in the melt and thus the crystal diameter. By optimizing the growth parameters we were able to grow crystals up to 47 mm in diameter with a total mass up to 880 g in a 80 mm crucible and, in a bigger setup, up to 57 mm in diameter exhibiting a total mass of ∼1.6 kg in a 120 mm crucible. Crystal growth was performed in low oxygen partial pressure of 10 mbar to avoid the formation of a volatile rhodium oxide.

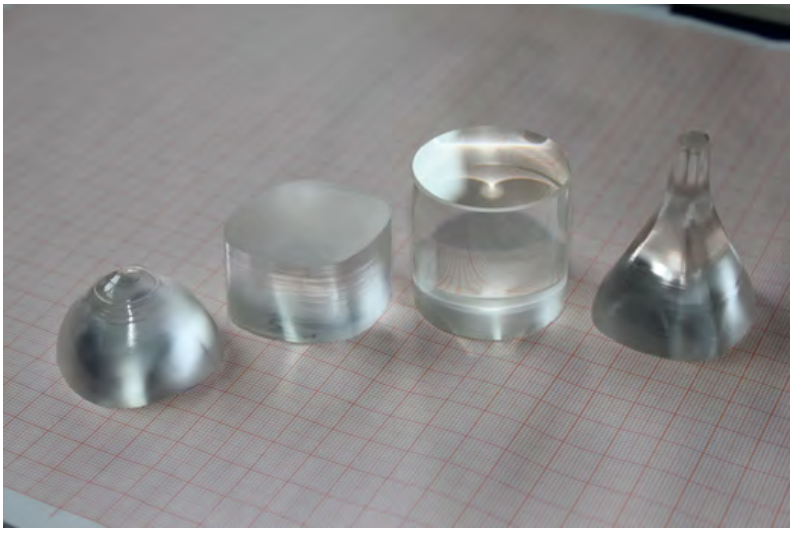

Figure 3: Cut and polished pieces of the $CaWO_4$ crystal; from left to right : tail, residual cylinder, detector crystal, shoulder and neck

Oxygenation and $CaWO_4$ Detector Preparation. The growth of the crystals in reduced oxygen partial pressure leads -depending on the diameter and growth velocity of the produced crystal- to a slightly greyish colour. Due to an oxygen deficiency this behaviour becomes even more pronounced for crystals exceeding a diameter of 20 mm. Since a high light yield of the crystal is crucial prerequisite for the background suppression in the CRESST-II experiment, the crystals need to be oxygenated after growth to make them as transparent as possible for the scintillation light. We optimize the clarity of the crystals by oxygenating them after growth in pure oxygen at temperatures between $1100 - 1500$ °C followed by slow cooling at rates of 50-100 K/h to room temperature. This not only leads to clear crystals but also releases residual strain prior to the cutting and polishing procedure, thus reducing the risk of cleaving in the final steps of the production of detector crystals. The analysis of radio-purity aspects, as well as the optimization of the light yield with respect to different crystal geometries and oxygenation treatment is subject of an ongoing Ph.D. thesis [3].

Conclusion and Outlook. In conclusion we have set up a dedicated production facility to grow scintillating single crystals of $CaWO_4$ suitable in quality and purity for the implementation into the direct Dark Matter search experiment CRESST-II. We have now excellent control

of both the crystal purity due to direct contact with the experimental group building and characterizing the detectors and direct feedback regarding the crystal production parameters. Moreover, the setup of an in-house crystal production now provides us with a reliable source for such high purity crystals, which has been a severe problem in the past. This development not only is important for the already running CRESST-II experiment with a projected total detector mass of about 10-30kg but will be the most important prerequisite for the participation in the future EURECA (European Underground Rare Event Calorimeter Array) experiment with a projected total detector mass of 1000 kg comprising up to 500 kg of $CaWO_4$.

References

[1] G. Angloher et al. (CRESST collaboration), Astropart. Phys. **31**, 270 (2009).
[2] G. Angloher et al. (CRESST Collaboration), submitted to Europ. Phys. J. C, arXiv:1109.0702v1 (2011).
[3] M. v. Sivers. *Opitimizing the Light Yield of CaWO4 Single Crystals for Direct Dark Matter Detection*. Ph.D. Thesis, in preparation, TU Munich.

Experimental Facilities

Millikelvin Temperatures in Combination with 3D Vector Magnetic-Fields
Now Available in the WMI Quantum Science Laboratory

H. Huebl, A. Marx, K. Uhlig, S.T.B. Goennenwein, and R. Gross [1]

Last year, we reported on the construction of Quantum Science Laboratory at the Walther-Meißner-Institute [1]. The construction was completed in early 2011. Simultaneously, in 2010 we successfully applied for a cryogen-free (or "dry") dilution refrigerator with a 3D vector magnet via the "State Major Instrumentation Programme".

Figure 1: Unpacking the dilution unit. The dilution unit hanging from the crane and still protected by the aluminium frame with is in the process to be removed.

In November 2011, the system was delivered and installed by Oxford Instruments. Figures 1-2 show several stages of the assembly and testing of the system. After unpacking of the components from the transport boxes, the system was partly assembled in the "Helium-Halle" and subsequently transported to the Quantum Laboratories. Figure 3 shows the assembled dilution insert with its temperature stages.

Figure 2: Completed setup. The dilution system with the 3D vector magnet is assembled in the new Quantum Laboratories and operating at base-temperature.

Windows in the thermal shields allow direct access to all temperature stages, easing the installation of additional high frequency equipment like cold-amplifiers, circulators and attenuators. Finally, the system was tested and the system specifications were verified successfully. Currently, we are working to equip the system with additional low-temperature high frequency components to enable microwave spectroscopy at the single photon level at millikelvin temperatures.

Scientifically, several directions in the field of fundamental light matter interaction are envisaged with this setup:

(i) Experiments in the field of circuit quantum electrodynamics (circuit QED), where superconducting qubits form hybrids with microwave resonators. These experiments are time consuming because quantum effects arise in the limit of low excitation numbers. Hereby, challenging requirements are imposed on the detection systems allowing to detect microwave signals in the atto-Watt regime. [2]

[1] We greatfully acknowledge funding via the "State Major Instrumentation Programme".

(ii) Following this direction, the storage of quantum states is an important aspect. One pathway in this direction is transfer the quantum information contained in photons onto long-lived spin states [3–7]. This regarding, phosphorus dopants in Silicon are an optimal candidate due to their long coherence times [8], however strong coupling of such a phosphorus spin ensemble to a superconducting microwave resonator has not been demonstrated up to now. We intend to study the light-matter interaction with long-lived spin systems and integrate superconducting quantum circuits.

(iii) Spin systems are an interesting topic per-se and relaxation or damping is one of their key parameters. Here, the investigations are not limited to paramagnetic spin systems, but will be extended to exchange coupled (ferro-) magnetic systems. The new setup is designed for broadband microwave spectroscopy up to 18 GHz in the temperature range between 30 K and 20 mK while applying a 3D-vector magnetic field up to 1 T or an unidirectional magnetic field of 6 T. Hereby, magnetization damping can be investigated as function of the temperature, frequency and magnetic field direction.

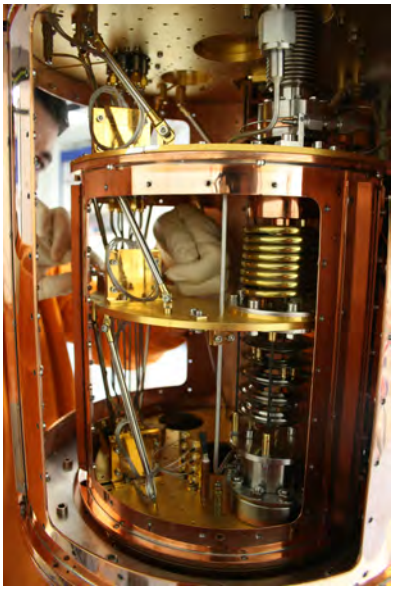

Figure 3: Inside of the dilution system. The windows of the 4 K and the still-shield are removed allowing to access to the low-temperature stages.

Last but not least, we want to acknowledge all members of WMI who helped preparing the new Quantum Science Laboratory for the installation of low-temperature quantum experiments and setting up this particular setup.

References

[1] H. Huebl, L. Ossiander, T. Brenninger, A. Marx, and R. Gross. Ann. Rep. WMI, p.83; www.wmi.badw.de/publications/jahresberichte/2010.pdf (2010).
[2] E. P. Menzel, F. Deppe, M. Mariantoni, M. A. Araque Caballero, A. Baust, T. Niemczyk, E. Hoffmann, A. Marx, E. Solano, and R. Gross, Phys. Rev. Lett. **105**, 100401 (2010).
[3] Y. Kubo, F. R. Ong, P. Bertet, D. Vion, V. Jacques, D. Zheng, A. Dreau, J. F. Roch, A. Auffeves, F. Jelezko, J. Wrachtrup, M. F. Barthe, P. Bergonzo, and D. Esteve, Phys. Rev. Lett. **105**, 140502 (2010).
[4] D. I. Schuster, A. P. Sears, E. Ginossar, L. DiCarlo, L. Frunzio, J. J. L. Morton, H. Wu, G. A. D. Briggs, B. B. Buckley, D. D. Awschalom, and R. J. Schoelkopf, Phys. Rev. Lett. **105**, 140501 (2010).
[5] R. Amsüss, C. Koller, T. Nöbauer, S. Putz, S. Rotter, K. Sandner, S. Schneider, M. Schramböck, G. Steinhauser, H. Ritsch, J. Schmiedmayer, and J. Majer, Phys. Rev. Lett. **107**, 060502 (2011).
[6] E. Abe, H. Wu, A. Ardavan, and J. J. L. Morton, Appl. Phys. Lett. **98**, 251108 (2011).
[7] J. H. Wesenberg, A. Ardavan, G. A. D. Briggs, J. J. L. Morton, R. J. Schoelkopf, D. I. Schuster, and K. Mølmer, Phys. Rev. Lett. **103**, 070502 (2009).
[8] A. M. Tyryshkin, S. A. Lyon, A. V. Astashkin, and A. M. Raitsimring, Phys. Rev. B **68**, 193207 (2003).

New WMI Millikelvin Facilities for Experiments with Superconducting Quantum Circuits

F. Deppe, A. Marx, J. Höß, K. Neumaier, C. Probst, K. Uhlig, R. Gross [1]

Since the first experiments on coherent oscillations in macroscopic quantum systems [1] in 1999, superconducting quantum circuits imprinted on a substrate chip have evolved into a prospering field in solid-state physics. In the following years, several types of Josephson junction based superconducting quantum bits (qubits) [2] were developed, mainly with prospective scalable quantum information processing (QIP) applications in mind. Very soon, also quantum simulation was proposed because the quantum coherence requirements for full-scale QIP seemed, despite a lot of progress, hard to reach with superconducting qubits. In a hallmark experiment in 2004 [3], the nonlinear qubits were coupled to linear superconducting circuits, giving birth to the field of circuit quantum electrodynamics (QED) [4]. Here, in analogy to quantum optical cavity QED [5], the qubits act as single artificial two-level atoms, which are coupled with unprecedented interaction strengths to quantum light stored in transmission line resonators. In this way, the motivation for investigating superconducting quantum circuits was extended from pure QIP to general studies on quantum mechanics. In this spirit, again inspired by quantum optics but considering that superconducting quantum circuits have typical transition frequencies of a few gigahertz, very recently propagating quantum microwaves have moved into the focus of the superconducting quantum circuits community. Here, in addition to fundamental light matter coupling and QIP or quantum simulation applications, the quantum state reconstruction is an important and challenging topic.

The research on superconducting quantum circuits at the WMI focuses mainly on systems sensitive to externally applied flux. Our central workhorse is certainly the superconducting flux qubit [6–8], where we recently implemented an especially tunable version (Ref. [9] and pp. 51–53). Furthermore, we built circuit QED systems by coupling flux qubits to transmission line resonators [10]. We used these systems to study operating point dependent selection rules (cf. pp. 36–38) and to demonstrate novel light-matter interaction physics with coupling strengths far beyond the limits found for single natural atoms ("ultrastrong coupling" [8, 11]). In addition, we have recently shown vacuum squeezing in a flux driven Josephson parametric amplifier (JPA) (cf. pp. 39–41). Our work on propagating quantum microwaves so far comprised the development and characterization of a quantum state reconstruction method allowing for the absence of off-the-shelf efficient microwave photodetectors [12–14]. Along these lines, we also characterized microwave beam splitters (Ref. [15] and pp. 54–55) and coupled transmission line resonators (cf. pp. 56–58), finding promising properties for using these systems in experiments on quantum correlations.

In order to keep up and further develop the above mentioned activities on quantum effects in the microwave regime, cryogenic capacities at millikelvin temperatures ($5\,\mathrm{GHz} \sim 240\,\mathrm{mK}$) are required. In addition to large cooling powers, the specifications for these cryostats are mainly dictated by the dimensions (typically a few centimeters in each direction) of bulky microwave components such as circulators or microwave switches. Under the scientific supervision of F. Deppe and A. Marx with indispensable support from our technical staff, the doctoral students, and our experienced cryogenic experts (K. Neumaier, C. Probst, and K. Uhlig), the following steps have been taken:

[1] We acknowledge financial support from the German Research Foundation via SFB 631, the German Excellence Initiative via NIM, and the EU Marie Curie Initial Training Network CCQED.

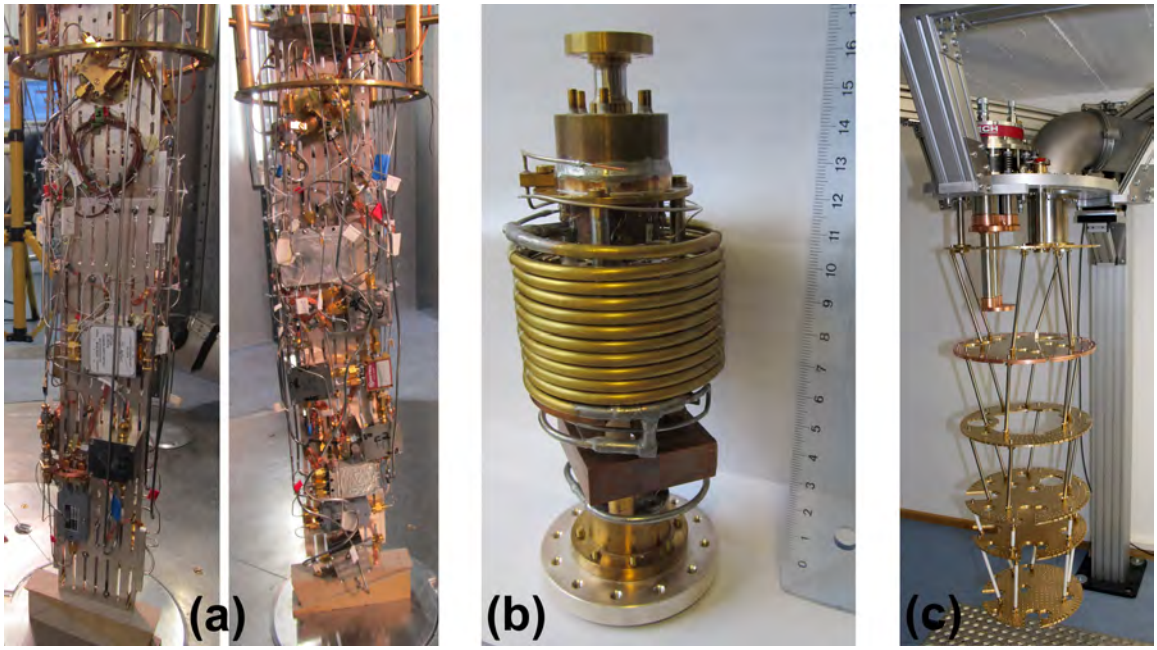

Figure 1: Activities towards increased millikelvin capacities in the Superconducting Quantum Circuits Group. **(a)** Sample stage of K12-fridge equipped with four circuit QED experiments. Left: Back side. Right: Front side. The height of the silver rod is 50 cm. **(b)** Dilution unit of the liquid helium precooled dilution refrigerator currently being set up in laboratory K04. **(c)** Current construction stage of the dry dilution refrigerator currently being set up in laboratory K21. The dimension of the lowest plate is approximately 35 cm.

- The sample space of the liquid helium precooled dilution refrigerator in laboratory K12 has been extended from a cylindrical volume with 11 cm diameter and 15 cm height to one with 55 cm height. By further increasing the number of microwave amplifiers at the 4 K-stage from two to four, the number of broadband input lines from four to seven, and the number of twisted pair DC-lines from 32 to 80, we are now in a position to mount four experiments simultaneously and avoid idle times by interleaved measurements [see Fig. 1(a)]. The fridge has been successfully cooled to 20 mK base temperature end of October and first measurements on the dielectric losses of superconducting microstrip resonators at very low temperatures are currently performed.

- In addition, we are currently setting up a similar facility in laboratory K04. Here, the key components such as the gas handing system, pumps and vacuum installations, cryogenic insert, and the dilution unit [see Fig. 1(b)] are finished, so we expect a first test cooldown early next year.

- For our mid- and longterm goal to scale our experiments towards quantum simulation and quantum information processing systems, we have recently started setting up a dry dilution refrigerator, where all temperature stages have a diameter of approximately 30-40 cm [see Fig. 1(c)].

In summary, the Superconducting Quantum Circuits Group at the WMI is very active in setting up millikevin measurement capacities with large sample spaces in order perform our key experiments on ultrastrong light-matter interaction and propagating quantum microwaves. Our efforts aim at creating sufficient cryogenic capabilities enabling us to follow our roadmap towards ultrafast quantum gates and quantum information processing with propagating microwave photons.

References

[1] Y. Nakamura, Yu. A. Pashkin, and J. S. Tsai, Nature **398**, 786–788 (1999).
[2] J. Clarke, and F. K. Wilhelm, Nature **453**, 1031–1042 (2008).
[3] A. Wallraff, D. I. Schuster, A. Blais, L. Frunzio, R.-S. Huang, J. Majer, S. Kumar, S. M. Girvin, and R. J. Schoelkopf, Nature **431**, 162–167 (2004).
[4] R. J. Schoelkopf, and S. M. Girvin, Nature **451**, 664–669 (2008).
[5] H. Mabuchi, and A. C. Doherty, Science **298**, 1372–1377 (2002).
[6] F. Deppe, M. Mariantoni, E. P. Menzel, S. Saito, K. Kakuyanagi, H. Tanaka, T. Meno, K. Semba, H. Takayanagi, and R. Gross, Phys. Rev. B **76**, 214503 (2007).
[7] T. Niemczyk, F. Deppe, M. Mariantoni, E. Menzel, E. Hoffmann, G. Wild, L. Eggenstein, A. Marx, and R. Gross, Supercond. Sci. Technol. **22**, 034009 (2009).
[8] T. Niemczyk, F. Deppe, H. Huebl, E. P. Menzel, F. Hocke, M. J. Schwarz, J. J. Garcia-Ripoll, D. Zueco, T. Hümmer, E. Solano, A. Marx, and R. Gross, Nature Phys. **6**, 772–776 (2010).
[9] M. J. Schwarz, T. Niemczyk, G. Wild, F. Deppe, A. Marx, and R. Gross. In **Annual Report 2009** 38–40 (Walther-Meißner-Institut für Tieftemperaturforschung, Garching, 2009).
[10] F. Deppe, T. Niemczyk, E. P. Menzel, A. Marx, and R. Gross. In **Annual Report 2010** 29–31 (Walther-Meißner-Institut für Tieftemperaturforschung, Garching, 2010).
[11] T. Niemczyk, F. Deppe, H. Huebl, E. Menzel, M. Schwarz, F. Hocke, E. Hoffmann, A. Marx, R. Gross, J. Garcia-Ripoll, D. Zueco, T. Hümmer, and E. Solano. In **Annual Report 2010** 36–39 (Walther-Meißner-Institut für Tieftemperaturforschung, Garching, 2010).
[12] E. P. Menzel, F. Deppe, M. Mariantoni, A. Baust, M. A. A. Caballero, E. Hoffmann, T. Niemczyk, C. Probst, K. Neumaier, K. Uhlig, A. Marx, E. Solano, and R. Gross. In **Annual Report 2010** 32–33 (Walther-Meißner-Institut für Tieftemperaturforschung, Garching, 2010).
[13] E. P. Menzel, M. Mariantoni, F. Deppe, M. Á. A. Caballero, A. Baust, T. Niemczyk, E. Hoffmann, A. Marx, E. Solano, and R. Gross, Phys. Rev. Lett. **105**, 100401 (2010).
[14] M. Mariantoni, E. P. Menzel, F. Deppe, M. Á. A. Caballero, A. Baust, T. Niemczyk, E. Hoffmann, E. Solano, A. Marx, and R. Gross, Phys. Rev. Lett. **105**, 133601 (2010).
[15] E. Hoffmann, F. Deppe, T. Niemczyk, T. Wirth, E. P. Menzel, G. Wild, H. Huebl, M. Mariantoni, T. Weißl, A. Lukashenko, A. P. Zhuravel, A. V. Ustinov, A. Marx, and R. Gross, Appl. Phys. Lett. **97**, 222508 (2010).

A Setup for Tip-Enhanced Raman Spectroscopy (TERS)

F. Kretzschmar, B. Botka, N. Chelwani, D. Hoch, R. Hackl [1]

Compounds with correlated electrons show a large variety of phenomena such as metal-insulator transitions, spin and charge order or superconductivity. The interplay of lattice, spin, charge, magnetization, and electric polarization leads to rich phase diagrams and makes correlated electron systems very interesting for science and promising for applications. Yet it is rather complicated to pin down how charges, spins, and the lattice reconstruct around defects or at interfaces. Although being a powerful experimental tool in general, [1] conventional electronic Raman scattering (ERS) experiments cannot be used to study structures much smaller than the wavelength of light λ. Only recently, near field methods have been shown to overcome these restrictions [2, 3].

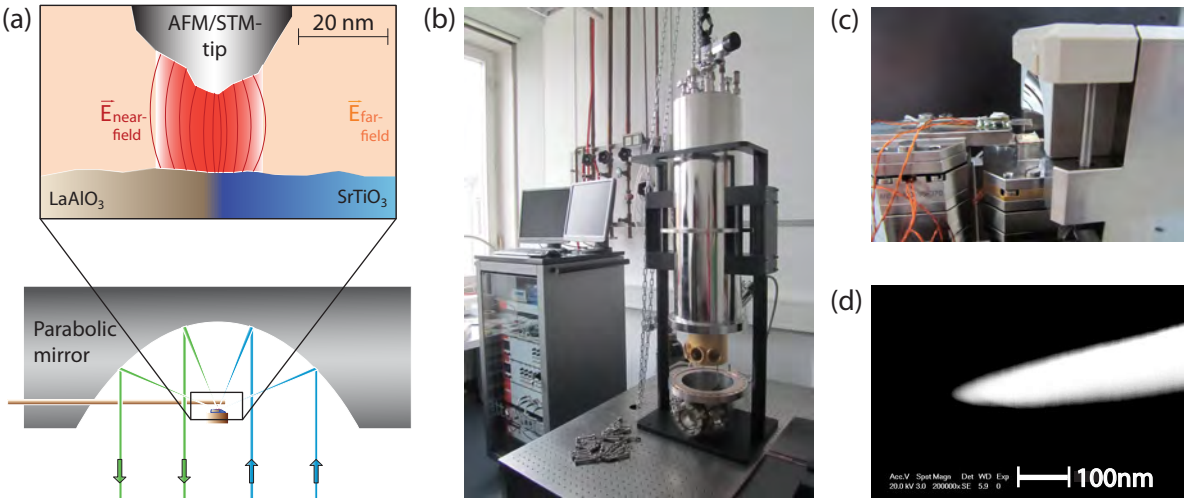

Figure 1: (a) Top-illumination principle using a parabolic mirror. (b) UHV Cryostat with optical access. The microscope is hidden behind the golden plated radiation shield. (c) Piezo stage, tuning fork and AFM/STM tunneling tip, with the apex positioned in the parabolic mirror's focus. (d) Electrochemically etched gold tip. The tip-apex has a radius of less than 25 nm.

Tip-enhanced Raman spectroscopy (TERS) provides the possibility to investigate surfaces of solid state samples with a spatial resolution in the range of 15 nm [4]. The crucial feature of a TERS setup is an ultrasharp metallic tip which simultaneously acts as the tip of a scanning tunneling or atomic force microscope (STM/AFM) device and as an external amplifier of the Raman signal. By focusing a laser beam onto the metal tip, a surface plasmon is excited locally which leads to a field enhancement at distances on the order of the tip radius. All optical processes are enhanced by a correspondingly increased excitation rate. Additionally, the tip acts as an antenna and amplifies the field of scattered light. The overall enhancement for light scattering signals coming from the near-field region can be as high as six orders of magnitude [2] and theoretical predictions yield a total Raman enhancement of more than 10^{14} [5]. A strong enhancement effect is essential for the contrast between near-field and far-field signal, especially regarding bulk samples, where the scattering volume of the far-field signal is substantially larger than that of a thin film. A test experiment with Si showed that the tip-enhanced scattering intensity is up to twice as high as in a conventional macro-Raman

[1]This work is supported by the German Research Foundation (DFG) via the Collaborative Research Center TRR 80 and by the EC's 7th Framework Programme via Marie Curie Initial Training Networks under grant agreement no. PITN-GA-2008-215399 (FINELUMEN).

experiment [5]. This not only means that TERS provides sufficient contrast for bulk *versus* surface measurements but can also be used for materials with low scattering cross sections like metallic systems.

Given these encouraging prospects we started to build a TERS setup. Fig. 1(a) shows the optical concept of our system. We use top-illumination with a parabolic mirror which provides a high numerical aperture (NA = 1) and a correspondingly small focal volume of the laser beam. Consequently, scattered light arises from an ideally localized area and is converted to a nearly perfect parallel beam of scattered light. Moreover, due to the high numerical aperture of the parabolic mirror the solid angle from which scattered light is collected is significantly larger than that of other optical devices.

So far, TERS has not been used for the study of solids at low temperature. In our setup, the scanning unit and the parabolic mirror are located in a UHV cryostat with optical access [see Fig. 1(b)] which faciliates near-field Raman experiments at temperatures in the range of 10 K and at 10^{-8} mbar. Since the parabolic mirror inside the vacuum chamber has a fixed position, the tip and the sample must be electronically adjustable in order to align the tip apex and the laser focus for the maximal enhancement effect. Therefore sample and tip are mounted on independent piezo-controlled stages and can be moved in x, y, z direction with sub-Å accuracy. Since mechanical vibrations would reduce the spatial resolution, the whole optics (including laser illumination, scattering beam path and observation part) and the cryostat are mounted on the same optical table with active vibration isolation. In addition, one has to compensate the thermal expansion occurring in a cryogenic environment and to keep the parabola axis aligned with the optics outside the cryostat. For this purpose the cryostat can be vertically moved by a stepping motor with respect to the breadboard hosting the external optics with approximately 2 µm accuracy.

The precision of the external optics design is essential for the successful operation of the new device. Two criteria have to be considered in particular: (i) The laser beam for excitation must be exactly parallel to the optical axis of the parabolic mirror inside the cryostat, and (ii) the resolution and contrast of the observation optics have to be sufficiently high to control of the position of the laser focus on the tip apex. For the latter purpose we designed new imaging and illumination optics using the ray-tracing software Zemax. The optical design software enables us to appropriately deal with the abberations originating mainly from the parabolic mirror.

Finally, we built a setup for electrochemical etching of tunneling tips with reproducible geometry. A platinum ring and a gold wire with a diameter of 100 µm in the center of the ring are connected with the anode and the cathode, respectively, and are immersed in highly concentrated hydrochloric acid. The etching starts when a characteristic AC voltage is applied for a short time. With this method we reproducibly obtained tip radii of less than 25 nm as verified by scanning electron microsopy [see Fig. 1(d)].

References

[1] T. P. Devereaux, and R. Hackl, Rev. Mod. Phys. **79**, 175–233 (2007).
[2] B. Pettinger, B. Ren, G. Picardi, R. Schuster, and G. Ertl, J. Raman Spectrosc. **36**, 541–550 (2005).
[3] A. Hartschuh, E. J. Sánchez, X. S. Xie, and L. Novotny, Phys. Rev. Lett. **90**, 095503 (2003).
[4] J. Steidtner, and B. Pettinger, Phys. Rev. Lett. **100**, 236101 (2008).
[5] J. Steidtner, and B. Pettinger, Rev. Sci. Instrum. **78**, 103104 (2007).

Overview of Key Experimental Facilities and Infrastructure

In the following basic information on the key experimental facilities and components of the technical infrastructure installed at the Walther-Meißner-Institute (WMI) is given.

UHV-Laser-MBE

The WMI operates a UHV-Laser-Molecular Beam Epitaxy (L-MBE) system for the growth of complex oxide heterostructures. The system has been designed to meet the special requirements of oxide epitaxy. The UHV cluster tool consists of the following main components:

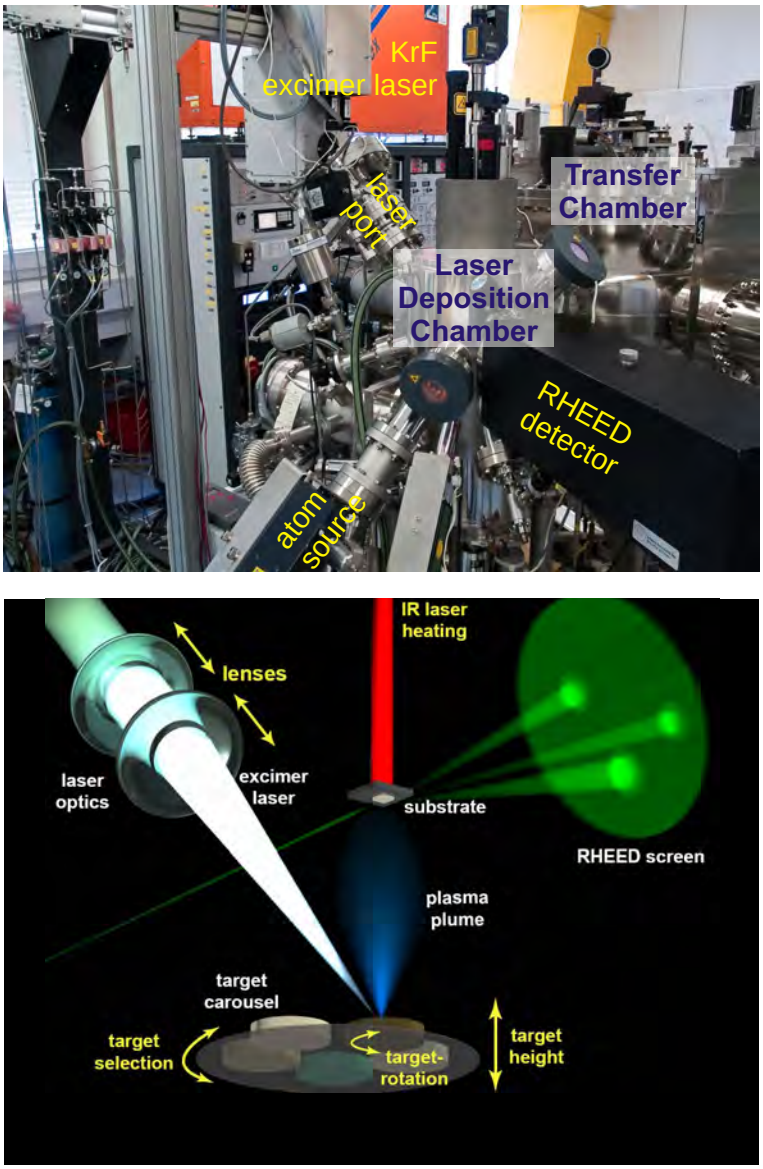

Figure 1: Top: UHV-Laser-Molecular Beam Epitaxy System. Bottom: Principle of the deposition process.

- central transfer chamber;
- load-lock chamber with heater system for substrate annealing;
- laser deposition chamber with in-situ reflection high energy electron diffraction (RHEED) system, laser substrate heating system, and atomic oxygen/nitrogen source, the RHEED system has been modified to allow for the operation at high oxygen partial pressure up to 0.5 mbar;
- surface characterization chamber with UHV scanning force microscope (Omicron);
- metallization chamber with a four heart electron gun system and a liquid nitrogen cooled sample stage. The sample holder can be tilt for shadow evaporation;
- KrF excimer laser.

The system is used for the growth of complex oxide heterostructures consisting of superconducting, magnetic, dielectric, and semiconducting materials such as the high-temperature superconductors, the doped manganites, the double perovskites, magnetite, zinc oxide, etc..

The original laser molecular beam epitaxy system (laser-MBE) designed already in 1995/96 until now has been permanently upgraded and modified. In particular, the substrate heating system and the temperature control unit was changed from a resistive radiation heater to an infrared laser heating system (see Fig. 3, left) including a pyrometer for determining the sample temperature. In addition, a source for atomic oxygen and nitrogen has been added. The main advantage of the new heating system is that only the substrate is heated while the surrounding parts are hardly affected (Fig. 3, right). In this way one can achieve an essentially better vacuum at temperatures well above 1000°C. The achievable substrate temperature is limited by the melting point and the size of the substrate material (approx. 1410°C for a 5 × 5 mm^2 silicon substrate). The laser heating system has already been successfully used for removing the amorphous silicon oxide layer from the surface of silicon substrates at 1150°C. This is required for the epitaxial growth of oxide thin films on this substrate.

Figure 2: Pulsed Laser Deposition (PLD): When the pulse of the UV laser (KrF excimer laser, 248 nm) hits the target, the target material is ablated and the so-called laser "plume" containing highly excited atoms and molecules is formed.

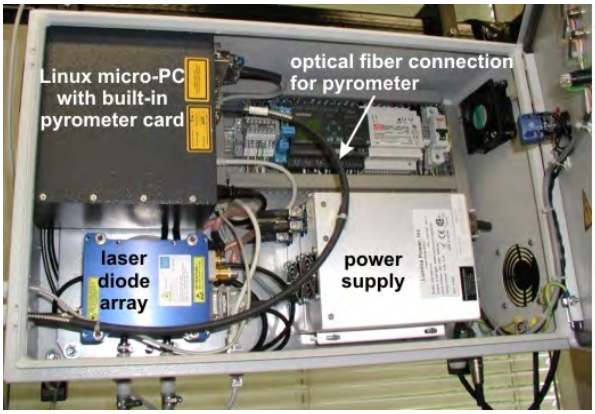

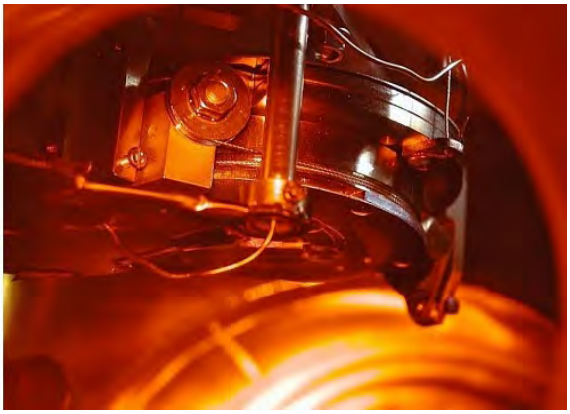

Figure 3: Components of the laser heating system: The substrate is heated using an IR diode laser head that is located in a separate box far away from the deposition chamber (left). The laser light is brought to the substrate (right) via an optical fiber.

Single Crystal Growth and Synthesis of Bulk Materials

Transition metal oxides are of great interest due to their various interesting physical properties (e.g. high temperature superconductivity, colossal magnetoresistance, ferroelectricity, nonlinear optical properties etc.) and their high potential for applications. Therefore, the WMI operates a laboratory for the synthesis of bulk materials and single crystals of transition metal oxides. Besides various chamber- and tube furnaces a four-mirror image furnace is used in the crystal growth of various oxide systems. With this furnace crystals of many different compounds of the high temperature superconductors and various other transition metal oxides have been grown as single crystals using the traveling solvent floating zone technique. The furnace consists basically of 4 elliptical mirrors with a common focus on the sample rod and with halogen lamps in their other focus. By irradiation of the focused light the sample rod is locally heated and eventually molten. The molten zone can be moved up and down along the entire sample rod under simultaneous rotation. Due to the anisotropic growth velocity a preferential growth of those grains with the fastest growth velocity along the pulling direction is obtained and the formerly polycrystalline rod is transformed into a single crystal. Single crystal growth can be performed with this furnace at maximum temperatures up to 2200°C in the pressure range from 10^{-5}mbar up to 10 bar and in oxidizing, reducing as well as inert atmosphere.

Figure 4: The four-mirror image furnace installed at the crystal laboratory of the WMI. Crystals can be grown by the floating zone and traveling solvent floating zone technique at temperatures up to 2200°C and pressures up to 10 bar.

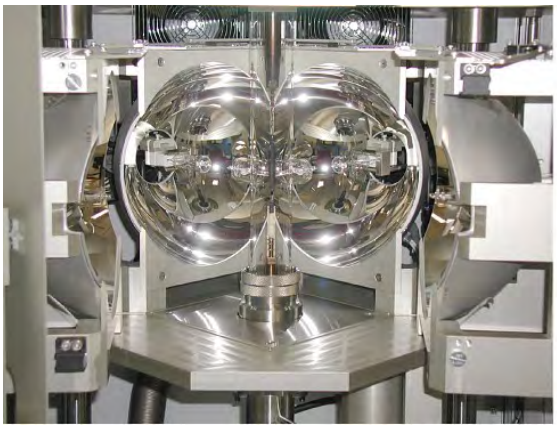

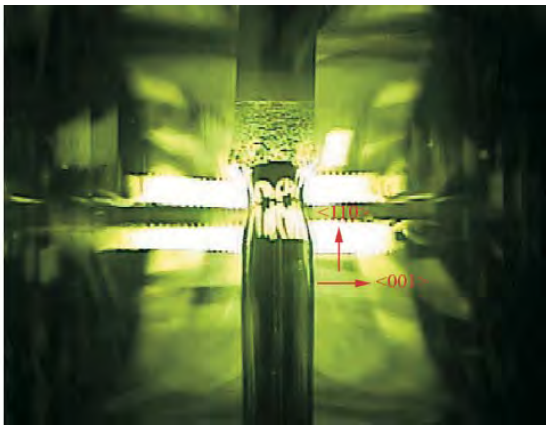

Figure 5: Left: Central part of the image furnace with the four elliptical mirrors. In the center one can see the quartz tube with the poly-crystalline rod. Right: View on the molten zone of $Pr_{2-x}Ce_xCuO_4$ (melting point: 1280°C) obtained by a CCD camera.

The X-ray diffraction systems

For x-ray analysis the Walther-Meissner-Institute operates two X-ray diffractometers (Bruker D8 Advance and D8 Discover). The two-circle system is used for powder diffraction. In this system the samples can be heated in oxygen atmosphere up to 1600°C. It is equipped with a Göbel mirror and an area detector to save measuring time. The second system is a high resolution four-circle diffractometer that can be used for reciprocal space mappings. It is equipped with a Göbel mirror and an asymmetric two-fold monochromator and allows for the texture analysis of thin film superlattices and single crystalline materials. In both systems measurements can be carried out fully computer controlled.

Figure 6: The two-circle X-ray diffractometer Bruker D8 Advance.

Beyond these two Bruker x-ray systems a Laue camera for single crystal analysis and a Debye-Scherrer camera are available.

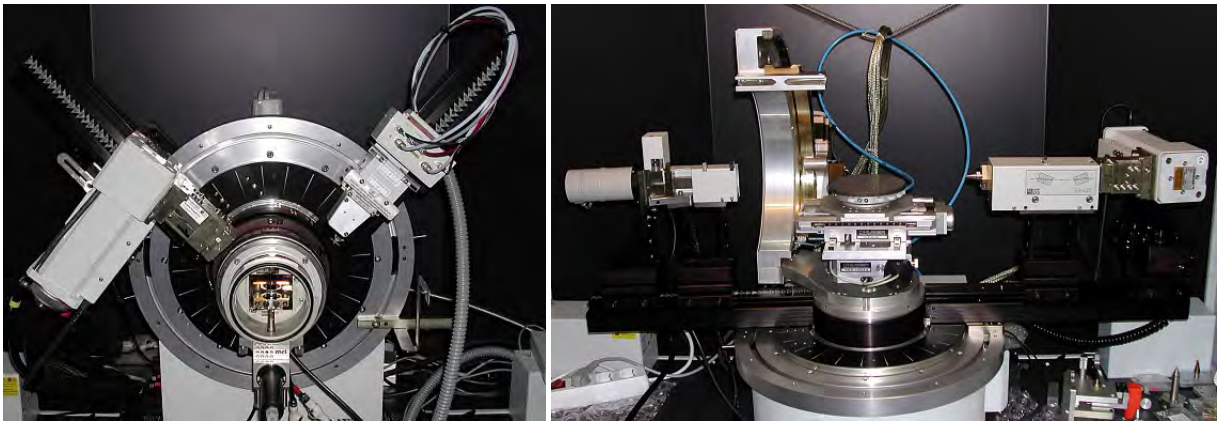

Figure 7: Left: High temperature sample holder of the D8 Advance system. Right: Four-circle high resolution X-ray diffractometer Bruker D8 Discover.

Figure 8: Quantum Design SQUID magnetometer.

The SQUID-magnetometer

For the analysis of the magnetic properties of materials, a Quantum Design SQUID magnetometer system as shown in Fig. 8 is used at the WMI. The SQUID magnetometer allows for measurements in the temperature regime from 1.5 to 400 K and provides excellent sensitivity particularly in the low field regime. Due to the excellent sensitivity of the system, thin film samples with a very small sample volume can be analyzed. In a special inset, samples can be measured up to temperatures well above room temperature (up to 500°C). For this option the sample volume has to be reduced. The SQUID magnetometer is equipped with a superconducting solenoid allowing for a maximum field of 7 T. At present, the magnetometer is used for the characterization of magnetic materials (both in bulk and thin film form). Examples are the doped manganites, magnetite, the double perovskites, magnetic semiconductors, or multiferroics.

The High Field Laboratory

Transport and thermodynamic properties of samples are often studied as a function of applied magnetic field. For such measurements several superconducting magnets are available at the WMI. Two of them (8/10 and 15/17 Tesla magnet system) are located in the high magnetic field laboratory in the basement of the WMI. The magnet systems are lowered below the ground level to facilitate the access to the top flange and the change of the sample sticks. The magnet systems are decoupled from the building to avoid noise due to mechanical vibrations. A variety of sample holders can be mounted allowing for e.g. sample rotation during the measurement. For standard sample holders the accessible temperature regime is 1.5 K$< T <$ 300 K. However, also ^{3}He/^{4}He dilution refrigerator inserts ($T >$ 20 mK) or high temperature units ($T <$ 700 K) can be mounted. All measurements are fully computer controlled (by the use of the LabView software tool) allowing for remote control and almost continuous measurements.

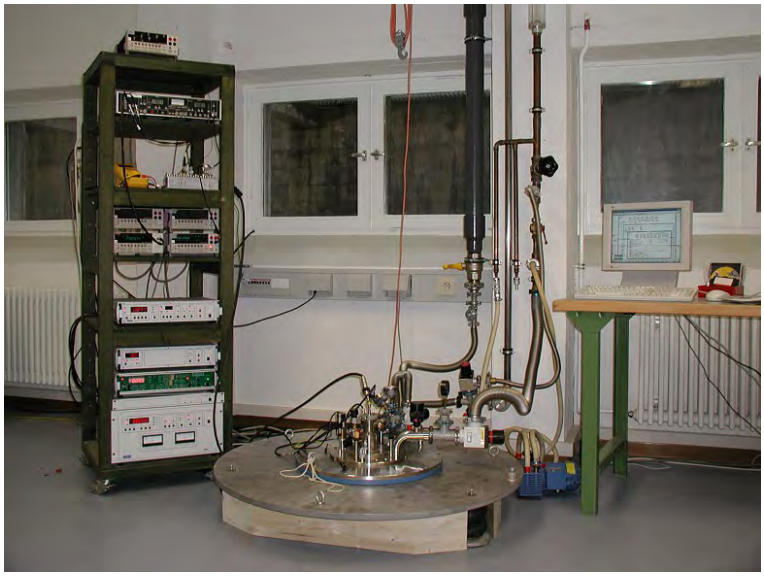

Figure 9: High field laboratory with Oxford 17 T magnet system.

Figure 10: Top: Part of the clean room facility with optical lithography equipment and clean room benches. Bottom: Resist coater and hot plates.

The Clean Room Facility

For the fabrication of nanostructures and superconducting as well as spintronic devices the WMI operates a class 1000 clean room facility with an area of about 50 m^2. This clean room facility has been put into operation at the WMI within the year 2001. The clean room is subdivided into two parts for optical lithography and electron beam lithography, respectively. The clean room facility is equipped with the standard tools for optical lithography such as resist coaters, hot plates, wet benches, a Karl Süss MJB3 mask aligner and an optical projection lithography system. The technical infrastructure for the clean room is located in the basement of the WMI directly below the clean room area.

Since 2005 the clean room also is equipped with a reactive ion etching system, Plasmalab 80 Plus with ICP plasma source (Oxford Instruments Plasma Technology).

Electron Beam Lithography

The Electron Beam Lithography System is installed in one part of the clean room facility. It consists of a Philips XL 30 SFEG scanning electron microscope (SEM) with a Raith Elphy Plus electron beam lithography system and a laser interferometer table for precise stitching of writing fields.

The SEM is equipped with a hot field emitter and typically provides a beam diameter of less than 1.5 nm at $\geq$ 10 keV or about 2.5 nm at 1 keV. The lithography unit allows the fabrication of nanostructures down to about 10 nm. We have realized the controlled fabrication of metallic strip patterns with a strip width of about 20 nm. The electron beam lithography is used for the fabrication of nanostructures in metallic and oxide systems required for the study of quantum effects in mesoscopic samples.

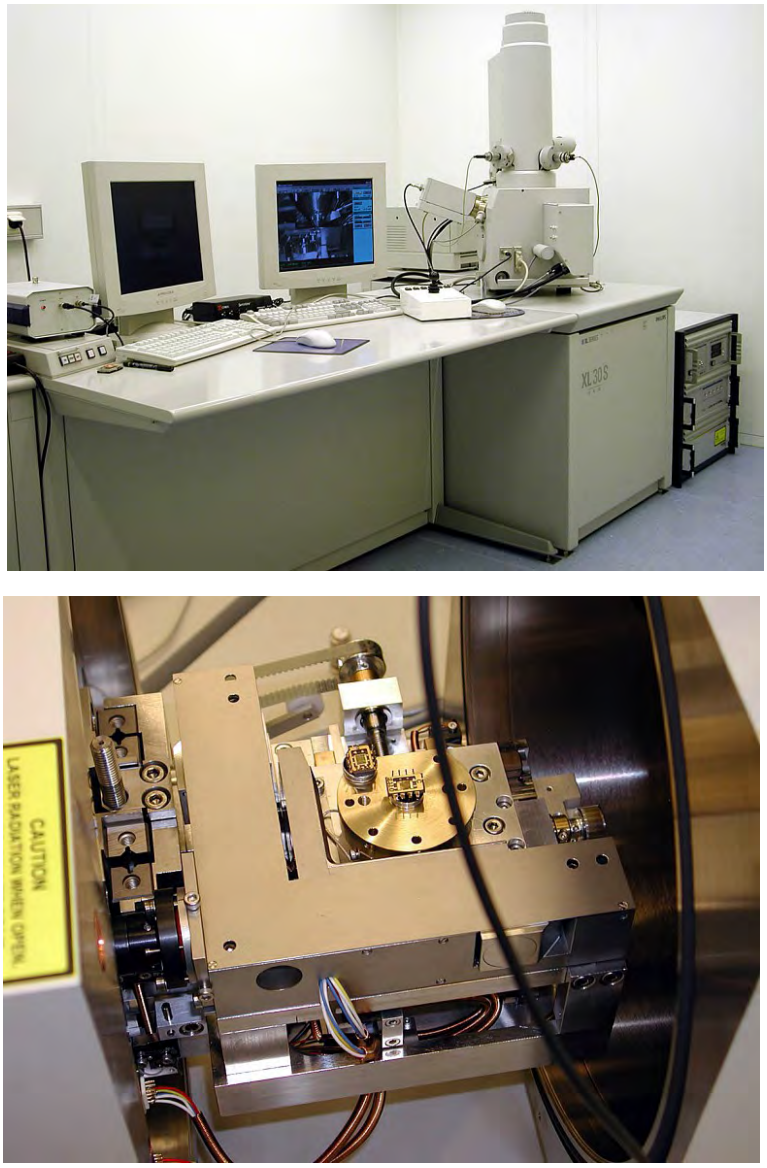

Figure 11: Top: Philips XL 30 SFEG Scanning Electron Microscope with Raith Elphy Plus Lithography System. Bottom: Raith Laser Stage.

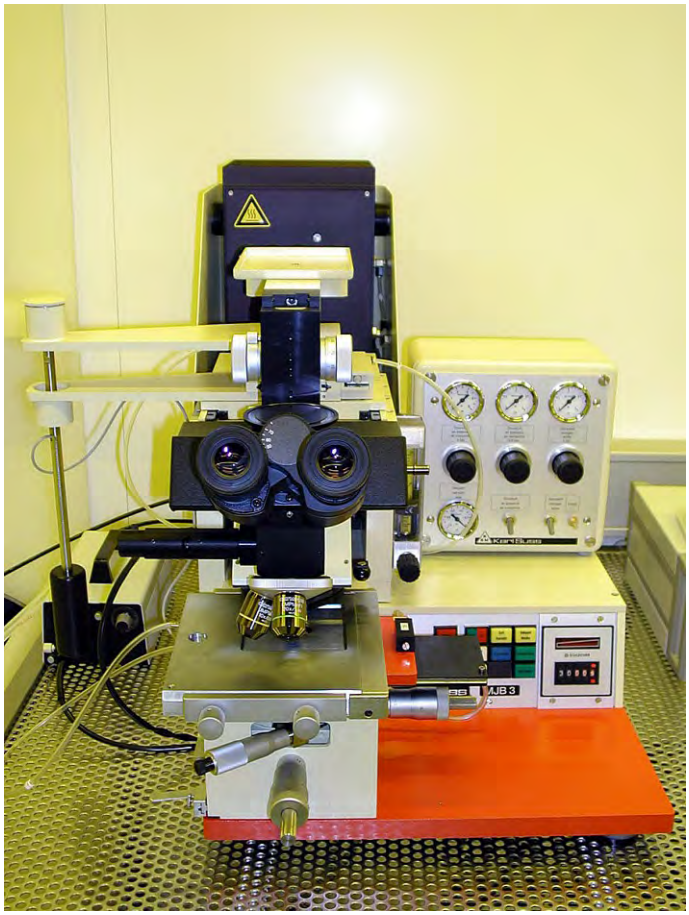

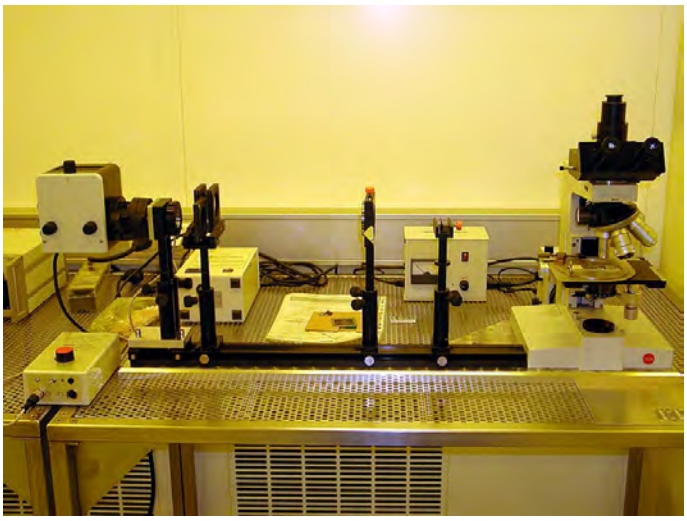

Figure 12: Top: Süss MJB 3 maskaligner for optical lithography. Bottom: Optical projection lithography based on an optical microscope.

Optical Lithography

For optical lithography a Karl Süss MJB 3 maskaligner or an optical microscope based projection system are used. The maskaligner is operating in the 1 : 1 soft or hard contact mode and is using chromium metal masks. In the projection system the mask pattern is demagnified by a factor of 5 to 100. Therefore, cheap foil masks can be used. With both systems microstructures with a lateral dimension down to 1 μm can be fabricated.

Low and Ultra-low Temperature Facilities

The WMI operates several low and ultra-low temperature facilities that have been developed and fabricated in-house.

The lowest temperature is achieved by the nuclear demagnetization cryostat "Bayerische Millimühle 2". This ultra-low temperature facility consists of an in-house built dilution refrigerator and originally of two nuclear demagnetization stages. The first of those is based on a hyperfine enhanced van Vleck paramagnet $PrNi_5$ (0.9 mole), the second, which has been removed a few years ago, was based on purified copper (0.2 mole). The lowest temperature reached with this system was slightly below 30 μK in the copper nuclear spin system. At the moment, the first stage can be cooled to below 400 μK and, due to the large heat capacity of $PrNi_5$, it stays below the mixing chamber temperature (5 mK) for nearly 3 weeks. In this cryostat three measuring sites are provided, two in a magnetic field compensated region and one in the center of an 8 T magnet. They are suitable for specific heat measurements, for capacitive torque- and SQUID magnetometry, as well as for transport measurements (electrical und thermal conductivity). The cryostat is also equipped with a pressure cell for liquid and solid ^{3}He, which at the moment is used for nuclear spin resonance measurements below 1 mK.

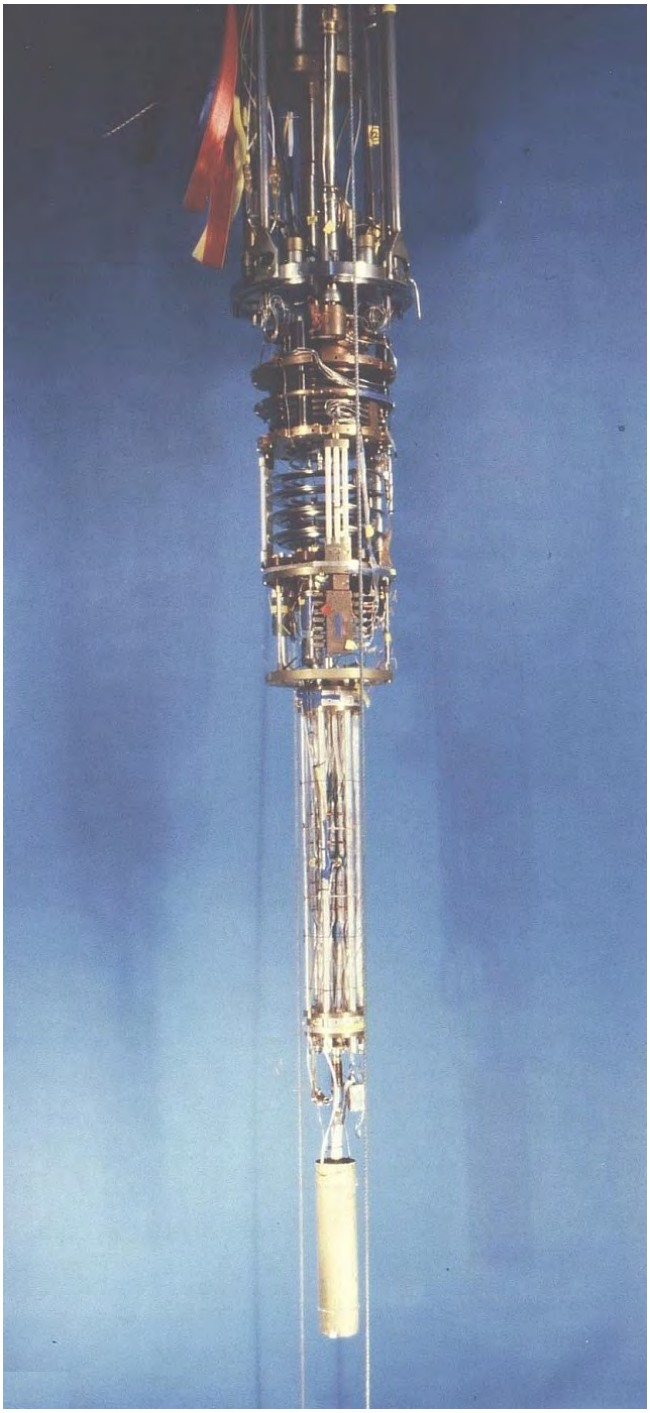

Figure 13: The dilution refrigerator and the nuclear demagnetization stage of the nuclear demagnetization cryostat "Bayerische Millimühle 2".

Some years ago, at the WMI, we have constructed the first dilution refrigerator with pulse tube pre-cooling for ultra-low temperature experiments. This type of refrigerator works without cryo-liquids, and thus is a lot more practical, more economical and more reliable than cryostats with liquid helium pre-cooling. These days, all major cryo-engineering firms are offering commercial versions of this milli-Kelvin cooler, and these so-called "dry" refrigerators outsell conventional refrigerators by a wide margin. The general construction concept of most manufacturers is unchanged from our original prototype, where the refrigerator consists of three basic components. The first cooling stage is a commercial pulse tube cryocooler which reaches a base temperature of 2.5 K. The second stage is a Joule-Thomson stage, and the last stage is a dilution refrigeration stage, where the lowest temperature of the cryostat is about 0.01 K (Fig. 14).

Figure 14: The "dry" dilution refrigerator of the WMI.

Figure 15: Low-temperature unit of a WMI dilution refrigerator ready to go into a cryostat.

In many low temperature applications high refrigeration capacities are required. Our design allows for a high circulation rate of ^{3}He which in the end determines the cooling power of a dilution refrigerator. Presently our "dry" fridge reaches a refrigeration capacity of 700 μW at a temperature of the mixing chamber of 0.1 K, seven times the cooling power of the WMI nuclear demagnetization cryostat. Goals of our present work are a further increase of cooling power and a lower base temperature of the dry dilution refrigerator.

Figure 16: Two mixing chamber mounting plates with silver sponges. Those are needed to overcome the thermal resistance (Kapitza resistance) between the liquid ^{3,4}He and the mounting plate of the mixing chamber. To fabricate the mounting of the sponge (square pins embedded in the sponge) a spark erosion technique has been employed.

A smaller version of our cryogen-free fridge has become commercially available at VeriCold Technologies, Ismaning. It has a refrigeration capacity of 250 μW at a mixing chamber temperature of 0.1 K (Fig.15).

The WMI also develops and fabricates dilution refrigerator inserts for temperatures down to about 20 mK. The inserts fit into all cryogenic systems (e.g. superconducting magnets) having a two inch bore. They allow fast sample change and rapid cool down cycles of less than five hours.

The dilution refrigerator inserts are engineered and fabricated in-house and are also provided to other low temperature laboratories for ultra low temperature experiments.

Low Temperature Scanning Tunneling Microscope with Ultra-High-Vacuum Characterization and Preparation Facilities

The low temperature scanning tunneling microscope allows investigation of low dimensional systems such as self-organized molecules, superconductors, magnetic and hetero-structure surfaces. The LT-STM is integrated into an ultra-high vacuum (UHV) chamber together with a variety of analytical as well as preparation tools. A newly added Quartz-Crystal-Microbalance allows quantitative controlling of evaporation processes. Monitoring is possible from island growth up to a film thickness of hundreds of atomic layers.

The Low Temperature Scanning Tunneling Microscope. The LT-STM (see Fig. 17a) is designed for easy handling under UHV as well as low temperature conditions. We control the Omicron STM by an electronics of the RHK company (see Fig. 17b).

Following, the technical features are listed:

- In-situ sample and tip exchange (manipulator see Figure 18 a).
- Vibration isolation ensured by a spring suspension system with eddy current damping and pneumatic damping legs.
- Variable temperatures from 5 K (pumped 2 K) up to room temperature ($\approx$ 300 K).
- Fast system cool-down (5 K within $\approx$ 6 hours).
- Sample pre-cooling to 50 K on the manipulator stage.
- Fast sample cool-down (5 K within $\approx$ 2 hours).
- On-line optical access and on-line four terminal transport measurements.
- Up to 6 samples can be stored at low temperature (77 K).

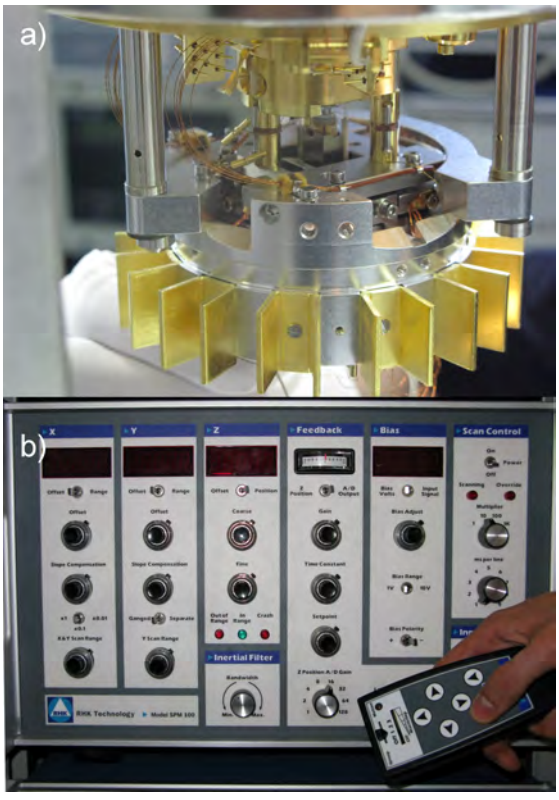

Figure 17: a) Inner view on the STM displaying part of the damping system, various cables and the scanning head (barely visible in the middle above the well). b) Photograph of our RHK scan electronic.

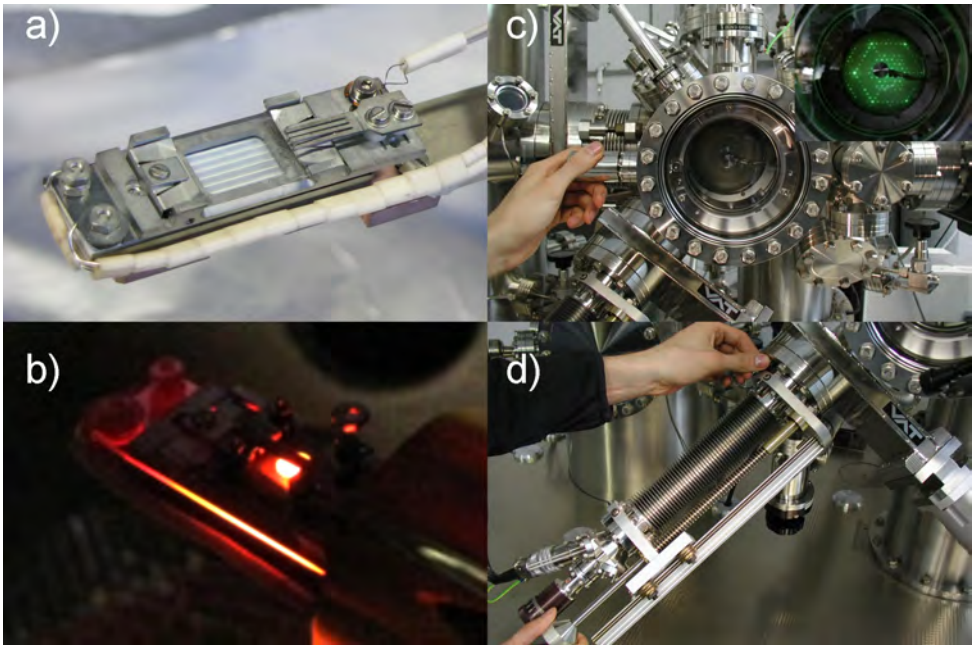

Figure 18: a) Close up on the manipulator for sample handling in the UHV chamber. b) Manipulator with Si-sample at 510°C under UHV conditions. The body of the manipulator is cooled to prevent damage. c) LEED spectrometer; inset LEED-diffraction image of the Si [111] 7×7 reconstruction. d) Photograph of the evaporator.

Preparation and Characterization Facilities. In addition to the LT-STM analysis chamber a second UHV chamber allows for sample preparation and characterization under UHV-conditions. Substrates can be prepared by an argon sputter gun and thermal annealing. A three crucible evaporator allows the deposition of molecules onto the surface; the deposition process is controlled by a quartz crystal microbalance. For sample characterization low-energy-electron-diffraction (LEED) and quadrupole mass spectrometry are available.

Argon Sputter Gun: Inside the preparation chamber clean single crystalline substrates are prepared by ion-sputtering and subsequent thermal annealing, which can be controlled by a three-grid low energy electron diffractometer (LEED) (see below) in a vacuum of 10^{-11} mbar.

Sample Heating/Cooling Stage: On the manipulator (see figure 18 a) samples can be prepared by direct current and indirect heating (see figure 18 b). Sample temperatures of up to 1073 K can be realized and the sample can be cooled to 50 K before transferring to the STM.

Low Energy Electron Diffraction (LEED): The surface ordering of (reconstructed) substrate/single crystal surfaces or molecular ad-layers can be analyzed by low energy electron diffraction (see figure 18 c).

Evaporator for Organic Material: A microprocessor controlled evaporator allows deposition of up to three different organic materials at the same time (see figure 18 d). Crucibles are refilled without breaking the vacuum of the main chamber.

Quartz-Crystal-Microbalance: For controlling the evaporation process and quantitative measurements of the number of adsorbed layers on/coverage of the substrate during evaporation a quartz-crystal-microbalance was recently added. Growth rates of 0.01 nm/s corresponding to a frequency change of 0.03 Hz/s can be monitored.

Quadrupole Mass Spectrometer: Samples are additionally characterized by desorption spectroscopy with a quadrupole mass spectrometer. The desorbing molecules are ionized in a crossbeam ion source and accelerated in the quadrupole mass spectrometer, which either uses a Faraday cup or secondary electron multiplier (SEM) as detector with a mass resolution up

to 2048 u.

Multiple additional vacuum ports allow further extensions of the Omicron STM in the future.

Tip etching facility (ex situ): The standard procedure for preparing STM tips - suitable for STM measurements - is cutting a PtIr-wire with scissors. Other tip materials (e.g. Tungsten, Gold, Niobium,...) have to be etched in order to form the necessary tip radii. A newly constructed tip etching facility allows for more tip materials than PtIr opening up the possibility of usage of e.g. superconducting tips.

Magnetic Field Low Temperature Ultra-High-Vacuum (UHV) – Scanning Tunneling Microscope (STM). The high stability of the instrument, the magnetic field as well as temperatures as low as 2.7 K allow the investigation of high temperature superconductors (HTSC) and organic superconductors. The STM is optimized for low temperature tunneling imaging and spectroscopy in high magnetic fields under UHV-conditions (see figure 19). A home-built electronics allows tunneling spectroscopy at points along lines, in grids and in a high density modus.

Figure 19: The current setup of the instrument: visible is the cryostat with microscope inside, as well as parts of the control electronics.

Technical Features of the STM.

- Imaging resolution: 0.01 nm in $x-y$-direction and 0.005 nm in z-direction.
- Current-voltage spectroscopy ($I-V$) (voltage resolution: 0.05 meV).
- Current-distance curves ($I-d$).
- Maximum scan size: $1\,\mu\text{m}\times 1\,\mu\text{m}$ at 4.2 K.
- Superconducting magnet up to 4 T with persistent switch.
- Vibration damping through spring suspension.
- Temperature range from room temperature down to liquid helium temperature at 4.2 K (pumped 2.7 K).
- Cryostat with LHe durability of one week (without thermal load).

Publications

1. **Elastically Driven Ferromagnetic Resonance in Nickel Thin Films**
   Mathias Weiler, Lukas Dreher, Christian Heeg, Hans Huebl, Rudolf Gross, Martin S. Brandt, Sebastian T.B. Goennenwein
   Phys. Rev. Lett. **106**, 117601 (2011).

2. **Magnetic microstructure and magnetotransport in Co_2FeAl Heusler compound thin films**
   Mathias Weiler, Franz D. Czeschka, Inga-Mareen Imort, Günter Reiss, Andy Thomas, Georg Woltersdorf, Rudolf Gross, Sebastian T. B. Goennenwein
   Appl. Phys. Lett. **98**, 042501 (2011).

3. **Novel Multifunctional Materials Based on Oxide Thin Films and Artificial Heteroepitaxial Multilayers**
   M. Opel, S. Geprägs, E.P. Menzel, A. Nielsen, D. Reisinger, K.-W. Nielsen, A. Brandlmaier, F.D. Czeschka, M. Althammer, M. Weiler, S.T.B. Goennenwein, J. Simon, M. Svete, Wentao Yu, S.-M. Hühne, W. Mader, R. Gross
   Phys. Status Solidi A **208**, 232–251 (2011).

4. **Fermi Surface of the Electron-overdoped Superconductor $Nd_{2-x}Ce_xCuO_{4+\delta}$ Probed by High Field Magnetotransport**
   M. V. Kartsovnik, T. Helm, C. Putzke, F. Wolff-Fabris, I. Sheikin, C. Proust, D. Vignolles, N. Bittner, W. Biberacher, A. Erb, J. Wosnitza, and R. Gross
   New J. Phys. **13**, 015001 (2011).

5. **Scaling Behavior of the Spin Pumping Effect in Ferromagnet-Platinum Bilayers**
   F. D. Czeschka, L. Dreher, M. S. Brandt, M. Weiler, M. Althammer, I.-M. Imort, G. Reiss, A. Thomas, W. Schoch, W. Limmer, H. Huebl, R. Gross, and S. T.B. Goennenwein
   Phys. Rev. Lett. **107**, 046601 (2011).

6. **Paarweise im Fluss**
   D. Einzel, R. Gross
   Physik Journal **10**, No. 6, 45–48 (2011).

7. **Nonvolatile, reversible electric-field controlled switching of remanent magnetization in multifunctional ferromagnetic/ferroelectric hybrids**
   A. Brandlmaier, S. Geprägs, G. Woltersdorf, R. Gross, and S. T. B. Goennenwein
   J. Appl. Phys. **110**, 043913 (2011).

8. **Local tunneling magnetoresistance probed by low-temperature scanning laser microscopy**
   R. Werner, M. Weiler, A. Yu. Petrov, B. A. Davidson, R. Gross, R. Kleiner, S. T. B. Goennenwein, and D. Koelle
   Appl. Phys. Lett. **99**, 182513 (2011).

9. **Electroelastic Hyperfine Tuning of Phosphorus Donors in Silicon**
   L. Dreher, T. A. Hilker, A. Brandlmaier, S. T. B. Goennenwein, H. Huebl, M. Stutzmann, and M. S. Brandt
   Phys. Rev. Lett. **106**, 037601 (2011).

10. **50 Years of Fluxoid Quantization: 2e or Not 2e**
    Dietrich Einzel
    J. Low Temp. Phys. **163**, 215–237 (2011).

11. **Superconductivity in copper-oxygen compounds**
    R. Hackl
    Zeitschrift für Kristallographie Vol. **226**, No. 4, 323–342 (2011).

12. **Electrical Detection of Coherent Nuclear Spin Oscillations in Phosphorus-Doped Silicon using Pulsed ENDOR**
    Felix Hoehne, Lukas Dreher, Hans Huebl, Martin Stutzmann, and Martin S. Brandt
    Phys. Rev. Lett. **106**, 187601 (2011).

13. **Coplanar stripline antenna design for optically detected magnetic resonance on semiconductor quantum dots**
F. Klotz, H. Huebl, D. Heiss, K. Klein, J. J. Finley, and M. S. Brandt
Rev. Sci. Instr. **82**, 074707 (2011).

14. **High-resolution electrical detection of free induction decay and Hahn echoes in phosphorus-doped silicon**
Jinming Lu, Felix Hoehne, Andre R. Stegner, Lukas Dreher, Martin Stutzmann, Martin S. Brandt, and Hans Huebl
Phys. Rev. B **83**, 235201 (2011).

15. **Intercalation and dynamics of hydrated Fe^{2+} in the vermiculites from Santa Olalla and Ojén**
Anton Lerf, Friedrich E. Wagner, Juan Poyato, José Luis Pérez-Rodríguez
J. Sol. State Electrochem. **15**, 223–229 (2011).

16. **Magnetic Transformations in the Organic Conductor κ-$(BETS)_2Mn[N(CN)_2]_3$ at the Metal-Insulator Transition**
O.M. Vyaselev, M.V. Kartsovnik, W. Biberacher, L.V. Zorina, N.D. Kushch, and E.B. Yagubskii
Phys. Rev. B **83**, 094425 (2011).

17. **Extracting the dynamical effective interaction and competing order from an analysis of Raman spectra of the high-temperature $La_{2-x}Sr_xCuO_4$ superconductor**
S. Caprara, C. Di Castro, B. Muschler, R. Hackl, M. Lambacher, A. Erb, S. Komiya, Y. Ando, M. Grilli
Phys. Rev. B **84**, 054508 (2011).

18. **Observation of a first-order phase transition deep within the vortex-solid region of $YBa_2Cu_3O_7$**
M Reibelt, S Weyeneth, A Erb, and A Schilling
Supercond. Sci. Techn. **24**, 105019 (2011).

19. **Magnetic-field-induced nonlocal effects on the vortex interactions in twin-free $YBa_2Cu_3O_7$**
J. S. White, R. W. Heslop, A. T. Holmes, E. M. Forgan, V. Hinkov, N. Egetenmeyer, J. L. Gavilano, M. Laver, C. D. Dewhurst, R. Cubitt, and A. Erb
Phys. Rev. B **84**, 104519 (2011).

20. **Magnetic torque study of the temperature-dependent anisotropy parameter in overdoped superconducting single-crystal $YBa_2Cu_3O_7$**
S. Bosma, S. Weyeneth, R. Puzniak, A. Erb, A. Schilling, and H. Keller
Phys. Rev. B **84**, 024514 (2011).

21. **Light scattering study of low-energy vibrational excitations in the metallic glass $Ni_{67}Zr_{33}$ using electronic Raman scattering**
B. Muschler, I. Tütto, A. Zawadowski, J. Balogh, and R. Hackl
Phys. Rev. B **84**, 104104 (2011).

22. **Investigation of particle-hole asymmetry in the cuprates via electronic Raman scattering**
B. Moritz, S. Johnston, T. P. Devereaux, B. Muschler, W. Prestel, R. Hackl, M. Lambacher, A. Erb, Seiki Komiya, and Yoichi Ando
Phys. Rev. B **84**, 235114 (2011).

23. **Sonication induced reduction of the Ojen (Andalucia, Spain) vermiculite under air and under nitrogen**
Juan Poyato, José Luis Pérez-Rodríguez, Anton Lerf, Friedrich E. Wagner,
Ultrasonics Sonochemistry **19**, 373–375 (2012).

24. **Quantum Simulation of the Ultrastrong Coupling Dynamics in Circuit QED**
D. Ballester, G. Romero, J. J. García-Ripoll, F. Deppe, E. Solano
arXiv:1107.5748v1, submitted for publication (2011).

25. **Pair breaking versus symmetry breaking: Origin of the Raman modes in superconducting cuprates**
N. Munnikes, B. Muschler, F. Venturini, L. Tassini, W. Prestel, Shimpei Ono, Yoichi Ando, D. C.

Peets, W. N. Hardy, Ruixing Liang, D. A. Bonn, A. Damascelli, H. Eisaki, M. Greven, A. Erb, and R. Hackl
Phys. Rev. B **84**, 144523 (2011).

26. **Field-induced charge-density-wave transitions in the organic metal α-(BEDT-TTF)$_2$KHg(SCN)$_4$ under pressure**
D. Andres, M. Kartsovnik, W. Biberacher, K. Neumaier, I. Sheikin, H. Müller, N. Kushch,
Fiz. Niz. Temp. **37**, 959 (2011); Low Temp. Phys., in press.
Invited paper in the special issue to the 80th anniversary of Prof. V.G. Peschansky

27. **Magnetic field effects on the charge-density-wave and superconducting state in pressurized α-(BEDT-TTF)$_2$KHg(SCN)$_4$**
M.V. Kartsovnik, W. Biberacher, D. Andres, S. Jakob, M. Kunz, K. Neumaier, H. Müller, N.D. Kushch
Physica B, accepted for publication (2011).

28. **Cryogen-free dilution refrigerator with separate 1K cooling circuit**
K. Uhlig,
Advances in Cryogenic Engineering, accepted for publication (2011).

29. **Cryogen-free Dilution Refrigerators**
K. Uhlig,
Journal of Physics, accepted for publication (2011).

30. **Spintronic oxides grown by laser-MBE**
M. Opel,
J. Phys. D: Appl. Phys., accepted for publication (2011).

31. **Kinetic theory for response and transport in non-centrosymmetric superconductors**
Ludwig Klam, Dirk Manske, Dietrich Einzel
arXiv:1003.0407, submitted for publication (2011).

32. **Selection rules in a strongly coupled qubit-resonator system**
T. Niemczyk, F. Deppe, E. P. Menzel, M. J. Schwarz, H. Huebl, F. Hocke, M. Häberlein, M. Danner, E. Hoffmann, A. Baust, E. Solano, J. J. Garcia-Ripoll, A. Marx, R. Gross
arXiv:1107.0810, submitted for publication (2011).

33. **Experimental observation of an enhanced anisotropic magnetoresistance in non-local configuration**
Daniel Rüffer, Franz D. Czeschka, Rudolf Gross, Sebastian T. B. Goennenwein
arXiv:1108.2125v1, submitted for publication (2011).

34. **Magneto-optical imaging of voltage-controlled magnetization reorientation**
A. Brandlmaier, M. Brasse, S. Geprägs, M. Weiler, R. Gross, S. T. B. Goennenwein
arXiv:1108.3521v1, submitted for publication (2011).

35. **Local charge and spin currents in magnetothermal landscapess**
Mathias Weiler, Matthias Althammer, Franz D. Czeschka, Hans Huebl, Inga-Mareen Imort, Günter Reiss, Andy Thomas, Rudolf Gross, and Sebastian T. B. Goennenwein
arXiv:1110.3981v1, submitted for publication (2011).

Theses, Appointments, Honors and Awards, Membership in Advisory Boards, etc.

Completed and ongoing Ph.D. Theses

1. **Rules of Molecular Self-Organization: Emergence, Control and Predictability**
   Carsten L. Rohr, LMU München, Juni 2011.
2. **From Strong to Ultrastrong Coupling in Circuit QED Architectures**
   Thomas Niemczyk, TU München, Juli 2011.
3. **Spin Currents in Metallic Nanostructures**
   Franz Dominik Czeschka, TU München, August 2011.
4. **Electric-field Control of Magnetization in Multifunctional Hybrid Devices**
   Andreas Brandlmaier, TU München, August 2011.
5. **Magnetoelectric Interactions in Multiferroic Thin Films and Composites**
   Stephan Geprägs, TU München, Dezember 2011.
6. **Josephson Junctions with Ferromagnetic Interlayer**
   Georg Wild, TU München, Januar 2012.
7. **Untersuchung der Wechselwirkungspotenziale in Kupratsupraleitern durch quantitativen Vergleich spektroskopischer Resultate**
   Wolfgang Prestel, TU München, seit November 2004.
8. **Kohärente Dynamik und Dekohärenz in supraleitenden Quantenbits**
   Edwin Menzel, TU München, seit Januar 2006.
9. **(Bio) Sensorik mit Cantileverarrays und Oberflächenkontrolle mittels Rastersondentechniken**
   Kathrin Gruber, LMU München, seit November 2007.
10. **Korrelierte Systeme untersucht mit Tieftemperatur-Rastersondenmikroskopie**
    Johannes Büttner, LMU München, seit Januar 2008.
11. **Magnetotransporteigenschaften von dünnen ferromagnetischen Schichten und Heterostrukturen**
    Mathias Weiler, TU München, seit Februar 2008.
12. **Untersuchung von Kupraten nahe des Einsatzpunktes der Supraleitung**
    Bernhard Muschler, seit Februar 2008.
13. **Multifunktionale magnetische Heterostrukturen**
    Matthias Althammer, TU München, seit April 2008.
14. **Herstellung und Charakterisierung von supraleitenden Schaltkreisen zur Realisierung von gekoppelten supraleitenden Quantenbauelementen**
    Elisabeth Hoffmann, TU München, seit April 2008.
15. **Quantenexperimente mit elektromechanischen Systemen**
    Fredrik Hocke, TU München, seit Mai 2008.
16. **Wechselwirkung zwischen Spin-, Gitter- und Ladungsfreiheitsgraden in korrelierten Metallen ohne Inversionszentrum**
    Hans-Martin Eiter, TU München, seit Oktober 2008.
17. **Properties of High-T_c Cuprates in Large Magnetic Fields**
    Toni Helm, TU München, seit März 2009.
18. **Superconducting Flux Qubits with Tunable Gap**
    Manuel Schwarz, TU München, seit Juni 2009.

19. **All Optical Quantum Computing**
    Max Häberlein, TU München, seit Dezember 2009.
20. **Raman-Untersuchungen an stark korrelierten Systemen mit hoher Ortsauflösung**
    Florian Kretschmar, TU München, seit Januar 2010.
21. **Vibrational Investigations of Luminescence Molecules**
    Nitin Chelwani, TU München, seit September 2010.
22. **Time-Domain Measurements on Ultra-strong-coupled Qubit -Resonator Systems**
    Alexander Baust, TU München, seit Oktober 2010.
23. **Spinabhängige thermogalvanische Effekte in ferromagnetischen Dünnschichten**
    Johannes Lotze, TU München, seit April 2011.
24. **Generation of Propagating Quantum Microwave Signals on a Single Photon Level Using Multi-resonator Systems and Detection with Cross-correlation Techniques**
    Ling Zhong, TU München, seit November 2011.

The following Ph.D. students of the Walther-Meißner-Institute have finished their theses in 2011:

Thomas Niemczyk

Franz Czeschka

Stephan Geprägs

Carsten Rohr

Andreas Brandlmaier

Completed and ongoing Diploma, Bachelor, Master Theses

1. **Impedance matching of metal powder filters for experiments with superconducting flux quantum bits**
   Edwar Xie, Bachelor-Thesis, Januar 2011.
2. **Epitaktisches Wachstum dünner ferromagnetischer Schichten aus $Y_3Fe_5O_{12}$ mittels gepulster Laserdeposition**
   Martin Sebastian Wagner, Bachelor-Thesis, Juni 2011.
3. **Konstruktion eines automatisierten Aufbaus zur Messung von temperaturabhängigen Widerständen von Kupraten und organischen Supraleitern**
   Tobias Lamm, Bachelor-Thesis, Juli 2011.
4. **Aufzeichnen einer Energiewertstromanalyse am Beispiel der Zylinderkopffertigung der BMW Group im Werk München**
   Jacob Steffen Ducke, Bachelor-Thesis, Juli 2011.
5. **Herstellung ferroelektrisch/ferromagnetischer Hybridstrukturen**
   Frederik Goerg, Bachelor-Thesis, Juli 2011.
6. **Räumliche Untersuchung nanomechanischer Objekte mit Interferometrie**
   Rasmus Holländer, Bachelor-Thesis, August 2011.
7. **Konstruktion und Charakterisierung von gekoppelten Mikrostreifen-Resonatoren**
   Lukas Augsbach, Bachelor-Thesis, August 2011.
8. **Optimization of impedance matched stainless steel powder filters**
   Thomas Ramirez, Bachelor-Thesis, August 2011.
9. **Compact superconducting coplanar beam splitters**
   Norbert Kalb, Bachelor-Thesis, August 2011.
10. **Hochfeld-Magnetisierungsmessungen an κ-$(BETS)_2Mn[N(CN)_2]_3$**
    Fabian Jerzembeck, Bachelor-Thesis, August 2011.
11. **Scalable Sample Holder for Experiments with Superconducting Quantum Circuits**
    Uwe Ehmann, Bachelor-Thesis, August 2011.
12. **Experimentelle Untersuchungen zum Spin-Seebeck-Effekt**
    Georg Alexander Benka, Bachelor-Thesis, August 2011.
13. **Modellierung von Teilchendichten in Stickstoff- Niedertemperaturplasmen**
    Michael Gerl, Bachelor-Thesis, August 2011.
14. **Nanomechanische Experimente bei Radiofrequenzen**
    Alexander Kleinkauf, Bachelor-Thesis, August 2011.
15. **Simulation of the dual-path detector for propagating quantum microwaves**
    Philipp Summer, Bachelor-Thesis, August 2011.
16. **Preparation and Characterization of Highly Ordered Y-123**
    Marlies Gangl, Bachelor-Thesis, August 2011.
17. **Study of Doping and Pressure Dependent Electronic Properties in the Pnictides**
    Markus Künzl, Bachelor-Thesis, August 2011.
18. **Electronic Interactions in $HgBa_2CuO_{4+\delta}$**
    Valentin Kunkel, Bachelor-Thesis, August 2011.
19. **Heat Transport in Evacuated Perlite Powder Insulations and its Application in Long-Term Hot Water Storages**
    Matthias Demharter, Master-Thesis, August 2011.
20. **Analysing Muscle Functional Imaging Using Statistical Methods**
    Roberta Kriegl, Master-Thesis, August 2011.

21. **Herstellung und Charakterisierung von Fluss-Quantenbits mit vier Josephson-Kontakten**
    Felix Bilger, Oktober 2010.
22. **Magnetoresistance in the normal and superconducting states of the layered organic metal κ-(BEDT-TTF)$_2$KHg(SCN)$_4$ under pressure**
    Michael Kunz, November 2011.
23. **Nb/AlO$_x$/Nb Josephson-Kontakte für supraleitende Quantenschaltkreise**
    Karl-Friedrich Wulschner, Oktober 2011.
24. **Gradiometric Flux Quantum Bits with Tunable Tunnel Coupling**
    Jan Goetz, November 2011.
25. **Herstellung und Charakterisierung von Zinkoxid-Ferromagnet-Heterostrukturen zur Spininjektion**
    Eva-Maria Karrer-Müller, November 2011.
26. **Ferromagnetic Resonance at Low Temperatures**
    Christoph Zollitsch, November 2011.
27. **Microstrip Resonators for Circuit Quantum Electrodynamics**
    Marta Krawczyk, Master-Thesis, Dezember 2011.
28. **Untersuchung der Voraussetzung für Supraleitung in FeAs-Verbindungen**
    Andreas Baum, seit Dezember 2010.
29. **Dual-path State Reconstruction of Propagating Quantum Microwaves**
    Peter Eder, seit Januar 2011.
30. **Grundlagenuntersuchungen zur plasmainduzierten Entflammung bei hochaufgeladenen Ottomotoren**
    Thorsten Wolf, seit Januar 2011.
31. **Dotierungs- und Impedanzabhängigkeit der Elektronendynamik in HgBa$_2$CuO$_{4+\delta}$ und YBa$_2$Cu$_3$O$_{6+x}$**
    Thomas Böhm, seit Januar 2011.
32. **Modellierung und Simulation eines thermoelektrischen Generators (TEG) unter Berücksichtigung von lokalen Effekten**
    Torsten Steinert, seit Juni 2011.
33. **Spin Resonance of Phosphorous Donors in Silicon at mK Temperatures**
    Moritz Greifenstein, seit Juli 2011.
34. **Study of the Electronic Interactions in Highly Ordered YBa$_2$Cu$_3$O$_{6+x}$**
    Peter Jaschke, seit Juli 2011.
35. **The influence of surface structures on the tribological properties of diamond-like carbon films**
    Markus Felgenbauer, seit Oktober 2011.
36. **Time-domain control of light-matter interaction with superconducting circuits**
    Thomas Losinger, seit November 2011.
37. **Response and collective modes in non-cetrosymmetric superconductors**
    Nikolaj Bittner, seit November 2011.
38. **Ortsaufgelöste spin-kalorische Experimente**
    Michael Schreier, seit November 2011.
39. **Magnon-Phonon-Kopplung in dünnen ferromagnetischen Schichten**
    Matthias Pernpeintner, seit November 2011.
40. **Gradiometric superconducting flux qubits with tunable gap**
    Zhaohai Jiang, seit Dezember 2011.

Appointments, Membership in Advisory Boards, etc.

1. **Werner Biberacher** is member of the Selection Panel EuroMagNet II of the Joint European High Magnetic Field Laboratories.
2. **Dietrich Einzel** is one of the four spokesmen of the scientific staff of the Bavarian Academy of Sciences and Humanities.
3. **Sebastian Gönnenwein** is associate member of the Cluster of Excellence *Nanosystems Initiative Munich (NIM)*.
4. **Rudolf Gross** was acting as member of the steering committee of the Exploratory Roundtable Conference on Quantum Information Science, 2-4 November, 2011, Shanghai, China.
5. **Rudolf Gross** is member of the Scientific Advisory Board of the Leibniz Institute for Solid-State and Materials Research, Dresden.
6. **Rudolf Gross** is member of the Kuratorium of the Physik Journal of the German Physical Society.
7. **Rudolf Gross** is member of the selection committee of the Stern-Gerlach-Medal of the German Physical Society.
8. **Rudolf Gross** is spokesman of the division of *Low Temperature Physics* of the Condensed Matter Section of the German Physical Society.
9. **Rudolf Gross** is spokesman of the Collaborative Research Center 631 on *Solid State Quantum Information Processing* of the German Research Foundation.
10. **Rudolf Gross** is member of the Executive Board of the Cluster of Excellence *Nanosystems Initiative Munich (NIM)* and coordinator of the Research Area 1 on *Quantum Nanosystems*.
11. **Rudolf Gross** is member of the Board of Editors of the European Physical Journal B.
12. **Rudolf Gross** is member of the Board of Editors of Physica C.
13. **Rudolf Hackl** has been appointed member of the Advisory Board of the Conference "Low Energy Electron Dynamics LEES 2012".
14. **Rudolf Hackl** has been appointed member of the evaluation board of the neutron source Heinz Maier-Leibnitz (FRM II).

Research Projects and Cooperations

A large number of our research projects are benefiting from the collaboration with external groups in joint research projects, as well as from individual collaborations, exchange programs and visitors. Most collaborations are based on joint projects, which are funded by different research organizations (see list below). A considerable number of collaborations also exists with universities, other research institutions and industry without direct financial support.

Funded Projects

German Research Foundation: Excellence Initiative

Cluster of Excellence "Nanosystems Initiative Munich"

1. Project Area I: *Quantum Nanophysics*
   F. Deppe, S.T.B. Gönnenwein, R. Gross, H. Hübl, A. Marx

2. Project Area II: *Hybrid Nanosystems*
   S.T.B. Gönnenwein, R. Gross, H. Hübl

German Research Foundation: Collaborative Research Centers

Collaborative Research Center 631: "Solid-State Quantum Information Processing: Physical Concepts and Materials Aspects"

1. Project A3: *Superconducting Quantum Circuits as Basic Elements for Quantum Information Processing*
   R. Gross, A. Marx

2. Project A8: *Cavity Quantum Electrodynamics with Superconducting Devices*
   A. Marx, R. Gross

3. Project C3: *Fundamentals of Quantum Logic Gates in Silicon*
   M. Brandt, H. Hübl, M. Stutzmann

4. Project S: *Coordination of the Collaborative Research Center*
   R. Gross

Transregional Collaborative Research Center TRR 80: "From Electronic Correlations to Functionality"

1. Project A2: *Spatially und Momentum Resolved Raman Studies of Correlated Systems*
   R. Hackl

German Research Foundation: Priority Programs

1. Spin-dependent thermo-galvanic effects: experiment
   within the DFG Priority Program 1538 *Spin-Caloric Transport – SpinCAT*
   S.T.B. Gönnenwein, R. Gross (Az. GO 944/4-1)

2. Project: *Spin injection, spin transport and controllable ferromagnetism in transition metal doped ZnO*
   within the DFG Priority Program 1285 *"Halbleiter-Spinelektronik"*
   R. Gross, S.T.B. Gönnenwein, M. Opel (Az. GR 1132/14-1, GR 1132/14-2, GR 1132/14-3)

3. Project: *Raman study of electron dynamics and phase transitions in iron-pnictide compounds*
   within the DFG Priority Program 1458 *"High-Temperature Superconductivity in Iron-Pnictides"*
   R. Hackl, R. Gross, B. Büchner, D. Johrendt, C. Honerkamp (Az. HA 2071/7-1)

German Research Foundation: Research Projects

1. Project: *Doping dependent evolution of the Fermi surface and competing ordering phenomena in superconducting cuprates*
   R. Gross, M. Kartsovnik, A. Erb (Az. GR 1132/15-1)

2. Project: *Interaction between spin, lattice, and charge in non-centrosymmetric correlated metals*
   R. Hackl, R. Gross (Az. HA 2071/5-1)

3. Project: *Study of π-d interaction in crystalline organic (super)conductors with 3d metal-complex ions*
   W. Biberacher (Az.: BI 340/3-1), bilateral cooperation with institutes of the Russian Academy of Science.

4. Project: *Local Magnetotransport Properties of Thin Ferromagnetic Layers and Heterostructures*
   S.T.B. Gönnenwein (Az. GO 944/3-1)

European Union

1. Marie Curie Network for Initial Training (ITN): *Circuit and Cavity Quantum Electrodynamics (CCQED)*
   R. Gross, A. Marx, F. Deppe, Grant Agreement No. PITN-GA-2010-264666
   partners: several European Universities and research facilities.

2. Marie Curie Network for Initial Training (ITN): *Cavity-confined Luminophores for Advanced Photonic Materials: A Training Action for Young Researchers (FINELUMEN)*
   R. Hackl, Grant Agreement Number PITN-GA-2008-215399
   partners: several European Universities and research facilities.

Alexander von Humboldt Foundation

1. Alumni Program for Prof. Dr. T.P. Devereaux, Stanford University, Stanford, USA
   R. Hackl

German Academic Exchange Service

1. German-Indian STAR Scholarship for Technology and Research, collaboration with IIT Madras (Prof. M.S.R. Rao)
   R. Gross

Ministerio de Educacion y Ciencia, Spanien

1. Intercalación de minerales de la arcilla por medio de tratamiento con ultrasonidos y reacciones de transferencia de electrones. Producciòn de arcillas funcionalizadas con estructuras complejas jerarquizadas en el espacio interlaminar.
   J.L. Perez-Rodriguez, A. Lerf (Reference No. : MAT2005-04838)

Conferences and Workshops

The Walther-Meißner-Institute has organized/co-organized the following conferences and workshops in 2011:

1. **Winter School of the Cluster of Excellence "Nanosystems Initiative Munich"**, March 27 – April 02, 2011, St. Christoph am Arlberg, Austria.

The Winter School was covering all main research topics of NIM, referring to the five research areas (i) Quantum Nanophysics, (ii) Hybrid Nanosystems, (iii) Nanosystems for Energy Conversion, (iv) Biomolecular Nanosystems, and (v) Biomedical Nanotechnologies. Sebastian Gönnenwein of WMI was acting as a member of the Program Committee of the Winter School.

2. **Bi-annual Meeting of the EU Marie Curie Project 215399 (FINELUMEN)** April 14 - 15, 2011, Munich Residence, Germany.

The workshop was organized by the EU Marie Curie Project FINELUMEN. FINELUMEN is a 4-year training and research project aiming at the preparation and extensive characterization of luminescent materials in which suitably designed organic and inorganic luminophores are encapsulated within confined media where they can preserve and even improve their emission output. The ultimate goal is to create a library of luminescent modules emitting throughout the VIS-NIR region for producing superior functional organic materials. The versatile properties of these materials will make them attractive in at least 3 applicative areas, i.e. bioimaging, optoelectronic devices and sensors. The research effort inside "FINELUMEN" calls for a multidisciplinary team in which key groups, experts in different fields of chemistry, physics and engineering tightly interact. The meeting was bringing together more than 50 scientists.

3. **Course 3 on "Applied Physics and Electronics" of the Ferienakademie 2011** September 18 – 30, 2011, Sarntal, Italy.

The course was hold by Rudolf Gross of WMI together with Prof. Dr. techn. Wolfgang M. Rucker, University of Stuttgart, within the Ferienakademie. The Ferienakademie is jointly organized by the Technische Universität München, the University of Erlangen/Nuremberg, and the University of Stuttgart to motivate and foster highly talented students. It takes place in the Italian Alps.

Collaborations

Other collaborations without direct project funding involve:

- Stanford University, Stanford, USA (Prof. T.P. Devereaux, M. Greven, Z.-X. Shen, I. Fisher)
- Universidad del País Vasco and Ikerbasque Foundation, Bilbao, Spain (Prof. E. Solano)
- Instituto de Fisica Fundamental, Madrid, Spain (J.J. Garcia-Ripoll)
- Instituto de Ciencia de Materiales de Sevilla, Spain (Prof. J. Poyato, Prof. J.L. Perez-Rodriguez)
- Research Institute for Solid State Physics and Optics, Hungarian Academy of Sciences, Budapest, Hungary (Prof. K. Kamaras and Prof. I. Tüttö, Dr. J. Balogh)
- University of Rome "La Sapienza", Rome, Italy (Prof. S. Caprara, Prof. C. Di Castro and Prof. M. Grilli)
- Hungarian Academy of Sciences, Budapest University of Technology and Economics, Budapest, Hungary (Dr. A. Virosztek, Prof. A. Zawadowski, G. Mihály)
- Central Research Institute of the Electric Power Industry, Tokyo, Japan (Dr. S. Ono and Dr. Y. Ando)
- Green Innovation Research Laboratories, NEC Corporation, Japan (Dr. Y. Nakamura, Dr. J.S. Tsai, Dr. K. Inomata, Dr. T. Yamamoto)
- NTT Basic Research Laboratories, Japan (Dr. K. Semba)
- University of Tohoku, Sendai, Japan (Prof. Dr. Gerrit E.W. Bauer)
- European Synchrotron Radiation Facility (ESRF), Grenoble (Dr. H. Müller, Dr. J. Criginski Cezar, Dr. D. Mannix)
- Materials Science Research Centre, IIT Madras, India (Prof. M.S. Ramachandra Rao)
- Raja Ramanna Centre for Advanced Technology, Indore, India (Prof. Lalit M. Kukreja)
- Clarendon Laboratory, University of Oxford, England (Dr. A. Karenowska)
- High Magnetic Field Laboratory, Toulouse (C. Proust, D. Vignolles)
- ETH-Zurich, Switzerland (Profs. L. Degiorgi, R. Monnier, Dr. M. Lavagnini)
- Chalmers University of Technology Gothenburg, Sweden (Prof. P. Delsing)
- MINT Center, University of Alabama (Prof. A. Gupta)
- Materials Physics Laboratory, Helsinki University of Technology, Finland (Dr. Tero Heikkilä)
- Kavli Institute of NanoScience, Delft University of Technology, Delft, The Netherlands (Prof. T.M. Klapwijk)
- High-Magnetic-Field Laboratory, Grenoble, France (Dr. I. Sheikin)
- B. Verkin Institute for Low Temperature Research and Engineering, Kharkov, Ukraine (Prof. V.G. Peschansky)
- Landau Institute for Theoretical Physics, Chernogolovka, Russia (Dr. P. Grigoriev)
- Russian Academy of Sciences, Chernogolovka, Russia (N. Kushch, A. Palnichenko)
- High Magnetic Field Laboratory, Dresden (E. Kampert, J. Wosnitza)
- National High Magnetic Field Laboratory, Tallahassee, USA (Prof. J. Brooks)
- University of Bonn, Germany (Prof. W. Mader)
- IFW Dresden, Germany (Prof. B. Büchner, Prof. J. Fink, Dr. S.V. Borisenko, Dr. M. Knupfer)

- Max-Planck-Institut für Festkörperforschung, Stuttgart (Prof. B. Keimer)
- University of Tübingen, Germany (Prof. R. Kleiner, Prof. D. Kölle)
- University of Würzburg, Germany (Prof. W. Hanke, Prof. F. Assaad, Prof. C. Honerkamp, Dr. M. Potthoff)
- University of Augsburg, Germany (Dr. S. Kohler, Prof. Dr. P. Hänggi, Prof. A. Wixforth)
- University of Hamburg, Germany (Dr. G. Meier, Prof. W. Wurth)
- University of Leipzig, Germany (Prof. J. Haase)
- Abt. Halbleiterphysik, University of Ulm, Germany (Dr. W. Limmer)
- RWTH Aachen, Germany (Prof. G. Güntherodt, Dr. B. Beschoten)
- Georg-August-Universität, Göttingen, Germany (Prof. M. Münzenberg)
- Institut für Experimentelle und Angewandte Physik, Universität Regensburg, Germany (Prof. Christian Back, Dr. Georg Woltersdorf, Dr. Dominique Bougeard)
- Universität Duisburg-Essen, Germany (Dr. A. Ney)
- Universität Bielefeld, Germany (Dr. A. Thomas)
- University of British Columbia, Vancouver, Canada (Prof. D. Bonn, Prof. A. Damascelli)
- Max-Planck-Institut für Chemische Physik fester Stoffe, Dresden, Germany (Prof. F. Steglich)
- Technische Universität München, Physics Department, Germany (Prof. P. Böni, Prof. F. von Feilitzsch, Prof. D. Grundler, Prof. Ch. Pfleiderer, Prof. F.C. Simmel)
- Walter Schottky Institut, TU München, Germany (Prof. G. Abstreiter, Prof. M. Stutzmann, Prof. J. Finley, Dr. M. Brandt, Dr. D. Bougeard, Prof. A. Holleitner)
- Ludwig-Maximilians-Universität München, Physics Department, Germany (Prof. J.P. Kotthaus, Prof. J. von Delft, Prof. E. Frey, Prof. T. Franosch, Prof. J. Rädler, Dr. E. Weig, Dr. S. Ludwig)
- Ludwig-Maximilians-Universität München, Chemistry Department, Germany (Prof. Hubert Ebert, Dr. Diemo Ködderitzsch)
- University of Birmingham, UK (Prof. E.M. Forgan)
- Paul Scherrer Institute, ETH Zürich (Prof. Joel Mesot)
- University of Geneva, Switzerland (O. Fischer)
- HMI Berlin, Germany (Dr. A. Buchsteiner, Dr. J. Pieper, Dr. K. Siemensmeyer)
- Royal Holloway University, London UK (Prof. J. Saunders)
- University of Liverpool, UK (Dr. J. Goff)
- CNRS Grenoble, France (Prof. H. Godfrin)
- University of Florida, USA (Prof. D. Adams, Prof. Y. Takano)
- Universidad de Zaragoza, Spain (Prof. L. Morellon, Prof. J.M. de Teresa)
- EPFL Lausanne, Switzerland (Prof. H. Ronnov)
- University of New South Wales, Sydney, Australia (M. Simmons, A. Morello)
- McMaster University, Hamilton, Canada (Prof. J.P. Carbotte)
- Technische Universität Graz, Austria (Dr. E. Schachinger)
- Universität Konstanz (Prof. A. Leitenstorfer, Dr. R. Huber, Dr. J. Demsar, Dr. A. Pashkin)
- BMW Group, Munich, Germany (Dr. J. Schnagl)
- Siemens AG, CT MM 2, Munich, Germany (Dr. R. Matz)
- Attocube, Munich, Germany (Prof. K. Karrai, Dr. D. Andres)
- THEVA Dünnschichttechnik, Ismaning, Germany (Dr. W. Prusseit)

Stays abroad

Extended visits of members of the Walther-Meißner-Institute at foreign research laboratories:

1. **Toni Helm**
   High Magnetic Field Laboratory, Tallahassee, USA
   25. 01. - 06. 02. 2011
2. **Mark Kartsovnik**
   High Magnetic Field Laboratory, Tallahassee, USA
   29. 01. - 06. 02. 2011
3. **Toni Helm**
   High Magnetic Field Laboratory, Grenoble, France
   27. 02. - 07. 03. 2011
4. **Mark Kartsovnik, Toni Helm**
   High Magnetic Field Laboratory, Toulouse, France
   08 . 05. - 13. 05. 2011
5. **Toni Helm**
   High Magnetic Field Laboratory, Dresden
   10. 07. - 24. 07. 2011
6. **Mark Kartsovnik**
   Institute of Solid State Physics, Chernogolovka, Russia
   25. 07. - 05. 08. 2011, 17. 11. - 31. 12. 2011
7. **Rudi Hackl**
   Stanford University, Stanford, USA
   13. 03. - 05. 04. 2011
8. **Anton Lerf**
   Instituto de Ciencia de Materiales de Sevilla, Sevilla, Spain
   23. - 30. 03. 2011
9. **Matthias Opel**
   Material Science Research Centre, Indian Institute of Technology Madras, Chennai, India
   13. - 18. 11. 2011
10. **Matthias Opel**
    Cavendish Laboratory, University of Cambridge, England
    28. - 30. 11. 2011

Conference Talks and Seminar Lectures

Alexander Baust

1. **Superconducting coplanar waveguides for experiments with flux circuits**
   4^{th} Workshop on the Physics and Applications of Superconducting Microresonators, Grenoble, France.
   28. - 29. 07. 2011

Bea Botka

1. **Optical and Raman investigation of EU(III) complex nanotube hybrids**
   Biannual meeting of the EU Marie Curie project (FINELUMEN), Munich, Germany.
   14. 04. 2011
2. **Raman measurements on CNTs functionalized with luminescent lanthanide complexes**
   Biannual meeting of the EU Marie Curie project (FINELUMEN), Namur, Belgium.
   23. 09. 2011

Nitin Chelwani

1. **Infrared spectroscopic study of luminescent molecules**
   Biannual meeting of the EU Marie Curie project (FINELUMEN), Namur, Belgium.
   23. 09. 2011

Frank Deppe

1. **Experiments on superconducting flux quantum circuits**
   Colloquium of SFB/TR 21, Universität Ulm, Germany.
   18. 11. 2011

Hans-Martin Eiter

1. **Charge density wave order RTe_3**
   Miniworkshop on Complex Order and Fluctuations, Walther-Meißner-Institut, Garching, Germany.
   25. 07. 2011

Andreas Erb

1. **Intermetallische und oxydische Systeme mit Spin und Ladungskorrelationen**
   DGKK-Arbeitskreis Treffen, Dresden, Germany.
   06. - 07. 10. 2011
2. **Crystal growth of the high temperature superconductors**
   MaReMaS-Seminar, Universität Leipzig, Germany.
   07. 12. 2011

Sebastian Gönnenwein

1. **Scaling behavior of the spin pumping effect in ferromagnet/platinum bilayers**
   3. TUM Nanomagnetik-Workshop, TU München, Germany.
   28. 01. 2011
2. **Spin Pumping**
   Seminar der Abt. PGI-6, Peter Grünberg Institut, Forschungszentrum Jülich, Germany.
   10. 02. 2011

3. **Magnetotransport and Magnetization Control in Multifunctional Heterostructures**
   Seminar des Paul-Drude-Instituts Berlin, Germany.
   22. 02. 2011
4. **Spin Pumping**
   NIM Winter School 2011, St. Christoph, Austria.
   01. 04. 2011
5. **Anisotropic Magneto-Resistance and Anisotropic Magneto-Seebeck Effect in (Ga,Mn)As Thin Films**
   Spin Caloritronics III, Lorentz Center, Leiden, The Netherlands.
   10. 05. 2011
6. **Spin Mechanics**
   Seminar des SFB 689, Universität Regensburg, Germany.
   30. 05. 2011
7. **Voltage-Controlled Spin Mechanics**
   Seminar des Lehrstuhls für Experimentalphysik I, Universität Augsburg, Germany.
   20. 06. 2011
8. **Voltage-Controlled Spin Mechanics**
   CeNS Workshop 2011, Venice, Italy.
   20. 09. 2011
9. **Spin Mechanics and Spin Pumping in Ferromagnetic/Ferroelectric Hybrids**
   Workshop on Functional Hybrid Nanosystems, TUM, Institute of Advanced Study, Garching
   16. 11. 2011

Rudolf Gross

1. **Strain Control of Magnetism in Complex Oxide Heterostructures and Hybrids**
   471st WE-Heraeus Seminar on "Functional Magnetoelectric Oxide Heterosturctures"
   January 05 – 07, 2011, Bad Honnef, Germany.
2. **From Flux Quantization to Superconducting Quantum Bits**
   22nd Edgar Lüscher-Seminar
   February 12 – 18, 2011, Klosters, Switzerland.
3. **Circuit QED in the Ultra-strong Coupling Regime**
   NIM Winter School
   March 27 – April 02, 2011, St. Christoph, Austria.
4. **Circuit QED in the Ultra-strong Coupling Regime**
   International Conference on "Quantum Science and Technologies"
   May 09 – 12, 2011, Rovereto, Italy.
5. **Ultra-Strong Light-Matter Interaction in Circuit-QED Systems**
   18th Central European Workshop on "Quantum Optics"
   May 29 – June 03, 2011, Madrid, Spain.
6. **Strain Engineering and Control of Magnetic Materials**
   Public Colloquium of SFB 855 "Magnetoelectric Composites - Future Biomagnetic Interfaces"
   June 27 –28, 2011, Kiel, Germany.
7. **Modern Aspects of Solid State Physics**
   Ferienakademie der Technischen Universität München und der Universitäten Stuttgart und Erlangen-Nürnberg
   September 18 – 30, 2011, Sarntal, Italy.
8. **Superconducting Quantum Circuits**
   Humboldt Kolleg "Cooperation and Networking of Universities and Research Institutes, study by doing research – NANO-2011"
   October 06 – 09, 2011, Chisinau, Moldova.
9. **Light-Matter Interaction: from Strong to Ultrastrong Coupling in Superconducting Quantum Circuits**
   18. 10. 2011
   Physikalisches Kolloquium, Fachbereich Physik, Universität Stuttgart, Germany.

10. **ZnO Thin Films and Heterostructures for Spin Injection Devices**
Materials Research Society Fall Meeting
November 28 – December 02, 2011, Boston, USA.

Rudolf Hackl

1. **Hallmarks of spectroscopic studies of superconductors**
26^{th} Workshop on Novel Materials and Superconductors, Planneralm, Donnersbach, Austria.
15. 02. 2011
2. **Raman spectroscopy in far and near field**
FINELUMEN International Summer School 2011, Lochow, Poland.
26. 05. 2011
3. **Carrier anisotropies in superconductors with high transition temperature**
EMRS Fall Meeting 2011, Warschau, Poland.
20. 09. 2011
4. **New results on FeAs and RTe_3 compounds: Selection rules and charge gaps**
International Workshop on the SIMES group, SLAC, Stanford University, Stanford, USA.
31. 03. 2011
5. **Why are superconductors still interesting?**
Physics Colloquium at the TU Dresden, Dresden, Germany.
25. 10. 2011
6. **The fascinating properties of unconventional superconductors**
Colloquium at DESY, Hamburg, Germany.
15. 11. 2011
7. **Final state interactions and the pairing potential in superconductors**
Colloquium on the occasion of the 75^{th} birthday of A. Zawadowski, Budapest, Hungary.
25. 11. 2011

Hans Hübl

1. **Taking Ferromagnetic Resonance to Millikelvin Temperatures**
APS March Meeting, Dallas, USA.
18. - 26. 03. 2011
2. **Donor Spins in Silicon: Spin Control and Single Spin Readout**
VCIAN, Las Vegas, USA.
20. - 27. 04. 2011
3. **Strong coupling of photons and magnons in systems with exchange interaction**
Collective Spins, Oxford, England.
17. - 19. 05. 2011

Mark Kartsovnik

1. **Probing the Fermi surface of the electron-doped cuprate superconductor $Nd_{2-x}Ce_xCuO_4$ by high-field magnetotransport**
Aspen Winter Conference, Aspen, Colorado, USA.
22. - 28. 01. 2011
2. **High-field magnetotransport and the Fermi surface of the n-doped cuprate superconductor $Nd_{2-x}Ce_xCuO_4$**
EuroMagNET II user meeting, Toulouse, France.
23. 06. 2011
3. **Magnetic Quantum Oscillations and the Fermi Surface in $Nd_{2-x}Ce_xCuO_4$**
International conference on "Quantum Phenomena in Complex Matter 2011 - STRIPES 11", Rome, Italy.
10. - 16. 07. 2011

4. **Magnetic field effects on the charge-density-wave and superconducting states in α-(BEDT-TTF)$_2$KHg(SCN)$_4$**
   International Research School-Workshop on Electric Crystals, ECRYS-2011, Cargese, France.
   15. - 27. 08. 2011
5. **High magnetic field studies of the Fermi surface in high-T$_c$ cuprate superconductors**
   ISSP Seminar, Chernogolovka, Russia.
   17. 11. - 30. 12. 2011

Florian Kretzschmar

1. **Raman study of the gap in $Ba_{0.6}K_{0.4}Fe_2As_2$**
   Miniworkshop on Complex Order and Fluctuations, Walther-Meißner-Institut, Garching, Germany.
   25. 07. 2011

Anton Lerf

1. **Intercalation and Dynamics of Hydrated Fe^{2+} in the Vermiculites from Santa Olalla and Ojén**
   International Symposium Compounds ISIC16, Sec, Czech Republic.
   22. - 26. 05. 2011

Bernhard Muschler

1. **Raman study of magnetically ordered $BaFe_2As_2$**
   Miniworkshop on Complex Order and Fluctuations, Walther-Meißner-Institut, Garching, Germany.
   25. 07. 2011

Matthias Opel

1. **Oxide thin film structures for spintronic applications**
   Material Science Research Centre, IIT Madras, Chennai, India.
   16. 11. 2011
2. **Dilute magnetic doping and spin injection in the wide bandgap semiconductor ZnO**
   Cavendish Laboratory, University of Cambridge, England.
   29. 11. 2011
3. **Electrical spin injection into the wide bandgap semiconductor ZnO**
   MAM-SYNT Workshop on Synthesis and Design of Multi-Functional Materials and Heterostructures, Ercolano, Italy.
   24. 10. 2011
4. **Multifunctional materials based on oxide thin films and heterostructures**
   DAE-BRNS 6^{th} National Symposium on Pulsed Laser Deposition of Thin Films and Nanostructured Materials, Materials Research Centre, Indian Institute of Science, Bengaluru, India.
   09. 11. 2011

Kurt Uhlig

1. **Cryogen-free Dilution Refrigerators**
   26^{th} International Conference on Low Temperature Physics, Beijing, China.
   10.- 17. 08. 2011

Lectures, Seminars, Courses and other Scientific Activities

Several members of Walther-Meißner-Institut give lectures and seminars at the Technische Universität München.

Lectures

Dietrich Einzel

WS 2010/2011	• Mathematische Methoden der Physik I (Mathematical Methods of Physics I) • Übungen zu Mathematische Methoden der Physik I (Mathematical Methods of Physics I, Problem Sessions) • WMI-Seminar über aktuelle Fragen der Tieftemperatur-Festkörperphysik (WMI Seminar on Current Topics of Low Temperature Solid State Physics, with R. Gross, S.B.T. Gönnenwein, A. Marx, M. Opel, R. Hackl) • Seminar on Advances in Solid-State Physics (with R. Gross, M. Opel, A. Marx, S.T.B. Gönnenwein)
SS 2011	• Mathematische Methoden der Physik II (Mathematical Methods of Physics II) • Übungen zu Mathematische Methoden der Physik II (Mathematical Methods of Physics II, Problem Sessions) • WMI-Seminar über aktuelle Fragen der Tieftemperatur-Festkörperphysik (WMI Seminar on Current Topics of Low Temperature Solid-State Physics, with R. Gross, S.B.T. Gönnenwein, A. Marx, M. Opel, R. Hackl) • Seminar on Advances in Solid-State Physics (with R. Gross, M. Opel, A. Marx, S.T.B. Gönnenwein)
WS 2011/2012	• Mathematische Methoden der Physik I (Mathematical Methods of Physics I) • Übungen zu Mathematische Methoden der Physik I (Mathematical Methods of Physics I, Problem Sessions) • WMI-Seminar über aktuelle Fragen der Tieftemperatur-Festkörperphysik (WMI Seminar on Current Topics of Low Temperature Solid-State Physics, with R. Gross, S.B.T. Gönnenwein, H. Hübl, A. Marx, M. Opel, R. Hackl) • Seminar on Advances in Solid-State Physics (with R. Gross, M. Opel, A. Marx, S.T.B. Gönnenwein)

Frank Deppe

WS 2010/2011	• Angewandte Supraleitung: Josephson-Effekte und Supraleitungselektronik (Applied Superconductivity: Josephson-Effects and Superconducting Electronics) • Übung zu Angewandte Supraleitung: Josephson-Effekte und Supraleitungselektronik (Exercises to Applied Superconductivity: Josephson-Effects and Superconducting Electronics)

- Seminar: Supraleitende Quantenschaltkreise (mit R. Gross, A. Marx) (Seminar on Superconducting Quantum Circuits)

SS 2011
- Supraleitung und Tieftemperaturphysik 2 (Superconductivity and Low Temperature 2)
- Übungen zu Supraleitung und Tieftemperaturphysik 2 (Exercises to Superconductivity and Low Temperature 2)
- Seminar: Supraleitende Quantenschaltkreise (mit R. Gross, A. Marx) (Seminar on Superconducting Quantum Circuits)

WS 2011/2012
- Angewandte Supraleitung: Josephson-Effekte und Supraleitungselektronik (Applied Superconductivity: Josephson-Effects and Superconducting Electronics)
- Übung zu Angewandte Supraleitung: Josephson-Effekte und Supraleitungselektronik (Exercises to Applied Superconductivity: Josephson-Effects and Superconducting Electronics)
- Seminar: Supraleitende Quantenschaltkreise (mit R. Gross, A. Marx) (Seminar on Superconducting Quantum Circuits)

Rudolf Gross

WS 2010/11
- Physik der kondensierten Materie I (Condensed Matter Physics I)
- Tutorium zur Physik der kondensierten Materie I (Condensed Matter Physics I, Tutorium)
- Übungen zur Physik der kondensierten Materie I (Condensed Matter Physics I, Problem Sessions, with R. Hackl, D. Einzel)
- WMI-Seminar über aktuelle Fragen der Tieftemperatur-Festkörperphysik (WMI Seminar on Current Topics of Low Temperature Solid-State Physics, with D. Einzel, S.T.B. Gönnenwein, R. Hackl, H. Hübl, A. Marx, M. Opel)
- Seminar on Advances in Solid-State Physics (with D. Einzel, S.T.B. Gönnenwein, R. Hackl, H. Hübl, A. Marx, M. Opel)
- Seminar on Superconducting Quantum Circuits (with F. Deppe, A. Marx)
- Festkörperkolloquium (Colloquium on Solid-State Physics, with D. Einzel)

SS 2011
- Physik der kondensierten Materie I (Condensed Matter Physics I)
- Tutorium zur Physik der kondensierten Materie I (Condensed Matter Physics I, Tutorium)
- Übungen zur Physik der kondensierten Materie I (Condensed Matter Physics I, Problem Sessions, with R. Hackl, D. Einzel)
- Seminar on Advances in Solid-State Physics (with D. Einzel, S.T.B. Gönnenwein, R. Hackl, H. Hübl, A. Marx, M. Opel)
- WMI-Seminar über aktuelle Fragen der Tieftemperatur-Festkörperphysik (WMI Seminar on Current Topics of Low Temperature Solid-State Physics, with D. Einzel, S.T.B. Gönnenwein, R. Hackl, H. Hübl, A. Marx, M. Opel)

- Seminar on Superconducting Quantum Circuits (with F. Deppe, A. Marx)
- Festkörperkolloquium (Colloquium on Solid-State Physics, with D. Einzel)
- Ferienakademie: Kurs 3 "Physik und Elektronik im Alltag" (Ferienakademie: Course 3 "Physics and Electronics in Everyday Life")

WS 2011/12
- Supraleitung und Tieftemperaturphysik I (Superconductivity and Low Temperature Physics I)
- Übungen zu Supraleitung und Tieftemperaturphysik I (Superconductivity and Low Temperature Physics I, Problem Sessions)
- WMI-Seminar über aktuelle Fragen der Tieftemperatur-Festkörperphysik (WMI Seminar on Current Topics of Low Temperature Solid-State Physics, with D. Einzel, S.T.B. Gönnenwein, R. Hackl, H. Hübl, A. Marx, M. Opel)
- Seminar on Advances in Solid-State Physics (with D. Einzel, S.T.B. Gönnenwein, R. Hackl, H. Hübl, A. Marx, M. Opel)
- Seminar on Superconducting Quantum Circuits (with F. Deppe, A. Marx)
- Festkörperkolloquium (Colloquium on Solid-State Physics, with D. Einzel)

Sebastian T.B. Gönnenwein

WS 2010/2011
- Seminar on Advances in Solid-State Physics (with R. Gross, A. Marx, M. Opel, D. Einzel, R. Hackl, H. Hübl)
- Seminar: Spin Caloritronics and Spin Pumping
- WMI-Seminar über aktuelle Fragen der Tieftemperatur-Festkörperphysik (WMI Seminar on Current Topics of Low Temperature Solid State Physics, with R. Gross, D. Einzel, H. Hübl, A. Marx, M. Opel, R. Hackl)
- Seminar zu aktuellen Fragen der Magneto- und Spinelektronik (Seminar on Current Topics in Magneto and Spin Electronics, with M. Brandt, M. Opel)

SS 2011
- Seminar: Spinmechanik und Spindynamik (Seminar on Spin Mechanics and Spin Dynamics)
- Seminar on Advances in Solid-State Physics (with R. Gross, A. Marx, M. Opel, D. Einzel, R. Hackl, H. Hübl)
- WMI-Seminar über aktuelle Fragen der Tieftemperatur-Festkörperphysik (WMI Seminar on Current Topics of Low Temperature Solid-State Physics, with R. Gross, D. Einzel, A. Marx, M. Opel, R. Hackl)
- Seminar zu aktuellen Fragen der Magneto- und Spinelektronik (Seminar on Current Topics in Magneto and Spin Electronics, with M. Brandt, M. Opel)

WS 2011/2012
- Seminar on Advances in Solid-State Physics (with R. Gross, A. Marx, M. Opel)

- Seminar: Spin Caloritronics and Spin Pumping
- WMI-Seminar über aktuelle Fragen der Tieftemperatur-Festkörperphysik (WMI Seminar on Current Topics of Low Temperature Solid State Physics, with R. Gross, D. Einzel, H. Hübl, A. Marx, M. Opel, R. Hackl)
- Seminar zu aktuellen Fragen der Magneto- und Spinelektronik (Seminar on Current Topics in Magneto and Spin Electronics, with M. Brandt, H. Hübl)

Rudi Hackl

WS 2010/2011
- Supraleitung und Tieftemperaturphysik I (Superconductivity and Low Temperature Physics I, with R. Gross)
- Problems and Solutions in Superconductivity (with D. Einzel)
- Problems and Solutions in Solid State Physics (with R. Gross, D. Einzel)
- WMI-Seminar über aktuelle Fragen der Tieftemperatur-Festkörperphysik (WMI Seminar on Current Topics of Low Temperature Solid-State Physics, with R. Gross, S.B.T. Gönnenwein, H. Hübl, A. Marx, M. Opel, D. Einzel)
- Seminar on Advances in Solid-State Physics (with R. Gross, S.T.B. Gönnenwein, H. Hübl, A. Marx, M. Opel)

SS 2011
- Problems and Solutions in Solid State Physics (with R. Gross, D. Einzel)
- WMI-Seminar über aktuelle Fragen der Tieftemperatur-Festkörperphysik (WMI Seminar on Current Topics of Low Temperature Solid-State Physics, with R. Gross, S.B.T. Gönnenwein, H. Hübl A. Marx, M. Opel, D. Einzel)
- Seminar on Advances in Solid-State Physics (with R. Gross, S.T.B. Gönnenwein, H. Hübl, A. Marx, M. Opel)

WS 2011/2012
- Seminar on Advances in Solid-State Physics (with R. Gross, S.T.B. Gönnenwein, H. Hübl, A. Marx, M. Opel)
- WMI-Seminar über aktuelle Fragen der Tieftemperatur-Festkörperphysik (WMI Seminar on Current Topics of Low Temperature Solid-State Physics, with R. Gross, S.B.T. Gönnenwein, H. Hübl, A. Marx, M. Opel, D. Einzel)

Hans Hübl

WS 2010/2011
- Magnetismus mit Übungen (Magnetism)
- Seminar on Advances in Solid-State Physics (with R. Gross, D. Einzel, S.T.B. Gönnenwein, A. Marx, M. Opel)
- WMI-Seminar über aktuelle Fragen der Tieftemperatur-Festkörperphysik (WMI Seminar on Current Topics of Low Temperature Solid State Physics, with R. Gross, D. Einzel, S.T.B. Gönnenwein, A. Marx, M. Opel, R. Hackl)

SS 2011
- Spinelektronik mit Übungen
- Seminar on Advances in Solid-State Physics (with R. Gross, A. Marx, M. Opel, S.T.B. Gönnenwein, D. Einzel)

	• WMI-Seminar über aktuelle Fragen der Tieftemperatur-Festkörperphysik (WMI Seminar on Current Topics of Low Temperature Solid-State Physics, with R. Gross, D. Einzel, A. Marx, M. Opel, R. Hackl)
WS 2011/2012	• Magnetismus mit Übungen (Magnetism)
	• Seminar on Advances in Solid-State Physics (with R. Gross, D. Einzel, S.T.B. Gönnenwein, A. Marx, M. Opel)
	• WMI-Seminar über aktuelle Fragen der Tieftemperatur-Festkörperphysik (WMI Seminar on Current Topics of Low Temperature Solid State Physics, with R. Gross, D. Einzel, S.T.B. Gönnenwein, A. Marx, M. Opel, R. Hackl)
	• Seminar zu aktuellen Fragen der Magneto- und Spinelektronik (Seminar on Current Topics in Magneto and Spin Electronics, with S.T.B. Gönnenwein, M. S. Brandt)

Anton Lerf

WS 2010/2011	• Moderne Aspekte der Chemie für Physiker I (Modern Aspects of Chemistry for Physicists I)
SS 2011	• Moderne Aspekte der Chemie für Physiker II (Modern Aspects of Chemistry for Physicists II)
	• Nanostrukturierte Materie (Nanostructured Matter, with Prof. J. Plank)
WS 2011/2012	• Moderne Aspekte der Chemie für Physiker I (Modern Aspects of Chemistry for Physicists I)

The WMI Seminars

The Friday Seminar – Walther-Meißner-Seminar on Current Topics in Low Temperature Physics

1. **Erfindungswesen und Patentwesen an der TUM**
   Dipl.-Phys. Anita Widmann, Patent- und Lizenzbüro der TU München
   14. 01. 2011
2. **Functional perovskite superlattices and nanostructures fabricated by pulsed-laser deposition**
   Dr. Ionela Vrejoiu, Max-Planck-Institut für Mikrostrukturphysik, Halle
   28. 01. 2011
3. **Parametric resonators for quantum information applications**
   Dr. Christopher Wilson, Chalmers University, Schweden
   11. 02. 2011
4. **Superconductivity: deep superficial insights**
   Prof. Andrea Damascelli, University of British Columbia, Canada
   04. 03. 2011

5. **Low voltage electron emission from ferroelectric materials**
   Dr. Oliver Mieth, Technische Universität Dresden
   21. 04. 2011
6. **Topological superconductors**
   Prof. Yoichi Ando, Osaka University Ibaraki, Osaka, Japan
   06. 05. 2011
7. **Tuning superconductivity by carrier injection**
   Prof. Paul Müller, Universität Erlangen-Nürnberg
   13. 05. 2011
8. **High frequency electro-mechanical control of optically active nanostructures using surface acoustic waves**
   Dr. Hubert J. Krenner, Universität Augsburg
   20. 05. 2011
9. **Einführung in die Phänomenologie der heterotischen Stringtheorie**
   Matthias Danner, Walther-Meissner-Institut, Garching
   10 .06. 2011
10. **Some new reflections on spin-wave dynamics**
    Dr. Alexy Karenowska, Oxford University, UK
    08. 07. 2011
11. **Numerical Exact Diagonalization studies of inelastic light scattering**
    Chunjing Jia, Stanford University, Stanford, USA
    21. 07. 2011
12. **Als Ingenieur/Physiker bei Bosch Automotive**
    Dr. Daniel Reisinger, Robert Bosch GmbH, Reutlingen
    22. 07. 2011
13. **Entwicklung von Si-basierten Strahlungsdetektoren für Forschungsvorhaben**
    Dr. Petra Majewski, PN Sensor GmbH, München
    22. 07. 2011
14. **Superconducting coplanar wave guide resonators for measurements of molecular spins**
    Ling Zhong, Chalmers University, Schweden
    29. 07. 2011

15. **A common thread: the pairing interaction in the heavy fermion, cuprate and Fe supercondcutors**
    Prof. Douglas Scalapino, University of California, Santa Barbara, USA
    07. 10. 2011

16. **Interlayer magnetoresistance in strongly anisotropic quasi-2D compounds**
Dr. Pavel Grigoriev, L.D. Landau Institute for Theoretical Physics, Chernogolovka, Russia
17. 10. 2011
17. **Quantum Dots of ZnO: How do they grow and how do they glow?**
Prof. Lalit M. Kukreja, Raja Ramanna Centre for Advanced Technology, Indore, India
21. 10. 2011
18. **Fabrication of Nb thin films with modulated thickness for the investigation of the static and dynamic properties of Abrikosov vortices in artificial potential landscapes**
Benedikt Betz, Physikalisches Institut, Universität Tübingen
09. 12. 2011

Topical Seminar on Advances in Solid State Physics – WS 2010/2011, SS 2011 and WS 2011/2012

1. **Preliminary discussion and assignment of topics**
Rudolf Gross, Walther-Meißner-Institut
19. 10. 2010
2. **Study of correlated electron systems with applied pressure**
Reinhard Rossner, Walther-Meißner-Institut
02. 11. 2010
3. **Vibrational studies of confined luminescent systems**
Nitin Chelwani, Hungarian Academy of Sciences, Budapest, Ungarn
16. 11. 2010
4. **Graphene**
Michael Schreier, Technische Universität München
23. 11. 2010
5. **Silicon Detectors and Integrated Readout Electronics for X-ray Imaging, Spectroscopy, and Synchrotron Applications**
Davide Bianchi, Max-Planck-Institut für Extraterrestische Physik, Garching
30. 11. 2010
6. **Growth and Characterization of Ferromagnetic Heusler Compound Thin Films**
Alexander Krupp, Walther-Meißner-Institut
07. 12. 2010
7. **Thermodynamics of Phase Diagrams**
Andrea Winnerl, Technische Universität München
14. 12. 2010
8. **Magnetic Digital Logic and Memory Circuits**
Alexander Büse, Technische Universität München
21. 12. 2010
9. **Josephson Light-Emitting Diode**
Alexander Kupijai, Technische Universität München
25. 01. 2011

10. **Preliminary discussion and assignment of topics**
Rudolf Gross, Walther-Meissner-Institut
03. 05. 2011
11. **The Superconducting Quantum Interference Proximity Effect Transistor**
Thomas Losinger, Technische Universität München
24. 05. 2011
12. **Herstellung und Charakterisierung von linearen supraleitenden Schaltkreisen I**
Norbert Kalb, Technische Universität München
21. 06. 2011
13. **Herstellung und Charakterisierung von linearen supraleitenden Schaltkreisen II**
Lukas Augsbach, Technische Universität München
21. 06. 2011

14. **Automatized setup for measuring temperature-dependent resistivity of cuprate and organic superconductors**
    Tobias Lamm, Technische Universität München
    28. 06. 2011
15. **Anschluss eines Multiplex-Multimeters zur Überwachung eines Kryostaten**
    Markus Künzl, Technische Universität München
    28. 06. 2011
16. **Skalierbarer Probenhalter für Experimente mit supraleitenden Schaltkreisen**
    Uwe Peter Ehmann, Technische Universität München
    05. 07. 2011
17. **High-field magnetization of κ-(BETS)$_2$Mn[N(CN)$_2$]$_3$**
    Fabian Jerzembeck, Technische Universität München
    12. 07. 2011
18. **Aufzeichnen eines Energiewertstromes in einem Prozessabschnitt der Zylinderkopffertigung im Motorenbau**
    Jacob Ducke, Technische Universität München
    12. 07. 2011
19. **Aufbau eines Probenstabes für die Diamantdruckzelle**
    Valentin Kunkel, Technische Universität München
    19. 07. 2011
20. **Tempern und Charakterisierung von oxidischen Proben**
    Marlies Gangl, Technische Universität München
    19. 07. 2011
21. **Realisierung von Impedanz-angepassten Pulverfiltern für Experimente mit Fluss-Quantenbits**
    Thomas Ramirez, Technische Universität München
    26. 07. 2011
22. **Auflösungsgrenze des Dual-Path-Detektors für propagierende Quantenmikrowellen**
    Philipp Summer, Technische Universität München
    26. 07. 2011

23. **Preliminary discussion and assignment of topics**
    R. Gross, Walther-Meißner-Institut
    18. 10. 2011
24. **Ferromagnetic resonance at low temperatures**
    Christoph Zollitsch
    13. 12. 2011
25. **Gradiometric flux quantum bits with tunable tunnel coupling**
    Jan Götz, Walther-Meißner-Institut
    20. 12. 2011
26. **Nb/AlO$_x$/Nb Josephson junctions for superconducting quantum circuits**
    Friedrich Wulschner, Walther-Meißner-Institut
    17. 01. 2012
27. **Interlayer Magnetoresistance of the Quasi-twodimensional Charge Density Wave Superconductor α-(BEDT-TTF)$_2$KHg(SCN)$_4$ at Low Temperatures**
    Michael Kunz, Walther-Meißner-Institut
    31. 01. 2012
28. **Magnetoresistive and magnetogalvanic effects in (Ga,Mn)As**
    Sibylle Meyer, Walther-Meißner-Institut
    07. 02. 2012

Topical Seminar: Spin Mechanics and Spin Dynamics – SS 2011

1. **Preliminary discussion and assignment of topics**
   Sebastian Gönnenwein, Walther-Meißner-Institut

04. 05. 2011

2. **Epitaktisches Wachstum dünner ferromagnetischer Schichten aus Y3Fe5O12 via "Pulsed Laser Deposition"**
   Martin Wagner, Walther-Meißner-Institut
   23. 05. 2011
3. **Epitaxie und Magnetotransport in ZnO/Ferromagnet Heterostrukturen**
   Eva Karrer-Müller, Walther-Meißner-Institut
   30. 05. 2011
4. **Spin Pumping**
   Philipp Braun, Technische Universität München
   06. 06. 2011
5. **Akustische ferromagnetische Resonanz**
   Alexander Kleinkauf, Walther-Meißner-Institut
   20. 06. 2011
6. **Interferrometrische Messungen von Oberflächenauslenkungen**
   Rasmus Holländer, Walther-Meißner-Institut
   27. 06. 2011
7. **Herstellung und Charakterisierung von SAW-Strukturen**
   Frederik Georg, Walther-Meißner-Institut
   04. 07. 2011
8. **Spin Kaloritronik**
   Georg Benka, Walther-Meißner-Institut
   11. 07. 2011
9. **Spin-Seebeck-Effekt**
   Michael Schreier, Technische Universität München
   18. 07. 2011
10. **Magneto-Seebeck-Effekt**
    Sibylle Meyer, Walther-Meißner-Institut
    25. 07. 2011

Topical Seminar on Superconducting Quantum Circuits – WS 2010/2011, SS 2011 and WS 2011/2012

1. **Preliminary discussion and assignment of topics**
   Frank Deppe, Achim Marx, Rudolf Gross, Walther-Meißner-Institut
   19. 10. 2010
2. **Microwave-Induced Cooling of a Superconducting Qubit**
   Thomas Losinger, Technische Universität München
   23. 11. 2010
3. **Frozen Light**
   Benno Blaschke, Technische Universität München
   14. 12. 2010
4. **Ultra-strong Light-Matter Interaction**
   Franz Sterr, Technische Universität München
   11. 01. 2011
5. **Strong Coupling between Spins and Cavities**
   Nikolaj Bittner, Technische Universität München
   25. 01. 2011

6. **Preliminary discussion and assignment of topics**
   Frank Deppe, Achim Marx, Rudolf Gross, Walther-Meißner-Institut
   03. 05. 2011
7. **Circuit cavity electromechanics in the strong-coupling regime**
   Fredrik Hocke, Walther-Meißner-Institut
   10. 05. 2011

8. **Deterministic Entanglement of Photons in Two Superconducting Microwave Resonators**
   Elisabeth Hoffmann, Walther-Meißner-Institut
   24. 05. 2011
9. **Herstellung von Nb/AlOx/Nb Kontakten für supraleitende Mikrowellenbauelemente**
   Karl Friedrich Wulschner, Walther-Meißner-Institut
   31. 05. 2011
10. **Observation of Quantum Jumps in a Superconducting Artificial Atom**
    Manuel Schwarz, Walther-Meißner-Institut
    07. 06. 2011
11. **Experimental Tomographic State Reconstruction of Itinerant Microwave Photons**
    Matthias Danner, Walther-Meißner-Institut
    21. 06. 2011
12. **Dual-path state reconstruction of propagating microwave**
    Peter Eder, Walther-Meißner-Institut
    28. 06. 2011
13. **The Single-Photon Router**
    Alexander Baust, Walther-Meißner-Institut
    05. 07. 2011
14. **Systematische Charakterisierung zweier Resonatortypen**
    Marta Krawczyk, Walther-Meißner-Institut
    12. 07. 2011
15. **Gradiometric flux quantum bits with tunable tunnel coupling**
    Jan Goetz, Walther-Meißner-Institut
    19. 07. 2011
16. **Herstellung und Charakterisierung von Flussquantenbits mit vier Josephson-Kontakten**
    Felix Bilger, Walther-Meißner-Institut
    26. 07. 2011

17. **Preliminary discussion and assignment of topics**
    F. Deppe, A. Marx, R. Gross, Walther-Meißner-Institut
    18. 10. 2011
18. **Superconducting qubit as a quantum transformer routing entanglement between a microscopic quantum memory and a macroscopic resonator**
    Elisabeth Hoffmann, Walther-Meißner-Institut
    15. 11. 2011
19. **Quantum walks of correlated particles**
    Jan Goetz, Walther-Meißner-Institut
    22. 11. 2011
20. **Noise spectroscopy through dynamical decoupling with a superconducting flux qubit**
    Ling Zhong, Walther-Meißner-Institut
    06. 12. 2011
21. **Quantum State Tomography of an Itinerant Squeezed Microwave Field**
    Alexander Baust, Walther-Meißner-Institut
    20. 12. 2011
22. **Full-field implementation of a perfect eavesdropper on a quantum cryptograph system**
    Max Häberlein, Walther-Meißner-Institut
    10. 01. 2012

C: Solid State Colloquium

The WMI has organized the Solid-State Colloquium of the Faculty of Physics in WS 2010/2011, SS 2011, and WS 2011/2012. The detailed program can be found on the WMI webpage: http://www.wmi.badw-muenchen.de/teaching/Seminars/fkkoll.html.

Staff of the Walther-Meißner-Institute

Director
Prof. Dr. Rudolf Gross

Deputy Director
Dr. Werner Biberacher

Technical Director
Dr. Achim Marx

Administration/Secretary's Office
Ludwig Ossiander
Emel Dönertas

Scientific Staff
Dr. Werner Biberacher
Dr. Frank Deppe
Priv.-Doz. Dr. habil. Dietrich Einzel
Dr. habil. Andreas Erb
Dr. habil. Sebastian Gönnenwein
Priv.-Doz. Dr. habil. Rudolf Hackl
Dr. Hans Hübl
Dr. Mark Kartsovnik
Prof. Dr. Anton Lerf
Dr. Achim Marx
Dr. Matthias Opel
Dr. Kurt Uhlig
Dipl.-Phys. Matthias Althammer
Dipl.-Phys. Alexander Baust
Dipl.-Phys. Bea Botka
Dipl.-Phys. Andreas Brandlmaier
Dipl.-Phys. Johannes Büttner
Dipl.-Phys. Nitin Chelwani
Dipl.-Phys. Franz Czeschka
Dipl.-Phys. Hans-Martin Eiter
Dipl.-Phys. Stephan Geprägs
Dipl.-Phys. Max Häberlein
Dipl.-Phys. Toni Helm
Dipl.-Phys. Fredrik Hocke
Dipl.-Phys. Elisabeth Hoffmann
Dipl.-Phys. Florian Kretzschmar
Dipl.-Phys. Johannes Lotze
Dipl.-Phys. Edwin Menzel
Dipl.-Phys. Bernhard Muschler
Dipl.-Phys. Thomas Niemczyk
Dipl.-Phys. Manuel Schwarz
Dipl.-Phys. Mathias Weiler
Dipl.-Phys. Ling Zhong

Technical Staff
Peter Binkert
Dipl.-Ing. (FH) Thomas Brenninger
Dipl.-Ing. (FH) Ulrich Guggenberger
Dieter Guratzsch
Astrid Habel
Karen Helm-Knapp
Dipl.-Ing. (FH) Josef Höss
Namvar Jahanmehr
Julius Klaus
Robert Müller
Jan Naundorf
Georg Nitschke
Christian Reichlmeier
Harald Schwaiger
Helmut Thies
Siegfried Wanninger

Assistants

Sybilla Plöderl
Brigitte Steinberg

Permanent Guests

Prof. Dr. B. S. Chandrasekhar
Dr. Robert Doll
Dr. Christian Probst
Dr. Karl Neumaier
Prof. Dr. Erwin Schuberth

Guest Researchers

1. Prof. Dr. B.S. Chandrasekhar
   permanent guest
2. Dr. Robert Doll
   permanent guest
3. Dr. Karl Neumaier
   permanent guest
4. Dr. Christian Probst
   permanent guest
5. Prof. Dr. Erwin Schuberth
   permanent guest
6. Jorge Casanova, Universidad del Pais Vasco, Bilbao, Spain
   09. 04. - 01. 05. 2011
7. Dr. Guillermo Romero, Universidad del Pais Vasco, Bilbao, Spain
   09. 04. - 26. 04. 2011
8. Dr. Daniel Ballester, Universidad del Pais Vasco, Bilbao, Spain
   09. 04. - 24. 04. 2011
9. Nitin Chelwani, Hungarian Academy of Science, Budapest, Hungary
   15. 04. - 13. 05. 2011
10. Dr. Brian Moritz, Stanford University, Stanford, USA
    30. 06. - 27. 07. 2011
11. Prof. Dr. Juan Poyato Ferrera, Instituto de Ciencia de Materiales, Sevilla, Spain
    05. 07. - 28. 07. 2011
12. Prof. T.P. Devereaux, Stanford University, Stanford, USA
    01. 07. - 31. 07. 2011
13. Dr. M. Füchsle, Centre for Quantum Computing and Communication Technology University of New South Wales, Australia
    11. 07. - 15. 07. 2011
14. Dr. Lex Kemper and Y. Kung BSc, Stanford University, Stanford, USA
    12. 07. - 27. 07. 2011
15. C.-J. Jia BSc, Stanford University, Stanford, USA
    17. 07. - 28. 07. 2011
16. Dr. Lucia Steinke, Max-Planck-Institut für Chemische Physik fester Stoffe, Dresden, Germany
    01. 08. - 30. 09. 2011
17. PD Dr. P. Weinberger, Vienna University of Technology, Vienna, Austria
    27. 09. - 29. 09. 2011
18. Prof. Dr. J. Scalapino, University of California, Santa Barbara, USA
    06. 10. - 09. 10. 2011
19. Dr. Oleg Vyaselev, Institute of Solid Physics, Chernogolovka, Russia
    01. 10. - 15. 11. 2011
20. Dr. Daniel Ballester and Roberto Di Candia, Universidad del Pais Vasco, Bilbao, Spain
    04. 10. - 14. 10. 2011
21. Dr. Nataliya D. Kushch, Institute of Problems of Chemical Physics, Chernogolovka, Russia
    17. 10. - 01. 12. 2011

22. Dr. Pavel Kushch, Institute of Problems of Chemical Physics, Chernogolovka, Russia
    17. 10. - 16. 11. 2011
23. Dr. Pavel Grigoriev, Landau Institute, Chernogolovka, Russia
    17. 10. - 20. 10. 2011
24. Prof. Dr. Alfred Zawadowski, Budapest University of Technology and Economics, Budapest, Hungary
    07. 12. - 15. 12. 2011

Commission for Low Temperature Physics

Members of the Commission for Low Temperature Research of the Bavarian Academy of Sciences and Humanities:

Kaiser, Wolfgang, chairman (Technische Universität München)
Abstreiter, Gerhard, deputy chairman (Technische Universität München)
Gross, Rudolf (Walther-Meißner-Institut)
Landwehr, Gottfried (Universität Würzburg)
Hänsch, Theodor (Max-Planck-Institut für Quantenoptik, Garching)
Kotthaus, Jörg Peter (Ludwig-Maximilians-Universität München)
Schwoerer, Markus (Universität Bayreuth)
Vollhardt, Dieter (Universität Augsburg)
Weiss, Dieter (Universität Regensburg)